



**DGK** Veröffentlichungen der DGK

Ausschuss Geodäsie der Bayerischen Akademie der Wissenschaften

---

Reihe C

Dissertationen

Heft Nr. 933

**Hannes Sardemann**

**Conception and Realisation of a Photogrammetric  
Multisensor System for an Uncrewed Water Vehicle**

**München 2024**

**Bayerische Akademie der Wissenschaften**

ISSN 0065-5325

ISBN 978-3-7696-5345-8

---

Diese Arbeit ist gleichzeitig veröffentlicht in:

Qucosa – Dokumenten- und Publikationsserver der Sächsischen Landesbibliothek – Staats- und Universitätsbibliothek (SLUB)  
<https://nbn-resolving.org/urn:nbn:de:bsz:14-qucosa2-898707>, Dresden 2024



Conception and Realisation of a Photogrammetric Multisensor System  
for an Uncrewed Water Vehicle

Von der Fakultät Umweltwissenschaften  
der Technischen Universität Dresden  
zur Erlangung des akademischen Grades  
Doktor-Ingenieur (Dr.-Ing.)  
genehmigte Dissertation

von

Hannes Sardemann, M. Sc.

München 2024

Bayerische Akademie der Wissenschaften

Adresse der DGK:



Ausschuss Geodäsie der Bayerischen Akademie der Wissenschaften (DGK)

Alfons-Goppel-Straße 11 • D – 80 539 München  
Telefon +49 - 331 - 6264 1685 • E-Mail [post@dgk.badw.de](mailto:post@dgk.badw.de)  
<http://www.dgk.badw.de>

Prüfungskommission:

Vorsitzende: Jun.-Prof. Dr.-Ing. Anette Eltner

Referent: Prof. Dr. sc. techn. habil. Hans-Gerd Maas

Korreferenten: Prof. Dr.-Ing. Dorota Iwaszczuk (TU Darmstadt)  
Prof. Dr.-Ing. habil. Dr. h.c. Thomas Luhmann (Jade Hochschule)

Tag der mündlichen Prüfung: 28.11.2023

---

© 2024 Bayerische Akademie der Wissenschaften, München

Alle Rechte vorbehalten. Ohne Genehmigung der Herausgeber ist es auch nicht gestattet,  
die Veröffentlichung oder Teile daraus auf photomechanischem Wege (Photokopie, Mikrokopie) zu vervielfältigen

ISSN 0065-5325

ISBN 978-3-7696-5345-8

## Declaration of Conformity

The conformity of this copy with the original dissertation on the subject:

"Conception and realisation of a photogrammetric multisensor system for an uncrewed water vehicle"  
is hereby confirmed.

## Statement of the Authorship

I, Hannes Sardemann, hereby certify that I have authored this dissertation entitled "Conception and realisation of a photogrammetric multisensor system for an uncrewed water vehicle" without additional resources and references than explicitly declared as such in the text by citation or footnote. I have marked both literal and accordingly adopted quotations as such. Unless otherwise stated, all graphics and illustrations were created by myself. The individual author contributions to the selected publications used in this cumulative dissertation are declared on an extra page preceding each paper. I am aware that violations of this declaration may lead to subsequent withdrawal of the degree.

# Acknowledgements

First of all, I would like to thank my thesis advisor Hans-Gerd Maas for his support and trust during the last years. I would also like to thank Prof. Iwaszczuk and Prof. Luhmann for reviewing this thesis. I would like to thank Prof. Förstner for awakening my interest in photogrammetry. I thank Ferdinand Maiwald for proofreading and Robert Blaskow and David Mader for their support in the writing phase of this thesis. I thank Anette Eltner, Robert Blaskow and Christian Mulsow for their co-authorship of the papers in this thesis. I would also like to thank all current and former colleagues at the TU Dresden Photogrammetry group for their great collaboration. Last but not least, I thank my grandparents, my parents, my sister, and my wife for their unconditional support and trust.

To Jonah.

# Abstract

Due to climate change, extreme weather events and their effects like flash floods have become more frequent in recent years, causing major damages to landscapes and infrastructure, and endangering human lives. This is one of the reasons why it is desirable to monitor rivers and fluvial processes. Besides gauging water levels and flow velocities, it is necessary to know the morphology of the river as precisely as possible. In hydrodynamic flood modelling, for example, high-resolution river models are needed for a prediction of the flooded areas. By comparing the river profile before and after a flood event, conclusions can be drawn about changes in the landscape. River surveys need to record both, the banks above the water level, and the river bottom below the water level. This dissertation presents the conception and implementation of a photogrammetric multisensor system on an uncrewed water vehicle (UWV). It proves that a well-equipped UWV is a useful measurement system for recording the topography of rivers above and below the water level providing relevant information about the river morphology.

For deriving accurate 3D information above the water level, a camera and a mobile lidar are attached to the platform. For the bathymetric measurement of the river profile, a single beam echo sounder is initially used. The individual sensors record data in different coordinate systems. For a combined model of the river, these measurements need to be fused in one coordinate system. Therefore, a calibration method is presented that enables the determination of the relative orientations between all sensors.

Lidar measurements provide detailed information about the riverbanks. Since the sensor is used on a moving platform, georeferencing of the lidar points is a crucial issue of the method. Thus, position and orientation of the scanner must be known during the entire acquisition. This is usually solved with an inertial navigation system (INS), consisting of an IMU (inertial measurement unit) and a GNSS (global navigation satellite system) receiver. However, due to shadowing from vegetation on the banks and multipath effects from the water surface, satellite positioning is likely to be error prone on rivers. IMUs are furthermore influenced by electric fields on the small platform, resulting in drifts in the orientation determination. Therefore, an independent method for determining the position and orientation of the platform is developed. For this purpose, time-lapse images of the camera on the UWV are used. Their orientation is determined with photogrammetric multi-image methods. Based on a relative orientation between the camera and the scanner coordinate system, these orientations are used for georeferencing the lidar points. This calibration method enables a fast and highly accurate determination of the relative orientation.

For the monitoring of the river bathymetry, the UWV carries a single beam echo sounder. However, echo sounding has principal limitations in shallow waters. This issue can be solved with a laser triangulation sensor combining the contrary properties of both sensors. Laser triangulation enables highly accurate line scans in close range applications and is an established method in optical industrial surveying. In order to use the method for underwater measurements, the sensor system, consisting of a camera and a laser line projector, must first be placed in a waterproof glass housing. The lightsheet emitted by the laser line projector is then refracted several times at the interfaces from air to glass and from glass to water. A method for the exact modelling and calibration of these ray paths is presented. In addition, the accuracy potential is evaluated in a theoretical assessment. In practical tests, which were first carried out in the laboratory, the previously estimated submillimetre accuracy was confirmed.

The results of the previously presented methods offer approaches for further developments. A comparison of INS and image-based methods shows the advantages of a potential combination of both approaches. The integration of the laser triangulation sensor into the set-up of the UWV confirms the potential of the combination of echo sounder and triangulation measurements. An exemplary multi temporal river survey approves the capability of the UWV for deformation analyses. Further, an improved laser triangulation sensor with a multi-line laser diode may enable more extensive underwater measurements.

# Zusammenfassung

Bedingt durch den Klimawandel treten seit einigen Jahren vermehrt extreme Wetterereignisse auf. Deren Auswirkungen, wie Sturzfluten, verursachen große Schäden an Landschaften und Infrastruktur und gefährden Menschenleben. Um Sturzfluten besser modellieren zu können, ist die Überwachung von Flüssen und fluvialen Prozessen erforderlich. Neben der Messung von Wasserständen und Fließgeschwindigkeiten an Pegeln, muss die Morphologie des Flusses so genau wie möglich bekannt sein. Bei der hydrodynamischen Hochwassermodellierung werden beispielsweise hochaufgelöste Flussmodelle für eine Vorhersage der überfluteten Gebiete benötigt. Durch den Vergleich des Flussprofils vor und nach einem Hochwasserereignis können Rückschlüsse auf Veränderungen in der Landschaft gezogen werden. Für umfassende Flussvermessungen müssen sowohl die Ufer oberhalb als auch die Flusssohle unterhalb der Wasseroberfläche erfasst werden. In dieser Dissertation wird die Konzeptionierung und Umsetzung eines photogrammetrischen Multisensorsystems auf einem unbemannten Wasserfahrzeug (uncrewed water vehicle – UWV) vorgestellt. Die Arbeit zeigt, dass ein UWV ein nützliches Messsystem zur Erfassung der Topographie von Flüssen ober- und unterhalb des Wasserspiegels ist und somit die Erfassung der Morphologie des Flusses ermöglicht.

Um präzise 3D-Informationen der Ufer zu erhalten, werden eine Kamera und ein mobiler Laserscanner an der Plattform angebracht. Für die Vermessung des Flussprofils wird zunächst ein Einzelpunkt-Echolot eingesetzt. Die einzelnen Sensoren zeichnen ihre Daten in unterschiedlichen Koordinatensystemen auf. Für ein kombiniertes Modell des Flusses müssen diese Messungen in einem gemeinsamen Koordinatensystem fusioniert werden. Daher wird eine Kalibriermethode vorgestellt, die die Bestimmung der relativen Orientierungen zwischen den Sensoren ermöglicht.

Laserscanner-Messungen liefern detaillierte Informationen über die Uferbereiche. Da der Sensor auf einer beweglichen Plattform eingesetzt wird, ist die Georeferenzierung der 3D-Punkte von großer Bedeutung. Dafür müssen Position und Orientierung des Scanners während der gesamten Erfassung bekannt sein. Dies wird üblicherweise mit einem inertialen Navigationssystem (INS) gelöst, das aus einer IMU (Inertial Measurement Unit) und einem GNSS-Empfänger (Global Navigation Satellite System) besteht. Aufgrund von Abschattungen durch die Ufervegetation und Mehrwegeeffekten an der Wasseroberfläche ist die Satellitenortung auf Flüssen jedoch oft fehleranfällig. Darüber hinaus werden IMUs durch elektrische Felder auf der kleinen Plattform beeinflusst, was zu Drifts bei der Orientierungsbestimmung führt. Daher wird eine unabhängige Methode zur Bestimmung der Position und Orientierung der Plattform vorgestellt. Dazu werden die Bilder der auf dem UWV angebrachten Kamera verwendet. Deren Orientierung wird mit photogrammetrischen Mehrbildverfahren bestimmt. Basierend auf einer relativen Orientierung zwischen Kamera- und Scanner-Koordinatensystem werden diese Orientierungen zur Georeferenzierung der Laserscannerpunkte verwendet. Die entwickelte Kalibriermethode ermöglicht eine schnelle und hochgenaue Bestimmung der relativen Orientierung

Das Echolot liefert aufgrund des Messprinzips in flachen Gewässern üblicherweise keine exakten Daten. Mittels eines Lasertriangulationssensors können auch in diesen Bereichen Gewässertiefen gemessen werden, weshalb eine Kombination beider Verfahren aufgrund ihrer gegensätzlichen Eigenschaften sinnvoll ist. Die Lasertriangulation ermöglicht hochgenaue linienhafte Abtastungen im Nahbereich und ist eine etablierte Methode in der optischen Industrievermessung. Um das Verfahren für Unterwassermessungen nutzen zu können, muss das Sensorsystem, bestehend aus einer Kamera und einem Linienlaser, zunächst in einem wasserdichten Glasgehäuse untergebracht werden. Das von der Laserdiode emittierte Licht wird dann an den Grenzflächen von Luft zu Glas und von Glas zu Wasser mehrfach gebrochen. Es wird eine Methode zur exakten Modellierung und Kalibrierung dieser Strahlengänge vorgestellt. Außerdem wird das theoretische Genauigkeitspotenzial evaluiert. In praktischen Versuchen, die zunächst im Labor durchgeführt wurden, konnte die zuvor abgeschätzte Submillimeter-Genauigkeit des Systems bestätigt werden.

Die Ergebnisse der vorgestellten Methoden bieten Ansätze für Weiterentwicklungen. Ein Vergleich von INS- und bildbasierten Verfahren zeigt die Vorteile der potenziellen Kombination beider Ansätze. Die Integration des Lasertriangulationssensors in den Messaufbau des UWV zeigt das Potential der Kombination von Echolot- und Triangulationsmessungen. Eine beispielhaft durchgeführte multitemporale Flussvermessung bestätigt die Leistungsfähigkeit des UWV für Deformationsanalysen. Darüber hinaus könnte ein verbesserter Lasertriangulationssensor mit einer Mehrlinien-Laserdiode flächenhafte Unterwassermessungen ermöglichen.



# Contents

<b>1 Introduction.....</b>	<b>1</b>
1.1 Objectives of this Thesis.....	1
1.2 Outline of this Thesis.....	1
<b>2 Development of the Uncrewed Water Vehicle.....</b>	<b>3</b>
2.1 Development .....	3
2.2 Sensor Configuration.....	4
2.2.1 INS and GNSS .....	4
2.2.2 Panorama Camera.....	4
2.2.3 RGB Camera .....	5
2.2.4 Mobile Lidar.....	5
2.2.5 Echo sounder .....	5
2.2.6 Underwater Laser Triangulation.....	5
2.3 System architecture .....	5
<b>Sardemann et al., 2018: Acquisition of geometrical Data of small Rivers with an Unmanned Water Vehicle .....</b>	<b>7</b>
Abstract.....	9
1. Introduction .....	9
2. The Unmanned Water Vehicle .....	9
2.1 Components.....	9
2.2 Time Synchronization .....	9
2.3 Calibration.....	10
3. Data Acquisition.....	10
4. Data Processing and Results.....	11
4.1 Lidar.....	11
4.2 Echo Soundings.....	12
4.3 Fusion with UAV data.....	12
5. Summary and Outlook.....	12
Acknowledgements .....	12
References.....	12
<b>Sardemann et al., 2023: Camera-aided orientation of mobile lidar point clouds acquired from an uncrewed water vehicle.....</b>	<b>15</b>
Abstract.....	17
1 Introduction .....	17
1.1 Uncrewed Water Vehicles as Multisensor Platforms.....	17
1.2 Camera based Orientation .....	18
1.3 Outline and Innovations of this Article.....	19
2 Platform Orientation Determination .....	19
3 Calibration of Lidar to Camera Orientation .....	20
3.1 Geometric Calibration .....	20
3.2 Time Synchronization .....	22
4 Lidar Point Transformation .....	22
5 Experiments.....	23
5.1 Reference Point Cloud.....	24
5.2 Calibration and Synchronization results .....	24
5.3 Transformation of mobile lidar point clouds .....	25
6 Accuracy Analysis.....	27
6.1 Theoretical Accuracy .....	27
6.2 Experimental Results.....	29

7	Conclusions .....	31
	References.....	32
<b>Sardemann et al., 2021: Strict geometric calibration of an underwater laser triangulation system.....35</b>		
	Abstract.....	37
1	State of the art.....	37
2	Method .....	37
2.1	Set-Up .....	37
2.2	Line Detection.....	38
2.3	Depth Determination .....	38
2.4	Calibration.....	38
2.5	Measurement Volume .....	39
3	Experiments and Results.....	39
3.1	Calibration.....	39
3.2	Measurements.....	40
4	Summary and Outlook.....	40
	Acknowledgements .....	40
	References.....	40
<b>Sardemann et al., 2022: Accuracy Analysis of an Oblique Underwater Laser Lightsheet Triangulation System.....41</b>		
	Abstract.....	43
	Zusammenfassung.....	43
1	Introduction .....	44
2	Background and State of the Art.....	44
3	System Design.....	46
4	Measurement Method .....	47
4.1	Line Measurement.....	47
4.2	Determination of 3D coordinates.....	48
4.3	Calibration.....	49
5	Measurement Volume.....	50
6	Statistical Accuracy Analysis .....	50
6.1	Influence of image measurement.....	51
6.2	Influence of Camera IOR .....	51
6.3	Influence of Camera EOR .....	51
6.4	Influence of Laser EOR.....	51
6.5	Influence of Refractive Index .....	51
6.6	Summarized Estimation of Accuracies .....	51
7	Experiments and de Facto Achieved Accuracies .....	52
7.1	Reference Objects.....	52
7.2	Single Profile Scan .....	52
7.3	Scanning Mode.....	53
8	Summary and Outlook.....	54
9	Declaration .....	54
	References.....	54
<b>3</b>	<b>Syntheses.....</b>	<b>59</b>
3.1	Comparison of INS- and Camera-based Orientation .....	59
3.1.1	Boresight alignment and lever-arm calibration.....	59
3.1.2	Theoretical error estimation.....	60
3.1.3	De facto achieved accuracies.....	60
3.1.4	Comparison of both approaches .....	61
3.2	Integrating the underwater laser triangulation sensor .....	62

<b>4 Ongoing and Future Work</b> .....	<b>64</b>
4.1 Deformation Analysis .....	64
4.2 Multiline Underwater Laser Triangulation .....	65
4.2.1 Calibration .....	66
<b>5 Conclusion</b> .....	<b>69</b>
<b>6 Literature</b> .....	<b>71</b>
<b>List of Figures</b> .....	<b>77</b>
<b>List of Tables</b> .....	<b>81</b>
<b>List of Abbreviations</b> .....	<b>83</b>



# 1 Introduction

Unattended multisensor platforms enable measurements in remote or difficult-to-reach areas. There are three main areas of application: on the ground, in the air and in the water. When it comes to the surveying of rivers, unattended aerial vehicles (UAVs) and uncrewed water vehicles (UWVs) are both capable of measuring the river morphology. The following paragraph will discuss the differences between aerial and water vehicles and highlight the specific advantages and applications of UWVs for river measurements.

UAVs are commonly used for environmental monitoring. Recent surveys can be found in Eltner et al. (2022) and Manfreda and Dor (2023). In hydrographic applications, UAVs can be used for various tasks: Tauro et al. (2016) measure the stream surface flow velocity by applying Large Scale Particle Image Velocimetry on stream floaters. Water levels can be obtained using cameras (Eltner et al., 2018). The topography of the water bottom can also be measured with cameras (Mulsow et al., 2020) and with lidar bathymetry (Mandlbürger et al., 2020). Both methods are restricted by the visibility through the water. While camera based methods only allow for measurements in visible depths (one Secchi depth), bathymetric lidars allow for measurements in two Secchi depths.

Especially when there is dense vegetation on the bank area of a river, optical sensors have difficulties measuring through the vegetation. Mandlbürger et al. (2022) had to put a lot of effort into flight planning to survey rivers with UAV-based lidar bathymetry because of vegetation on the banks. Trees demand the UAVs to fly in greater altitudes, therefore decreasing the accuracy. UWVs that are navigated on the river operate under the trees and are therefore able to map the river profile and the riverbanks without occlusions. When satellite-based positioning is also obstructed by the vegetation, camera based orientation methods can be applied. UWVs observe the riverbanks from a closer range and from a more favourable angle than UAVs, especially when the banks are steep. Bathymetric measurements from an UWV can be conducted with a single beam echo sounder. It is therefore not restricted by Secchi depth. In shallow areas, where echo sounders are limited, laser triangulation can be applied to gather high accurate depth measurements.

## 1.1 Objectives of this Thesis

The work presented in this thesis aims to present a photogrammetric sensor system for an uncrewed water vehicle. This includes sensor modelling and calibration concepts. The UWV is supposed to be used for both measurements above and under the water level. For mapping above the water, it will be equipped with a mobile lidar and a camera. The thesis will present methods for the generation of a mobile lidar point cloud of riverbanks. It will furthermore present a georeferencing method of mobile lidar points collected at rivers, where satellite-based positioning is challenged by multipath and shadowing effects. This will be realized using camera orientation methods.

The UWV can furthermore be equipped with an underwater laser triangulation sensor for bathymetric mapping in shallow waters. A sensor system will be presented that is suitable for that task. The sensor will be modelled, especially considering the influence of refraction. The potential of that sensor system will be evaluated in a laboratory environment. A feasibility study will show that the sensor system can be attached to the UWV, revealing that the triangulation sensor can complete the photogrammetric UWV sensor system for above and under water measurement tasks.

## 1.2 Outline of this Thesis

This thesis is a cumulative dissertation. Its main content is given in four scientific publications framed by an introduction and a synthesis. The following chapter presents the development process and set-up of the UWV that was developed for this thesis. This is followed by the four scientific papers, with each being preceded by an information page giving the most relevant information on the paper.

The first two papers address the topic of surveying of riverbanks with an UWV. The first paper (Acquisition of geometrical Data of small Rivers with an Unmanned Water Vehicle, 2018) gives an

overview of the complete measurement system and evaluates its capabilities using an exemplary recorded data set. The second paper (Camera-aided orientation of mobile lidar point clouds acquired from an uncrewed water vehicle, 2023) deals with the positioning of the UWV for the generation of mobile lidar point clouds. It takes up a problem from the first paper: The positioning of the UWV with an inertial navigation system (INS) tends to be error-prone on rivers and not as accurate as for example on aerial vehicles. Therefore, a camera-based positioning method is presented and its usefulness for the creation of a mobile laser scanner point cloud is analysed.

This is followed by two articles on the topic of optical underwater measurements. In these, an underwater laser triangulation sensor is presented that enables sub-millimetre accurate bathymetric measurements at close range. The third paper (Strict geometric calibration of an underwater laser triangulation System, 2021) presents the measurement method and calibration principle using a simulation and briefly analyses its feasibility using a prototype. In the fourth paper (Accuracy Analysis of an Oblique Underwater Laser Lightsheet Triangulation System, 2022), test measurements with a dedicated sensor system are presented and analysed in a comprehensive accuracy analysis.

The four papers are followed by a synthesis, which compares and combines their ideas. Subsequently, it is analysed which further work in this field should be addressed in the future. Some of these approaches have already been implemented and initially investigated. Their results will be presented, while it is worthwhile to conduct further in-depth research on them. The work is concluded with a summary and an overview of the main advantages of this work.

## 2 Development of the Uncrewed Water Vehicle

The following sections describe the development of the multisensor uncrewed water vehicle that was developed for this thesis. First, a short overview of the development stages that led to the current version is given in section 2.1. This is followed by a description of the components of the UUV and their purposes in section 2.2 and the wiring and data transfer in section 2.3.

### 2.1 Development

The scope of the UUV is to map rivers and their bank areas. It therefore needs two attributes: It needs to float on water and it needs (multiple) sensors for the measurement task. A first rudimentary version, that fulfilled both of these requirements was developed using empty plastic bottles glued to a wooden board and an aluminium profile with a camera attached to it (Fig. 2.1a). This platform was already capable of capturing a point cloud of the riverbanks using Structure from Motion (SfM). In order to get a point cloud with the correct scale, either direct or indirect georeferencing had to be considered. Indirect georeferencing could be achieved using control points on the banks, which had to be measured for example with a total station or with GNSS (global navigation satellite system). For direct georeferencing of the camera based point cloud, an INS system, consisting of an IMU and a GNSS receiver had to be attached to the platform and both temporally and geometrically synchronised with the camera. A laser scanner enables a reliable and scaled measurement of a point cloud of the banks in greater distances and operates under worse lightning conditions than a camera based measurement. The river profile under water can be measured either with echo sounding or with optical measurements using an underwater camera or a laser triangulation system. All the before mentioned sensors for measurement and positioning added up to a payload that requires a more stable platform. Depending on the depth and flow velocity of the river, it is also favourable that the UUV is operated from a safe distance, i.e. from the bank. A remote controlled platform was therefore equipped with the sensors (Fig. 2.1b).



Fig. 2.1: Development stages of the UUV. From a towed wooden board on plastic bottles (a) to a remote controlled multi sensor platform (b).

The platform is a Seafloor Systems HyDrone remote controlled catamaran. It has a size of 117 cm x 74 cm, a maximum payload of 11 kg, a top speed of 3 m/s and a battery endurance of 5 – 8 h depending on payload and speed. The sensors were attached using a customized design built out of aluminium profiles and 3D printed parts that were designed using CAD software (Fig. 2.2).

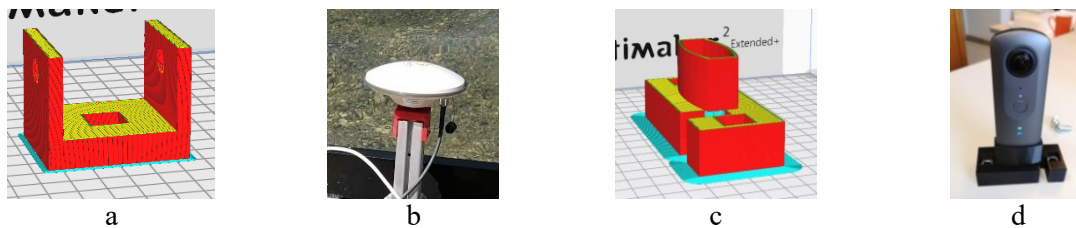


Fig. 2.2: 3D printed sensor mounts for antenna (a, b) and panorama camera (c, d). CAD models in 3D printer software (a, c) and resulting parts (b, d).

## 2.2 Sensor Configuration

The latest version of the UWV is equipped with sensors for positioning and for measurement above and under the water level. Fig. 2.3 shows the sensors and the according system architecture, which will be described in section 2.3.



Fig. 2.3: Sensor configuration and system architecture of the multisensory system. The arrow colours indicate different types of connection: dark blue: antenna cable, green: serial port, black: USB, orange: Ethernet, grey: Ethernet (not yet included in the system). The light blue waves indicate a WIFI connection.

### 2.2.1 INS and GNSS

Position and orientation of the platform is determined using an inertial navigation system (INS) and an additional multiband GNSS receiver. The MEMS-based INS Advanced Navigation Spatial combines an IMU with accelerometers, gyroscopes, magnetometers and a pressure sensor with a one-frequency GNSS receiver. The measurements are combined in real time using a Kalman filter, resulting in roll and pitch accuracies of  $0.1^\circ$  and a heading accuracy of  $0.2^\circ$ . The INS is synchronised with GPS time and serves as the reference clock for the multisensory system. In order to get more precise positions in post processing, a multiband GNSS receiver Swift Navigation Piksi Multi is also included. It records raw GNSS data that can be combined with the data collected from a base station on the riverbank in a post processing kinematic (PPK) process. The resulting positions have accuracies of 2 cm (lateral) to 3 cm (height). Both sensors are connected to the same geodetic antenna using an active antenna splitter. The relative orientation between the INS and the other sensors on board the UWV is described in section 3.1.1.

### 2.2.2 Panorama Camera

A Ricoh Theta V panorama camera records  $360^\circ$  images in time-lapse mode with 1 Hz. The camera is a combination of two fisheye lenses with two 8-megapixel image sensors directed in the opposite direction. Both can be considered as individual fisheye cameras with an opening angle of approx.  $190^\circ$ . The combination of both leads to a dual fisheye image, with two hemispherical views with a slight overlap. The interior orientation and the relative orientation between both fisheye cameras has been calibrated using a cubic calibration field. Using this information enables the generation of a spherical panoramic image. The panorama images can be used for a virtual panorama walk along the river. Furthermore, they can be used in SfM software for the generation of both a point cloud of the riverbanks and the track of the platform. The relative orientation calibration between a  $360^\circ$ -camera and mobile

lidar is described in Sardemann et al. (2018), using a Samsung Gear 360. The Ricoh Theta V camera uses an Android operating system, allowing the user to program specific apps. For this thesis, an Android app was developed and implemented, that records a dual-fisheye image every second and saves the exact millisecond time stamp in the image filename.

### 2.2.3 RGB Camera

Additionally to the 360°-camera, a central perspective camera can be used for SfM as well. A Panasonic DMX-GX80 camera with 15.8 megapixels and a 14 mm lens can be attached to either side of the UWV imaging the respective riverbank. A calibration method for the relative orientation between central perspective camera and other sensors on the UWV is presented in Sardemann et al. (2023). The central perspective camera has a sensor that is larger than the one in the panorama camera and a higher quality lens that enables clearer images. While those images allow for a higher SfM accuracy based on the image quality, they have the drawback, that they only show one riverbank and not both as the panorama camera. The fact, that there is usually both water and sky visible in the image, results in a bad utilisation of image space (Sardemann et al., 2023). Comparing position and orientation accuracies from the central perspective RGB to those from the 360° camera reveals that the advantages of both sensors counterbalance each other resulting in similar accuracies (see 4.1). A possible solution including the advantages of both methods would be using two synchronised central perspective cameras looking in the opposite direction.

### 2.2.4 Mobile Lidar

As a direct optical method for the measurement of 3D point clouds of the riverbanks, a Velodyne Puck VLP-16 mobile lidar has been attached to the UWV. It allows for the generation of scaled point clouds independent from contrast of the object or lighting conditions. Using mobile lidar data demands a known position and orientation of the scanner for every recorded lidar point. This can either be achieved using IMU and GNSS (Sardemann et al., 2018) or camera based poses (Sardemann et al., 2023). Those methods deliver the orientation and position for either the INS or the camera, requiring a relative orientation between scanner coordinate system and camera coordinate system (Sardemann et al., 2023) or IMU coordinate system (3.1.1).

### 2.2.5 Echo sounder

For bathymetric measurements, a single beam echo sounder has been attached. It measures the water depth underneath the UWV. In order to get an extensive river profile, a zig-zag-trajectory with subsequent interpolation can be applied as shown in Sardemann et al. (2018).

### 2.2.6 Underwater Laser Triangulation

A more sophisticated method especially for shallow water areas is the use of an underwater laser triangulation system (Sardemann et al., 2022). The sensor consists of a laser line projector and a camera, which are submerged into the water in the same watertight housing. Applying the methods of laser triangulation together with the laws of refraction enables highly accurate profile measurements. Depending on the base length between camera and laser and the turbidity and therefore visibility of the water restrains this method to a rather short measurement volume. The system can be installed on the UWV in a watertight housing, which is submerged into the water. A first test of installing the system on the UWV and a simulation of its benefit is presented in section 3.2. It is especially beneficial in shallow water areas, where echo sounders are usually unable to measure, serving as a useful extension to the bathymetric sensor set-up.

## 2.3 System architecture

The sensor measurements have to be recorded and if possible, time synchronised on board the UWV. The according connections and the main tasks of these connections are depicted in Fig. 2.3. Two

Raspberry Pi single board computers are encased in a waterproof box together with the GNSS receiver board, the IMU, an antenna splitter and the mobile lidar interface box. Fig. 2.4 shows the waterproof central control unit, that can also be seen mounted on the UWV in Fig. 2.1a. Specific board holders were designed and 3D-printed. The echo sounder is connected to the IMU where its measurements are assigned a timestamp. The IMU and echo sounder signal is connected to the first Raspberry Pi, which is also used to configure the GNSS receiver. The mobile lidar is connected to the second Raspberry Pi sending its measurements to be stored. The mobile lidar is furthermore connected with the IMU that sends a pulse-per-second signal for synchronisation with GPS time. The Raspberry Pis are controlled from a laptop or mobile phone via WIFI. The data is assessed in post processing on a stationary computer after the measurement.

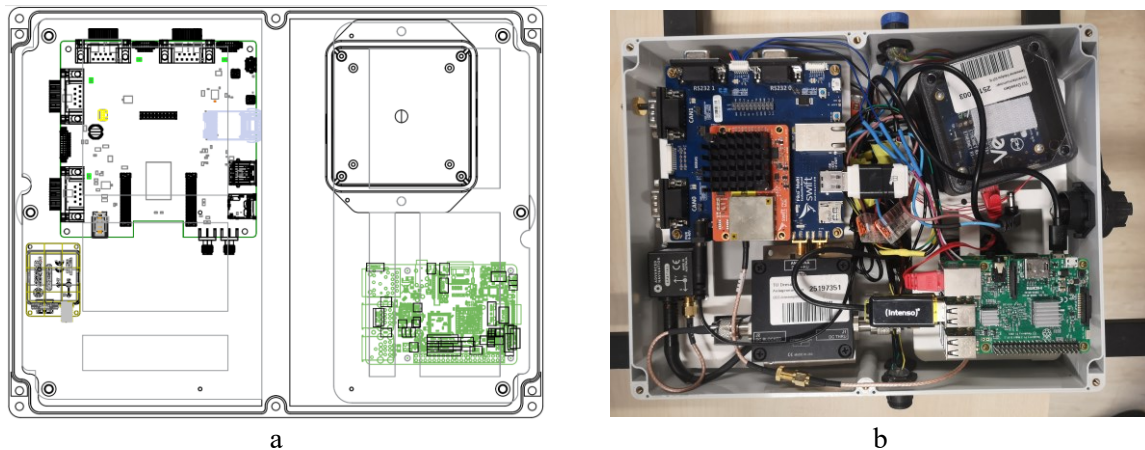


Fig. 2.4: Central control unit. a: concept for 3D-printing the board holder; b: assembled box including cables. The box includes two stacked Raspberry Pi computers (bottom right), the lidar interface box (top right), the GNSS receiver (top left), the IMU (bottom left) and antenna splitter (bottom centre, only in b).

Multiple functions and programs have to be used for the sensor configuration and to retrieve the data from the different sensors. The following scripts and programs were developed, implemented and compiled on the Unix-based Raspberry Pi operating system:

- The IMU is addressed based on ANSI-C function from the Advanced Navigation SDK. First, a magnetic calibration is started and monitored, and then the logging of the IMU data is started by activating the important packages.
- Python scripts that are based on the Swift Navigation SDK have been implemented to configure the GNSS receiver.
- The lidar data is logged by capturing the incoming Ethernet data using the script based program tshark.
- Shell scripts are implemented on the Raspberry Pi that first synchronise the system time with GPS time and then combine the aforementioned programs to start the measurement process. It gives a feedback to the user about the logged data. The shell scripts can be started from a Laptop or Smartphone that is connected to the Raspberry via WIFI.

For the panorama camera, an Android app was implemented, starting a time-lapse image recording and writing the millisecond-timestamp in the filename of the images. The camera is connected to the Raspberry before and after a measurement, to find the offset between the camera clock and GPS time.

Scientific Paper 1:

# Sardemann et al., 2018: Acquisition of geometrical Data of small Rivers with an Unmanned Water Vehicle

Hannes Sardemann, Anette Eltner, Hans-Gerd Maas

## Published in:

The International Archives of the Photogrammetry, Remote Sensing and Spatial Information Sciences, Volume XLII-2, 2018

<https://doi.org/10.5194/isprs-archives-XLII-2-1023-2018>

Published on 30 May 2018

## Additional Information:

The page numbers have been changed from 1023 – 1027 to 9 – 13 for this thesis.

This work has been presented in an oral presentation at the ISPRS TC II Mid-term Symposium “Towards Photogrammetry 2020”, 4–7 June 2018, Riva del Garda, Italy

## Authors’ Contributions following CRediT (Contributor Roles Taxonomy):

Conceptualization	Sardemann, Maas, Eltner
Data Curation	Sardemann
Formal Analysis	Sardemann
Funding Acquisition	Maas
Investigation	Sardemann
Methodology	Sardemann
Project Administration	Maas, Eltner
Resources	Maas
Software	Sardemann
Supervision	Maas
Validation	Sardemann, Eltner
Visualization	Sardemann
Writing – original draft	Sardemann
Writing – review & editing	Eltner, Maas



# ACQUISITION OF GEOMETRICAL DATA OF SMALL RIVERS WITH AN UNMANNED WATER VEHICLE

Hannes Sardemann\*, Anette Eltner, Hans-Gerd Maas

Institute of Photogrammetry and Remote Sensing, Technische Universität Dresden, Germany  
(hannes.sardemann, anette.eltner, hans-gerd.maas)@tu-dresden.de

## Commission II, ICWG I/II

**KEY WORDS:** Unmanned Water Vehicle, Multi-sensor Platform, Mobile Mapping, Lidar, Echo Sounder, Flash Flood

### ABSTRACT:

Rivers with small- and medium-scaled catchments have been increasingly affected by extreme events, i.e. flash floods, in the last years. New methods to describe and predict these events are developed in the interdisciplinary research project EXTRUSO. Flash flood events happen on small temporal and spatial scales, stressing the necessity of high-resolution input data for hydrological and hydrodynamic modelling. Among others, the benefit of high-resolution digital terrain models (DTMs) will be evaluated in the project.

This article introduces a boat-based approach for the acquisition of geometrical and morphological data of small rivers and their banks. An unmanned water vehicle (UWV) is used as a multi-sensor platform to collect 3D-point clouds of the riverbanks, as well as bathymetric measurements of water depth and river morphology. The UWV is equipped with a mobile Lidar, a panorama camera, an echo sounder and a positioning unit. Whole (sub-) catchments of small rivers can be digitalized and provided for hydrological modelling when UWV-based and UAV (unmanned aerial vehicle) based point clouds are fused.

## 1. INTRODUCTION

In the last decades, an increasing number of high-intensity rainfall events has been observed in central Europe (Mueller and Pfister, 2011). This results in a higher risk for flash-flood events, especially in rivers with small catchments. Flash floods develop in a short time and on a small scale, making them difficult to monitor and predict with traditional methods (Borga et al., 2008). Therefore, new hydrological and hydrodynamic models have to be developed and existing models have to be adapted in order to be able to predict flash floods. These models require input data with high temporal and spatial resolution. In this article, a system for the acquisition of high-resolution point clouds is presented.

A remote controlled UWV, equipped with multiple sensors for mapping its surroundings above and underneath the water level, is presented. In combination with UAV-based point clouds, which cover a broader area of the river catchment, DTMs of sub-catchments can be generated. This can serve as an input for hydrodynamic modelling and for the prediction of flooded areas. Furthermore the data can be used for post event analysis.

## 2. THE UNMANNED WATER VEHICLE

The boat platform used in this study is the remote controlled survey boat HyDrone by Seafloor Systems. The catamaran was originally designed for bathymetric surveys and has been rebuilt by the authors to the needs of a multisensor-platform (Figure 1). The platform has a maximum speed of 20 kts, a payload of 11.3 kg and a battery endurance of 5-8 hours, depending on the survey speed. The batteries are placed inside the pontoons, supplying power for the thrusters as well as for the attached sensors.

### 2.1 Components

Above water level, the mobile lidar Velodyne Puck scans the riverbanks in 16 profiles with up to 0.3 million points per second

and a maximum range of 100 m. The 3D point accuracy is +/- 3 cm. A Samsung Gear 360 records a panoramic video of the survey that can be used for point cloud colorization. The 360° camera consist of two fisheye lenses with a field of view of >180° each, pointing to opposite directions, enabling a full panorama with 7.3 megapixels. The positioning unit is the GNSS-supported IMU Spatial by Advanced Navigation. It has 0.6 m horizontal, 1 m vertical, and 0.2° rotation angle accuracy. The single-beam echo sounder EchoLogger ECT400 measures water depth with 10 Hz maximum ping rate. For sensor control and data storage, two RaspberryPi computers are deployed on the boat. The collected data is processed after the survey in the office.

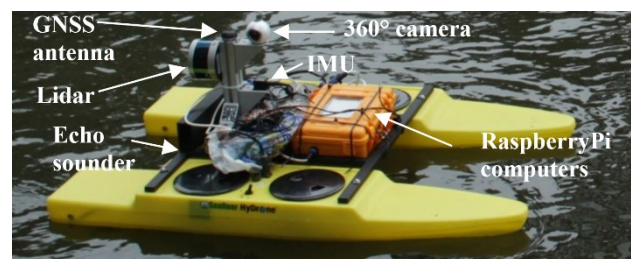


Figure 1. Multi Sensor UWV with Lidar, 360° camera, echo sounder (hidden) and GNSS-supported IMU

### 2.2 Time Synchronisation

In order to enable data fusion between the sensors, they need to have synchronized clocks. The IMU clock is synchronized with GPS time with 50 ns accuracy and serves as time reference. It sends a time stamp every second to the Velodyne lidar via RS232 interface. The lidar's internal clock is 0.05 ns accurate and assigns a time stamp to every 3D point measurement. The echo sounder transmits its data also via RS232 to the IMU, where it is stored and a time stamp is assigned. Time synchronisation is more challenging for the consumer camera Samsung Gear 360, since it is not possible to trigger the camera externally. One

\* Corresponding author

approach is to attach a display to the boat, showing the IMU time with a high refresh rate. Having the full spherical view of the 360° camera, a spot can be found, where the display is always in the camera's field of view and does not conclude the areas of interest, i.e. the riverbanks. The time stamp can be read manually or with optical character recognition for every frame. First tests revealed that this approach works well in indoor environments, but fails when the sun reflects from the display.

### 2.3 Calibration

Besides time synchronization, calibration of the relative orientations is crucial for data fusion and point cloud colorization. The calibration procedure introduced by Mader et al. (2014) was adapted for that purpose. The used calibration field consists of seven cones with coded markers on their surface. A reference point cloud of the calibration field was created with bundle adjustment using a SLR camera, scale bars and the coded markers. A dense point cloud was created, using structure from motion (SfM) and the results of the marker-based bundle adjustment (Figure 2a).

The UWV is placed in the middle of the calibration field, so that all cones are inside the fields of view of both lidar and 360° camera (Figure 2b-c). The exterior orientation of both sides of the camera are determined using marker-based space resection, applying a fisheye camera model. Interior orientation parameters were calibrated prior and then fixed. The 3D reference points are transformed from object space to the camera coordinate system:

$$\mathbf{X}_{\text{cam}} = \mathbf{R}_{\text{ref}}^{\text{cam}} \cdot (\mathbf{X}_{\text{ref}} - \mathbf{X}_{\text{ref}}^0) \quad (1)$$

where:  $\mathbf{X}_s = \begin{bmatrix} x_s \\ y_s \\ z_s \end{bmatrix}$  = point in specific coordinate system s

$\mathbf{X}_{\text{ref}}^0$  = coordinates of projection centre

$\mathbf{R}_{s_1}^{s_2}$  = rotation matrix from coordinate system s1 to s2

The origin of the camera coordinate system lies in the projection centre with its axes parallel to image space. According to an equidistant fisheye model, camera coordinates are projected into image space:

$$x' = x'_0 + c \cdot \alpha \cdot \frac{X_{\text{cam}}}{\sqrt{X_{\text{cam}}^2 + Y_{\text{cam}}^2}} + \Delta x' \quad (2)$$

$$y' = y'_0 + c \cdot \alpha \cdot \frac{Y_{\text{cam}}}{\sqrt{X_{\text{cam}}^2 + Y_{\text{cam}}^2}} + \Delta y' \quad (3)$$

where:  $x', y'$  = image coordinates

$x'_0, y'_0$  = principle point

$c$  = focal length

$\alpha$  = incidence angle of image ray

In order to determine the relative orientation between camera and lidar, the exterior orientation of the lidar relative to the reference coordinate system has to be found:

$$\mathbf{X}_{\text{ref}} = \mathbf{T}_{\text{lidar}}^{\text{ref}} + \mathbf{R}_{\text{lidar}}^{\text{ref}} \cdot \mathbf{X}_{\text{lidar}} \quad (4)$$

where:  $\mathbf{T}_{s_1}^{s_2}$  = translation vector from coord. system s1 to s2

The transformation can be determined fitting cones in the reference and in the lidar point cloud (Figure 2d). Each cone is parameterized by its apex, the direction of its axis, and its opening angle. In a 'cone coordinate system', where the  $z_c$ -axis points along the cone axis and  $x_c$  and  $y_c$  are perpendicular to it, all points on the cone's surface follow the equation

$$(x_{i,j})_c^2 + (y_{i,j})_c^2 - (z_{i,j})_c^2 \cdot \tan^2 \beta_j \quad (5)$$

where:  $x_c, y_c, z_c$  = surface points in cone coordinates  
 $\beta$  = cone opening angle  
 $i$  = point index  
 $j$  = cone index

In order to fit cones in the reference point cloud, the surface points have to be transformed from reference coordinates to cone coordinates:

$$(\mathbf{X}_{i,j})_c = (\mathbf{X}_{\text{ap},j})_{\text{ref}} + (\mathbf{R}_{\text{ref}}^c)_j \cdot (\mathbf{X}_{i,j})_{\text{ref}} \quad (6)$$

where:  $\mathbf{X}_{\text{ap}}$  = apex of cone

Since cones are rotation invariant around their main axis, only two rotation angles are needed to parameterize  $\mathbf{R}_{\text{ref}}^c$ . Those angles determine the direction of the cone axis in the reference coordinate system. Together with the apex position, they build the five parameters of each cone. From equations (4), (5) and (6), the  $(5 \cdot j)$  cone parameters and the relative orientation between lidar and reference coordinate system can be determined in a least squares adjustment.

Calibration of the relative orientation between IMU and sensors is a crucial requirement for the generation of a point cloud from a moving UWV. The translation vector, i.e. lever arm, is determined directly within the photogrammetric bundle adjustment by attaching a marker to the GNSS antenna. The boresight alignment can be simplified, because of the sensor configuration: IMU and lidar are attached to the same aluminium profile with the IMU pointing towards the front of the UWV and the lidar coordinate system being aligned perpendicular to it. The echo sounder is attached to the same profile. Since the accuracy of the echo soundings is expected to be in the range of a few centimetres, the offset was measured directly with a ruler. The calibration process will be extended with a lever arm and boresight-alignment calibration and a consideration of the echo sounder offset in future experiments. This will lead to an improved accuracy, especially when longer distances will be measured.

### 3. DATA ACQUISITION

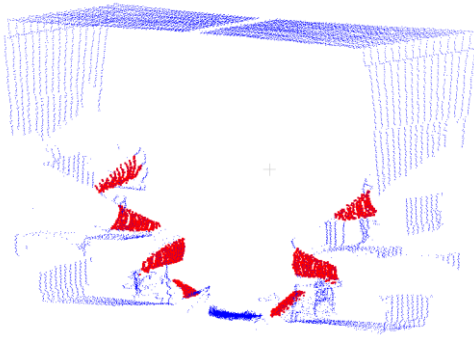
First test surveys were conducted in a small river in Saxony, Germany. Segments of the river 'Freiberger Mulde' have been monitored in other research projects recently and an UAV based point cloud of the river surrounding areas already exists. Parts of the riverbanks are covered by trees and can therefore not be seen from the air. These gaps can be filled with UWV surveys. There is also no high-resolution model of the riverbed available yet, which can be recorded from UWV surveys.



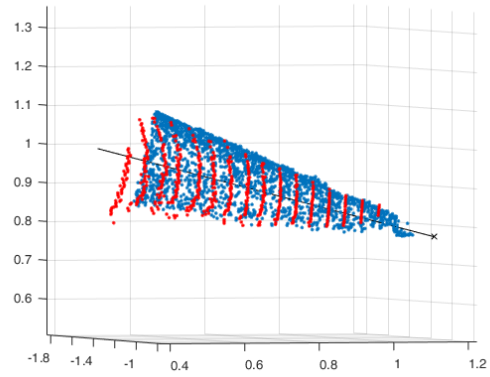
(a)



(b)



(c)



(d)

Figure 2. Calibration of relative orientations. The cone-based calibration field is measured with a SLR camera and used as reference (a). Markers are detected in the 360° camera images and used for space resection (b). Cones are detected in the Lidar point cloud (c) and fitted with cones from the reference point cloud (d).

Considering the survey configuration, a good trade-off has to be found between a dense point coverage for the single beam echo sounder and a feasible point density of the lidar point cloud. Krüger et al. (2018) show that a good data acquisition strategy has to be chosen for the interpolation of single point echo soundings. A zigzag trajectory was implemented at the Freiberger Mulde (Figure 3).



Figure 3. Survey configuration on the river Freiberger Mulde. The surveyed river segment is approx. 1.5 km long.

#### 4. DATA PROCESSING AND RESULTS

During the UWV surveys, RaspberryPi computers are used to start the sensor recording and to store the data on a hard drive. The data is then post processed in the office.

##### 4.1 Lidar

To gather a complete point cloud of the riverbanks, the lidar scanlines that were recorded along the river have to be combined according to the IMU position. In total, approx. 75 million points have been recorded. Boresight-Alignment and lever arm have to be considered in order to transform the recorded lidar points into the IMU coordinate system:

$$\mathbf{X}_{\text{IMU}} = \mathbf{T}_{\text{lidar}}^{\text{IMU}} + \mathbf{R}_{\text{lidar}}^{\text{IMU}} \cdot \mathbf{X}_{\text{lidar}} \quad (7)$$

Since every point has a time stamp, they can be transformed into world coordinates, i.e. UTM:

$$\mathbf{X}_{\text{world}} = \mathbf{T}_{\text{IMU}}^{\text{world}} + \mathbf{R}_{\text{IMU}}^{\text{world}} \cdot \mathbf{X}_{\text{IMU}} \quad (8)$$

The 360° camera images can be used for colorization of the point cloud. By projecting lidar points into image space of a frame recorded at a specific time, with known exterior and interior

orientation, the colour value can be taken from the image. This projection follows equations (1) – (3).

Figure 4 shows the acquired lidar point cloud of the riverbanks. All points are shown either monochrome or intensity coloured because the 360° camera has not been synchronized, yet. Figure 5 shows a more detailed view of a small segment on the northern bank including intensity values. The riverbank in the front is mapped with sub-centimetre resolution. The direct surroundings of the river, including the riverbank itself, the vegetation, and the buildings are important factors for hydrodynamic modelling and for modelling the flooded area during a flood event.



Figure 4. Lidar point cloud of a 1.5 km segment of the river Freiberger Mulde.



Figure 5. Details of the lidar point cloud. Colours show intensity. Only one bank of the river is shown, including trees and buildings in the background.

#### 4.2 Echo Soundings

The best strategy for single beam echo sounder measurements with subsequent interpolation is to record cross sections with small gaps (Santillan et al., 2016). However, this was impractical, because the riverbanks would be out of the lidar’s field of view. Therefore, a zigzag configuration was the best trade-off.

Interpolation of meandering rivers is influenced by an interaction of points, which are nearby in a world coordinate system, but not along the river. Echo sounder measurements need to be transformed into a flow-oriented coordinate system to minimize these influences (Merwade et al., 2016). Since there is no river centre line available, lidar points of the riverbanks have to be utilized for this transformation. The interpolation method plays a minor role compared to the data acquisition strategy, with Kriging performing best out of several interpolation methods (Krüger et al., 2018). Hence, Ordinary Kriging is applied.

Figure 6 includes the interpolation result as a depth coded point cloud. The river continues with a weir in the west, resulting in deep water in that area. As expected, there are also deeper parts where the river is narrower.

#### 4.3 Fusion with UAV data

The point clouds of the river bathymetry and the geometry of the riverbanks are both geo-referenced. Figure 6 shows them both in UTM coordinates, together with a point cloud that was generated with SfM from UAV images. For further use in the EXTRUSO project, a DTM will be derived from that point cloud.

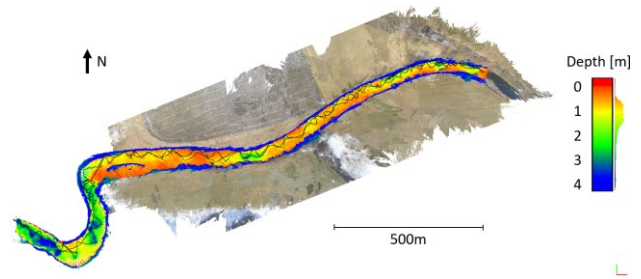


Figure 6. Results of a test surveys on the river Freiberger Mulde. Lidar points of the riverbanks are coloured in blue. The black line shows the UUV track in a zigzag configuration. The echo sounder data is depth coded. An UAV-based SfM point cloud maps the surroundings of the river.

### 5. SUMMARY AND OUTLOOK

This article shows the potential of boat-based river mapping for extreme event analysis and modelling. A design and calibration method for an unmanned water vehicle was presented. Point clouds of the river morphology recorded from an UUV can fill the gaps of UAV-based point cloud data. For further use for hydrodynamic modelling, DTMs have to be created. Hence, filtering the vegetation that covers the riverbanks has to be considered. The potential of using the multi-echo functionality of the mobile lidar for vegetation filtering should be evaluated in oncoming experiments. UUV based point clouds can also be used for post flood event analysis. Future work should include multi temporal acquisition and change detection of the river morphology before and after a flood event.

The accuracy of the acquired point clouds needs to be evaluated in more detail. Direct geo-referencing with IMU and GNSS leads to an error in the order of 50 cm. RTK should be used to minimize that error. Additionally, control points can be added. Adapting the calibration method with a boresight alignment and lever arm calibration and by designing a calibration method that includes the echo sounder will also improve the accuracy, especially when larger distances will be surveyed. The interpolation results for bathymetry highly depends on point density. In order to improve the interpolation accuracy, an acquisition strategy with higher zigzag frequency should be applied. Using a depth sensor with a larger field of view could also densify the point cloud. A triangulation sensor applying a laser line and an underwater camera will be tested in coming experiments.

### ACKNOWLEDGEMENTS

These investigations are part of the research project “Extreme events in small and medium catchments (EXTRUSO)” funded by the EU ESF ‘Junior Research Groups’ program under grant no. 100270097. The UAV point cloud was provided by the Chair of Geoinformatics at the TU Dresden and was developed in the research project “BOOT-Monitoring”, which is part of the funding program ‘ReWaM’ by the German Federal Ministry of Education and Research.

### REFERENCES

- Borga, M., Gaume, E., Creutin, J. D., and Marchi, L., 2008. Surveying flash floods: gauging the ungauged extremes. *Hydrological processes*, 22(18), 3883. <https://doi.org/10.1002/hyp.7111>

Krüger, R., Karrasch, P., and Bernard, L., 2018. Evaluating Spatial Data Acquisition and Interpolation Strategies for River Bathymetries. A. Mansourian et al. (eds.), *Geospatial Technologies for All*, Springer International Publishing, 3-24, [https://doi.org/10.1007/978-3-319-78208-9\\_1](https://doi.org/10.1007/978-3-319-78208-9_1)

Mader, D., Westfeld, P., and Maas, H.-G., 2014. AN INTEGRATED FLEXIBLE SELF-CALIBRATION APPROACH FOR 2D LASER SCANNING RANGE FINDERS APPLIED TO THE HOKUYO UTM-30LX-EW. *The International Archives of the Photogrammetry, Remote Sensing and Spatial Information Sciences XL-5*, 385-393. <https://doi.org/10.5194/isprsarchives-XL-5-385-2014>

Merwade, V. M., Maidment, D., R., and Goff, J. A., 2006. Anisotropic considerations while interpolating river channel bathymetry. *Journal of Hydrology* 332, 732-741. <https://doi.org/10.1016/j.jhydrol.2006.06.018>

Mueller, E. N., and Pfister, A., 2011. Increasing occurrence of high-intensity rainstorm events relevant for the generation of soil erosion in a temperate lowland region in Central Europe. *Journal of Hydrology*, 411(3), 266-278, <https://doi.org/10.1016/j.jhydrol.2011.10.005>

Santillan, J. R., Serviano, J. L., Makinano-Santillan, M., and Marqueso, J. T., 2016. INFLUENCE OF RIVER BED ELEVATION SURVEY CONFIGURATIONS AND INTERPOLATION METHODS ON THE ACCURACY OF LIDAR DTM-BASED RIVER FLOW SIMULATIONS. *The International Archives of the Photogrammetry, Remote Sensing and Spatial Information Sciences XLII-4/W1*, 225-235. <https://doi.org/10.5194/isprs-archives-XLII-4-W1-225-2016>



Scientific Paper 2:

# Sardemann et al., 2023: Camera-aided orientation of mobile lidar point clouds acquired from an uncrewed water vehicle

Hannes Sardemann, Robert Blaskow, Hans-Gerd Maas

## Published in:

Sensors 2023, 23(13), 6009

<https://doi.org/10.3390/s23136009>

Published on 28 June 2023

## Additional information:

The page numbers have been changed from 1 – 16 to 17 – 33 for this thesis.

## Authors' Contributions following CRediT (Contributor Roles Taxonomy):

Conceptualization	Sardemann, Blaskow, Maas
Data Curation	Sardemann
Formal Analysis	Sardemann
Funding Acquisition	Maas
Investigation	Sardemann, Blaskow
Methodology	Sardemann
Project Administration	Maas
Resources	Maas
Software	Sardemann
Supervision	Maas
Validation	Sardemann, Blaskow, Maas
Visualization	Sardemann
Writing – original draft	Sardemann
Writing – review & editing	Blaskow, Maas



# Camera-aided orientation of mobile lidar point clouds acquired from an uncrewed water vehicle

Hannes Sardemann <sup>1</sup>, Robert Blaskow <sup>1</sup> and Hans-Gerd Maas <sup>1\*</sup>,

<sup>1</sup> Institute of Photogrammetry and Remote Sensing, Technische Universität Dresden, 01062 Dresden

\* Correspondence: hans-gerd.maas@tu-dresden.de

**Abstract:** This article presents a system for recording 3D point clouds of riverbanks with a mobile lidar mounted on an uncrewed water vehicle. The focus is on the orientation of the platform and the lidar sensor. Rivers are areas where the conditions for highly accurate GNSS can be sub-optimal due to multipath effects from the water and shadowing effects by bridges, steep valleys, trees, or other objects at the riverbanks. Furthermore, a small measurement platform may have an effect on the accuracy of orientations measured by an IMU, for instance caused by electromagnetic fields emitted by the boat rotors, the lidar and other hardware decreasing IMU accuracy. As an alternative, we use exterior orientation parameters obtained by photogrammetric methods from the images of a camera on the boat capturing the riverbanks in time-lapse mode. Using control points and tie points on the riverbanks enables geo referenced position and orientation determination from the image data, which can then be used to transform the lidar data into a global coordinate system. Main influences on the accuracy of the camera orientations are the distance to the riverbanks, the size of the banks and the amount of vegetation on them. Besides this, the quality of the camera-orientation-based lidar point cloud also depends on the time synchronization of camera and lidar. The paper describes the data processing steps for the geometric lidar-camera integration and delivers a validation of the accuracy potential. For quality-assessment of a point cloud acquired with the described method, a comparison with terrestrial laser scanning has been carried out.

**Keywords:** Mobile Lidar · Multisensor Platform · River Bank Mappings · Uncrewed Water Vehicle

## 1. Introduction

Survey vessels are a useful and efficient tool to record water bodies and their surrounding shore and bank areas. Small, shallow, hazardous or restricted waters may require the use of small uncrewed water vehicles (UWVs). Besides their application in the ocean (Bai et al., 2022), uncrewed surface vehicles (USVs), as they are also called, can be applied in inland waters. One application is the acquisition of three-dimensional (3D) point clouds and models of the morphology of small rivers where crewed survey vessels are oversized and conventional surveying methods are too time consuming. UWVs furthermore allow for automatic data acquisitions.

### 1.1 Uncrewed Water Vehicles as Multisensor Platforms

Equipping crewed or uncrewed vessels with multiple sensors enables the acquisition of high-resolution 3D point clouds. Here, a distinction can be made between the measurements of above- and underwater geometries. Echo sounders are commonly used to record river bathymetry. While larger rivers allow for survey vessels with multibeam echo sounders (de Jong et al., 2013), smaller rivers require echo sounders mounted on UWVs (Lewicka et al., 2021). Optical methods enable depth measurements in even shallower areas (Mandlbürger, 2022). Mapping above the water level can be realized by cameras and

lidarsystems. Terrestrial laser scanners operated in profiler mode can be mounted on larger platforms, like crewed motorboats. Schneider and Blaskow (2021) use such a system to capture the shoreline of two lakes. Compact lidars can be mounted on UWVs as well. Zhang et al. (2020) use a combination of a camera and a Velodyne Puck lidar to detect objects on the water in a marine environment.

Besides oceans and lakes, rivers are a possible area of application for multisensor water vehicles. Tauro et al. (2018) show that the modelling of hydrological processes demands new measurement methods, especially at low cost for worldwide applications. High-resolution 3D models of the river morphology can be helpful to improve the prediction and understanding of flood events. Analyzing the impact of a flood event on the riverbanks helps to get a better understanding of the process. Especially when rivers are located in forested areas, riverbanks are often difficult to measure with camera equipped airborne systems such as unattended aerial vehicles (UAVs) due to shadowing effects. Water vehicles may operate under the trees and are able to capture the riverbanks with optical sensors at close range. UWVs are a low cost alternative to large survey vessels that enable a broad application not only in small rivers. Cheng et al. (2021) recorded a multi-sensor dataset containing data of different waterways recorded with a lidar system, stereo cameras, GNSS, IMU and radar mounted on an UWV.

### *1.2 Camera based Orientation*

To generate a 3D point cloud from a mobile lidar on a moving platform, position and orientation of the sensor has to be known for every captured 3D lidar point. The most common method to determine the orientation of an outdoor operated platform is the combined use of data from a Global Navigation Satellite System (GNSS) receiver and an inertial measurement unit (IMU) (Elhashash et al., 2022). In this case, the orientation of the platform is calculated using the IMU's high temporal resolution acceleration and rotation rate measurements. Due to the drift vulnerability of an IMU and for georeferencing, the trajectory calculation by IMU is supported by GNSS measurements that are usually available in a lower temporal frequency. Shading caused by high vegetation surrounding the rivers or high rock formations may lead to an interruption of the GNSS measurement. In cases where the GNSS signal is not available or erroneous and where no (expensive) high quality IMU is available, the pose of a multisensor platform may be also derived from photogrammetric multi-image triangulation.

Simultaneous localization and mapping (SLAM) algorithms provide poses in real time. Using SLAM with camera images or video image sequences is often referred to as visual odometry (Nister et al., 2004). Macario Barros et al. (2022) did a recent review on visual SLAM algorithms. SLAM has the disadvantage that it tends to drift, when the path is not closed (dead reckoning). Especially in river mapping, it is often favorable to steer the boat only in one direction, which is mostly downstream, leading to an open path. When real time is not needed, structure from motion (SfM) techniques may be utilized for 3D point cloud and camera orientation determination in post processing. Herein, using control points enables georeferenced and scaled 3D point clouds as well as sensor orientation parameters that do not suffer from drifts. Liebold and Maas (2014) presented a georeferencing procedure for a moving platform, integrating camera and lidar observations.

The aforementioned methods give the position and orientation of a mobile platform referring to the coordinate system of the camera that was used for the orientation determination. However, lidar points are recorded in a scanner coordinate system defined by the lidar. When both sensors are fixed on the platform, a relative orientation between scanner and camera coordinate system can be calibrated in order to determine the orientation of the lidar. Existing methods often use planar objects for the calibration of the relative orientation. Ying et al. (2014) move a checkerboard pattern through the object space to calibrate the extrinsic calibration of a camera and a line scan lidar. Kim et al. (2020) also use a planar chessboard pattern for the extrinsic calibration of a 16-channel 3D lidar and a system of six cameras. These methods require the manual interaction of a user moving

the plane. Pusztai and Hadjer (2017) use a 3D calibration setup consisting of multiple boxes. Their method only needs one viewpoint for the calibration, once the calibration field is established. The resulting accuracies are in the range of centimeters to decimeters for the position determination.

### 1.3 Outline and Innovations of this Article

This article analyses the quality of camera-based position and orientation determination for a lightweight lidar system. A method will be presented, that can be used for the georeferencing of a mobile lidar point cloud when GNSS and IMU poses are not available or erroneous. This is particularly important for UWVs navigated on small rivers. The method relies on a camera that is operated in video or time-lapse mode, a mobile lidar, control points on the riverbanks and a low- to mid-cost IMU to bridge very short time periods. First, the basic concept of the camera based lidar sensor orientation will be presented (section 2). Then, the strategy for the underlying calibration of the geometric relative orientation as well as time-sync between scanner and camera will be presented (section 3). The geometric calibration process (section 3.1) only requires the acquisition of an image and a lidar scan. Once the calibration field is established and measured, it can be used for a quick and mm-accurate geometric calibration of a mobile mapping camera-lidar system. Subsequently, a kinematic calibration process for the temporal synchronization of lidar and camera will be presented in section 3.2. A calibrated system enables the transformation of lidar points, which will be described in section 4. For the evaluation of the presented method, it has been applied for an UWV-based measurement of a riverbank (section 5). The resulting point cloud will be compared to reference measurements that were generated with a terrestrial laser scanner (TLS) (section 6). The paper ends with a conclusion and suggestions for future research (section 7).

## 2. Platform Orientation Determination

In order to reference and merge 3D points recorded with a mobile lidar, the orientation of the scanner has to be known. It is therefore important to know the current position and orientation of the platform during the entire measurement. The common choice to determine position and orientation of a mobile platform (outdoors) is to use differential GNSS for the position and IMU for the orientation. IMU measurements on an UWV are highly affected by electromagnetic fields, emitted from the scanner, the boat rotors and other electrical equipment on the platform. The most prominent effect of that can be observed in the heading. GNSS is furthermore influenced by multipath effects on the water surface and shadowing by objects on the riverbanks.

This article therefore evaluates the quality of camera-based orientations for platform orientation determination. Processing time-lapse images of a camera in a SfM procedure including control points, results in georeferenced positions and orientations for all images referring to the pose of the camera coordinate system ( $ccs$ ). Thus, the camera trajectory in the world coordinate system ( $wcs$ ) can be derived from the image data. For every image  $i$ , there is a six-parameter transformation matrix  ${}^{wcs}M_{ccs_i}(\omega, \phi, \kappa, X, Y, Z)$  containing its exterior orientation, using homogeneous coordinate transformations. In order to acquire convergent image observations, a zig-zag trajectory should be applied (Figure 1). Each object point is then seen in multiple images from multiple directions. The interior orientation of the camera can be determined with self-calibration in the same process.

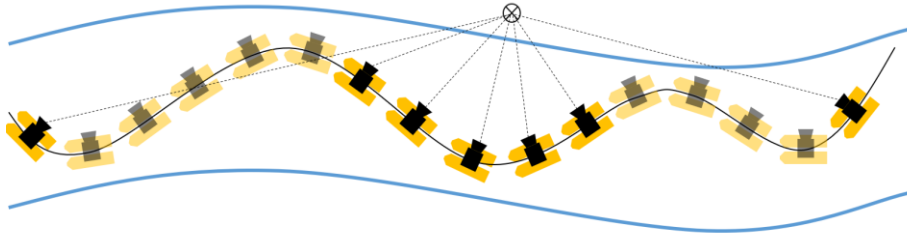


Figure 1: UWV trajectory. A zig-zag trajectory enables the visibility of object points from various distances and directions.

### 3. Calibration of Lidar to Camera Orientation

The exterior orientations of an UWV can be used to register the lidar frames and to combine them to a point cloud of the riverbanks. The platform orientations based on the camera images define the position and orientation of the camera coordinate system in world coordinates. The 3D points measured by the lidar are recorded in the scanners own coordinate system ( $scs$ ). In order to transform lidar points from  $scs$  to  $wcs$ , using the orientations from section 2, the relative orientation between  $scs$  and  $ccs$  has to be calibrated. This calibration consists of two steps: a geometric calibration of boresight alignment and lever arm, and a time synchronization between camera and lidar clock.

#### 3.1. Geometric Calibration

The geometric calibration process is an improved version of the method presented in Mader et al. (2014). Therein, a cone-based calibration procedure was used for the intrinsic calibration of a 2D laser scanner, while we use a similar method for the calibration of relative orientations between  $scs$  and  $ccs$ , which was not part of the Mader method. It consists of several cones placed in different distances and heights in the field of view of both the lidar and the camera (Figure 2). The geometry of the calibration field has to be known with high accuracy resulting in exact positions and orientations of the cones in a project coordinate system ( $pcs$ ).

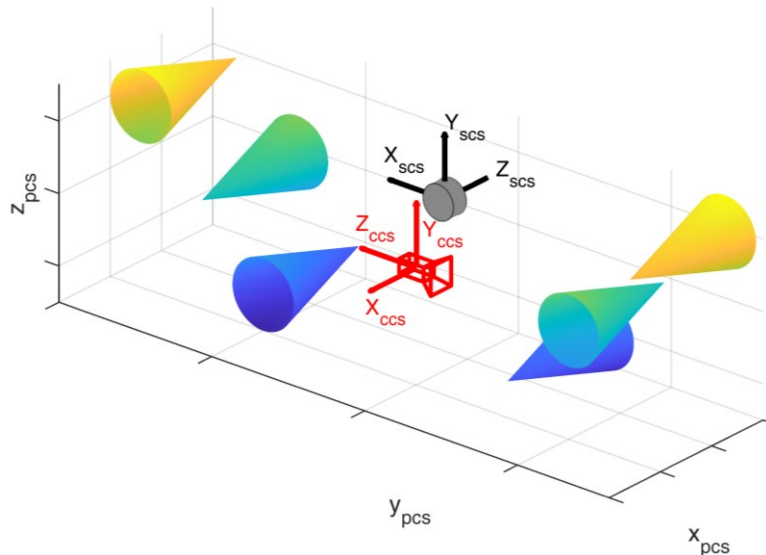


Figure 2: Calibration field set-up. Camera (red) and lidar (grey) both observe the cone-based calibration field that is located in a project coordinate system ( $pcs$ ). Six cones are placed on two sides of the scanner in different distances and heights in order to determine the relative orientation between the camera coordinate system ( $ccs$ ) and scanner coordinate system ( $scs$ ). The cones are color coded according to the height.

Each cone has its own cone coordinate system ( $cocs$ ), with the origin in its apex  $a$  and the  $z$ -axis along the cone's axis (Figure 3). Points  $p_j$  on the surface of a cone can be transformed into cone coordinates by a translation with the apex coordinates and a rotation from  $pcs$  to  $cocs$  ( ${}^{cocs}R_{pcs}$ ). The rotation includes only two angles ( $\lambda, \theta$ ), since the cone is rotation invariant:

$${}^{cocs}\begin{bmatrix} x \\ y \\ z \end{bmatrix}_{p_j} = {}^{cocs}R_{pcs}(\lambda, \theta) \cdot \left( {}^{pcs}\begin{bmatrix} x \\ y \\ z \end{bmatrix}_{p_j} - {}^{pcs}\begin{bmatrix} x \\ y \\ z \end{bmatrix}_a \right) \quad (1)$$

All cone points fulfil the condition

$$\left( {}^{cocs}x_{p_j} \right)^2 + \left( {}^{cocs}y_{p_j} \right)^2 - \left( {}^{cocs}z_{p_j} \right)^2 \tan^2(\alpha) = 0, \quad (2)$$

where  $\alpha$  is the opening angle of the cone.

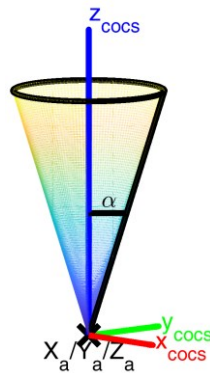


Figure 3: Cone coordinate system. Each cone of the calibration field has its own coordinate system ( $cocs$ ) defined by its apex coordinates  $(x_a, y_a, z_a)$ , the  $z$ -axis along the cone's axis and an opening angle  $\alpha$ .

A camera image and a 3D point cloud frame are recorded for at least one static position. The cones are visible both in the lidar frames and in the images. Figure 4 shows the synthetic camera image and lidar frame recorded from the positions depicted in Figure 3.

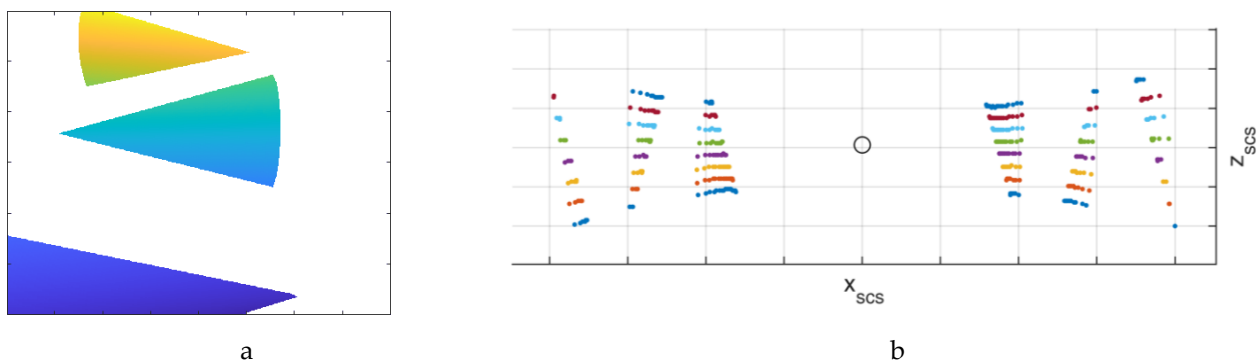


Figure 4: a: Synthetic camera image of the cone-based calibration field, where the color of the cones indicates height, b: synthetic lidar frame of the cone-based calibration field, where the color indicates the scanline ID of a lidar with 8 scanlines with  $4^\circ$  steps.

The exterior orientation  ${}^{pcs}M_{cscs_i}$  of the camera image can be determined in project coordinates using spatial resection. Furthermore, the individual cones have to be cropped from the scanner frame and used for an orientation determination of the lidar point clouds. This can be achieved in a common least squares optimization, with the model from equations (1) and (2). Eq. (2) is applied for the reference points (in  $pcs$ ) of all six cones

and simultaneously for the lidar points (in  $scs$ ) of the same cones. For the lidar points, the model has to be extended with a transformation from scanner into project coordinates, before they can be fitted with the same cone parameters. The lidar orientation in project coordinates is determined relatively to the camera using the relative orientation matrix  ${}^{ccs}M_{scs}$ , which has to be determined in the optimization process:

$${}^{pcs}\begin{bmatrix} x \\ y \\ z \\ 1 \end{bmatrix} = {}^{pcs}M_{ccsi} \cdot {}^{ccs}M_{scs} \cdot {}^{scs}\begin{bmatrix} x \\ y \\ z \\ 1 \end{bmatrix} \quad (3)$$

The total number of parameters is six per cone (cone parameters) and six for the relative orientation ( ${}^{ccs}M_{scs}$ ), totaling in 42 parameters when six cones are used. While the calibration strategy is suitable to be used with only one single recording, it can still be extended with more positions for a better accuracy and liability.

### 3.2. Time synchronization

Mobile lidars can usually be synchronized with GPS time. Some cameras, especially customer cameras on the other hand do not support external triggering. In this case, indirect time synchronization has to be applied. For that purpose, the calibration process is extended by a second step. Besides the static positions that were used for the relative geometric orientation determination in the previous section, a dynamic acquisition is performed. The UUV is moved along the calibration field and images are recorded in video or time-lapse mode. Exterior orientations are calculated for all of those images as well. At the same time, RTK positions have to be recorded with a GNSS receiver on board the UUV. In order to get the offset between GPS time and camera clock, GNSS and camera positions need to be available in the same world coordinate system  $wcs$ . The calibration field therefore has to be georeferenced. For every image observation time  $T_i$  (in GPS time) the GNSS antenna is located at an offset  $(dx, dy, dz)$  in camera coordinates:

$${}^{ccs}\begin{bmatrix} dx \\ dy \\ dz \end{bmatrix}_{T_i} = {}^{wcs}M_{ccsi}^{-1} \cdot {}^{wcs}\begin{bmatrix} X \\ Y \\ Z \end{bmatrix}_{GNSS_{T_i}} \quad (4)$$

However, images are not recorded with a GPS timestamp  $T_i$ , but with a camera timestamp  $t_i$ . The temporal offset  $dt$  between camera time and GPS time can be defined by  $T = t + dt$ . Substituting and rearranging eq. (4) leads to an equation with four unknowns ( $dt, dx, dy, dz$ ) that can be solved in a Gauss-Helmert optimization:

$${}^{wcs}M_{ccsi}^{-1} \cdot {}^{wcs}\begin{bmatrix} X \\ Y \\ Z \end{bmatrix}_{GNSS_{(t_i+dt)}} - {}^{ccs}\begin{bmatrix} dx \\ dy \\ dz \end{bmatrix} = 0 \quad (5)$$

## 4. Lidar Point Transformation

Given the relative orientation and temporal synchronization of camera and scanner enables the transformation of 3D lidar points using the respective image orientation. Thus, a 3D point has to be transformed from the scanner coordinate system to the image coordinate system and from image coordinates to world coordinates using eq. (3). The orientation of one image is used for the registration of one lidar frame. A lidar frame is hereby defined as a full  $360^\circ$  rotation of the lidar centered on the image recording time with half of the rotation before and the other half after the image was taken. Since the platform is not still during the acquisition of one lidar frame, using the same camera-based pose for all points of one frame would lead to an error in the georeferenced point cloud. Thus, the pose used for the orientation of each lidar point is interpolated using the IMU. Therefore, relative orientations between IMU and camera orientation are determined for all image

timestamps and interpolated for the lidar-point timestamps. The missing orientations between the image acquisition times can then be derived from the IMU measurements by applying the interpolated relative orientations.

## 5. Experiments

The methods presented in the previous paragraphs were tested with experimental data acquired with an UWV that was navigated along a river. The UWV used for this study is a Seafloor HyDrone (Figure 5). It is equipped with a two-frequency GNSS receiver (Swiftnav Piksi Multi) and an IMU (Advanced Navigation Spatial) for position and orientation determination. Riverbanks are observed with a mobile lidar (Velodyne Puck). The Velodyne Puck is a very popular lidar sensor in low or mid cost mobile mapping systems, offering the advantages of a good price-performance ratio and easy integration. It records 500,000 points per second in 16 scanlines with horizontal and vertical fields of view of 360° and 30°. It has a maximum distance of 100 m and a 3D-point accuracy of 3 cm. The UWV was first presented in Sardemann et al. (2018) in an earlier stage of development. It may also be equipped with an underwater laser triangulation sensor (Sardemann et al., 2022). The sensor platform is designed to be modular so that different sensors can be attached according to the measurement task.



Figure 5: The uncrewed water vehicle used in this study. The Velodyne Puck lidar is attached vertically on the back, while the Panasonic camera is oriented towards the left in the direction of travel, protected with a soft plastic cover.

For this study, a Panasonic DMX-GX80 camera with 15.8 megapixels and a 14 mm lens was attached to the UWV for camera-based orientation determination and to capture high-resolution images of the riverbank. The camera was chosen because of an available time lapse mode, but could be replaced by other models as well. It can be installed on either sides of the UWV according to the riverbank of interest. The camera was used in time-lapse mode with an image acquisition rate of 1 Hz.

The UWV was applied on the river Freiburger Mulde in Germany to map the riverbanks. The acquisition was done in only one transect, where the platform was steered downstream in a zigzag pattern from one riverside to the other (Figure 6a). The measurement took 17 minutes steering with mean speeds of 0.4 m/s (lateral) and 7 °/s (angular). The right-hand riverbank is the area of interest being a sloped railroad embankment with large stones and small vegetation like bushes and small trees (Figure 6b). The river had a width of approx. 40 m at that location and time of measurement.

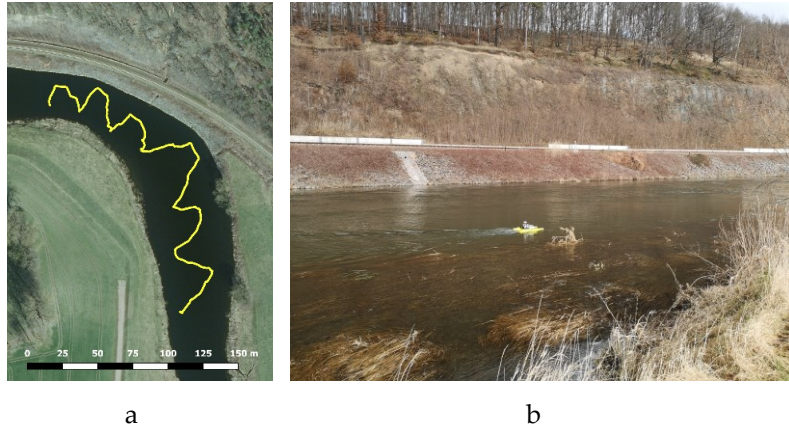


Figure 6: Freiberger Mulde. a: GPS-track of the transect. b: UWB on the river with the railroad bank in the background.

### 5.1. Reference Point Cloud

A reference point cloud has been recorded with terrestrial laser scanning using a Riegl VZ400i (Figure 7). Three stations have been recorded and merged. Georeferencing was realized with circular targets that were measured with RTK GNSS. The point cloud has a mean point spacing of 2.5 cm. The 3D point accuracy specified by the manufacturer is 3 mm at 50 m distance.



Figure 7: Terrestrial laser scan of the Freiberger Mulde (reflectance colored).

### 5.2. Calibration and Synchronization results

The calibration process from section 4 was performed before the measurement. The relative orientation between scanner and camera was determined from three viewpoints where the UWB was placed in the middle of the calibration field. Since time synchronization was solved in a subsequent step, static positions were needed to assign camera image and lidar frame. The positions differ mostly in orientation. Coded markers were attached to the surface of the cones and the geometry of the calibration field was measured with superior accuracy: First, only the marker coordinates were determined in a bundle block adjustment using Aicon 3D Studio. Including additional scale bars with known length allowed for object point accuracies of <1 mm herein. The 3D coordinates and their corresponding image measurements were imported into Agisoft Metashape, where a dense point cloud was determined. For time synchronization, the reference point cloud of the calibration field was furthermore georeferenced, using circular targets that were measured with RTK.

The exterior orientation parameters of the three Panasonic camera images were determined in the same SfM project, with interior orientation being calibrated in advance. The corresponding Velodyne positions were estimated relatively to the image orientations using equations (1) – (3) in an optimization process (Figure 8). The lever arm between lidar

and camera has a length of 16 cm and has been determined with a standard deviation of  $<1$  mm. The relative orientation angles have standard deviations of  $<1$  mrad. The exact values can be found in Table 1.

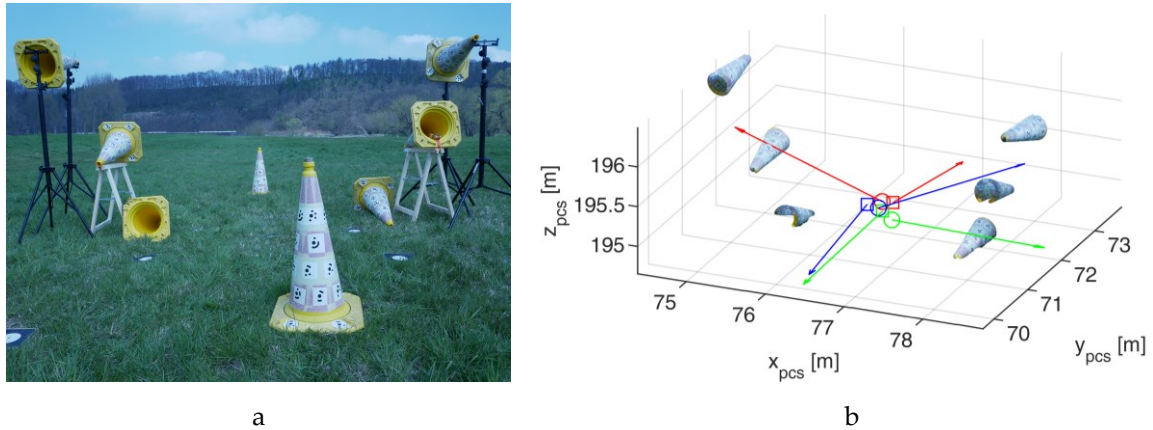


Figure 8: Geometric calibration. a: Calibration field consisting of 8 cones, from which only the 6 horizontal ones were used for calibration. b: Camera and scanner positions determined using the cones from the dense point cloud. Circles show camera positions and squares show scanner positions. The arrows give the orientation of the z-axis. Same color indicates same UWV position.

The same calibration field was used for the time synchronization of camera clock and GPS time. For that purpose, the UWV was moved around the calibration field with images taken every second. The images have been oriented in the SfM project. A RTK track of the boat-based GNSS antenna has been recorded at the same time with a frequency of 10 Hz. Figure 9 shows both tracks. Eq. (5) was used to determine the temporal and spatial offsets between both tracks. The calibrated time offset shows a standard deviation of 0.004 s.

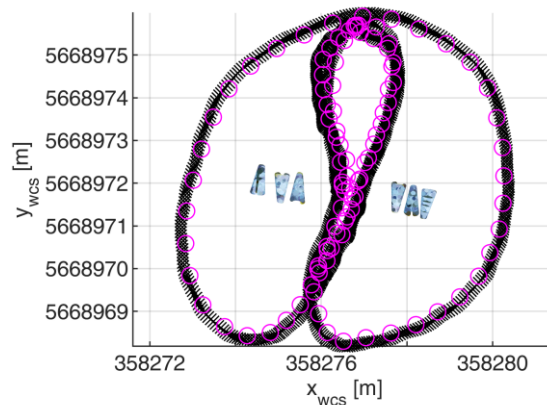


Figure 9: Time offset calibration. Image positions are shown as pink circles while the GNSS track is shown as black x.

### 5.3. Transformation of mobile lidar point clouds

Images were gathered every second along the track shown in Figure 6a and were aligned in Agisoft Metashape, using control points that were measured with RTK (Figure 10).

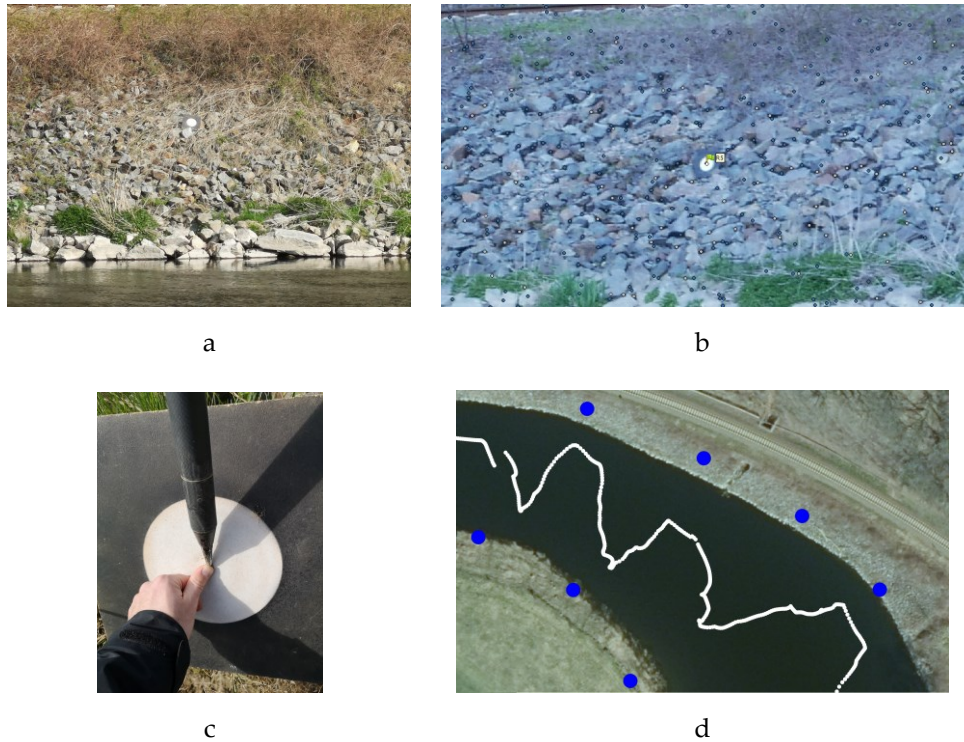


Figure 10: Image Orientation determination and georeferencing. a: Control point on river-bank, b: image measurement in Metashape, c: RTK measurement. d: Camera locations (white circles) and control point locations (blue circles) on aerial image.

The image orientations and the calibrated relative orientation between camera and lidar were used to calculate 3D-world-coordinates of every lidar point using eq. (3). Figure 11 shows the resulting point cloud generated from 1025 lidar frames at the corresponding image positions.

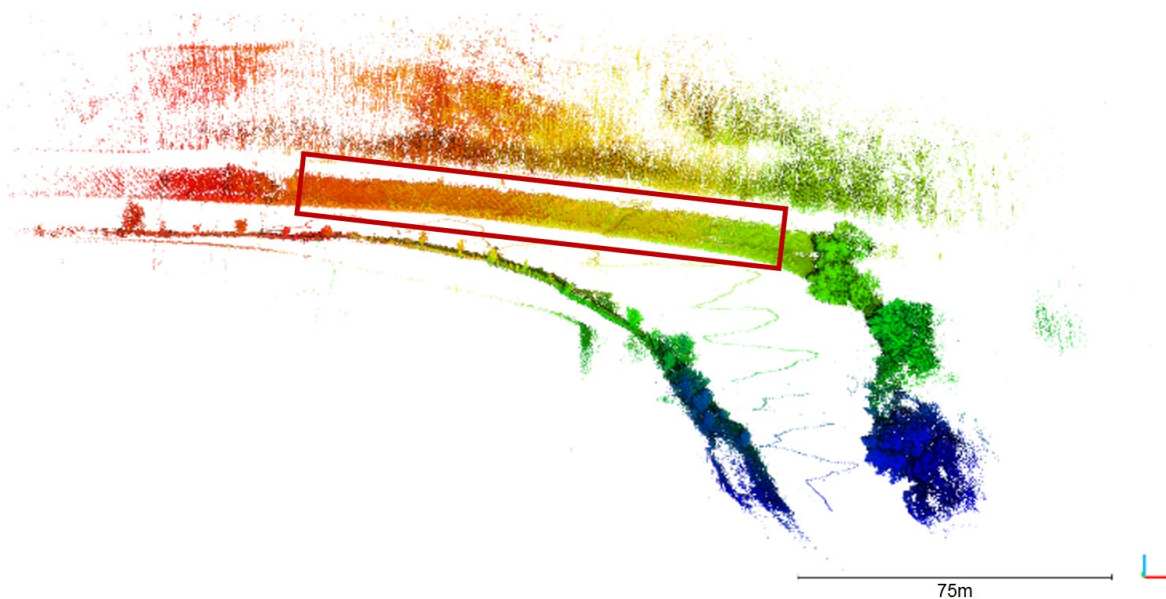


Figure 11: Oriented mobile lidar point cloud. The color indicates the image number that was used for transformation of the lidar frame. The red box shows the area of interest that was used for further analysis.

The outside bank is of specific interest since it is subject of erosion. The area of interest (red box in Figure 11) was clipped from the point cloud and used for further analysis. Due

to the zigzag trajectory, most parts of that area have been measured from more than one UWV position, resulting in a variation of measurement distances. 99% of all points were measured within 60 m distance.

## 6. Accuracy Analysis

The input parameters that were used to generate the resulting 3D point cloud (Figure 11) were determined with a certain accuracy. This leads to a point cloud, which includes a certain error. The following section will treat aspects of error propagation to analyze the expected and achieved accuracy.

### 6.1. Theoretical Accuracy

The acquisition of a 3D point cloud from a mobile lidar operated on an UWV with orientation determination from images involves several error sources, which affect the point cloud accuracy. The main error sources are the orientation of the platform, the time synchronization of lidar and camera, the relative orientation, and the lidar measurement itself. These individual error sources can be combined to an overall expected 3D point uncertainty using the law of error propagation.

#### 6.1.1. Platform Orientation Accuracy

The accuracy of an exterior orientation determination with SfM depends on various factors like overlap of the images, geometry of ray intersections or contrast in the images. Figure 12 highlights that a large portion of the images cannot be used for image matching: The UWV platform is visible in the image, being unsuited for matching. The water body shows reflections and movement and therefore results in mismatches. The sky shows moving clouds that cannot be used for matching either. These areas need to be masked out before calculation, leaving only a small area for matching and orientation determination. Masking has been conducted automatically using a 'Masks From Color' python script for Metashape. Overall, mean standard deviations of 5 mm for position and  $0.004^\circ - 0.078^\circ$  for the orientation parameters have been achieved (see Table 1).



Figure 12: Measurement image used for SfM. Large areas of the image (sky and water) are not suited for matching and therefore masked-out.

#### 6.1.2. Time Synchronization accuracy

The concepts of section 3 assume that the interval between two images is exactly one second. A laboratory experiment was conducted to find the timing stability of the camera clock. An exact time stamp that was gathered by an IMU was therefore displayed on a computer monitor with a frequency of 100 Hz. The camera was placed in front of the monitor and images of the time stamp were captured in time-lapse mode with 1 Hz (Figure 13a). Optical character recognition was applied using the MatLab function 'ocr' to read

the time stamp from each image for a period of approx. 90 minutes. The mean time between two images was 0.999 seconds with a standard deviation  $\Delta t$  of 0.023 s (Figure 13b).

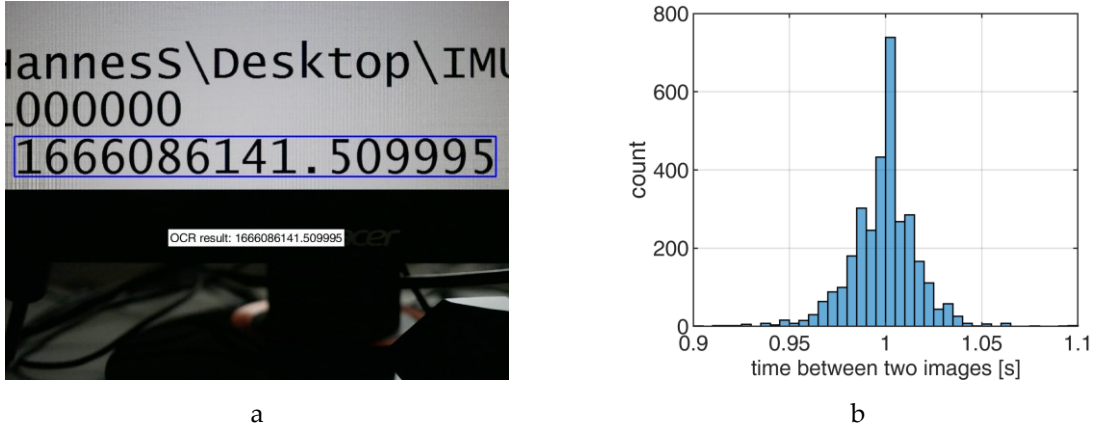


Figure 13: Determination of camera clock offset. a: GPS time stamp on monitor, b: time between two images in time lapse mode with 1 Hz.

The timing error results in wrong assignments between lidar points and camera orientations. Since the UWV is moving, eq. (3) should be extended to

$${}^{wcs} \begin{bmatrix} X \\ Y \\ Z \\ 1 \end{bmatrix} = \left( {}^{wcs} M_{ccsi} + \frac{\delta M_{ccsi}}{\delta t} \cdot \Delta t \right) \cdot {}^{ccs} M_{scs} \cdot {}^{scs} \begin{bmatrix} X \\ Y \\ Z \\ 1 \end{bmatrix} \quad (6)$$

where  $\frac{\delta M_{ccsi}}{\delta t}$  is the speed of the UWV in position and angle and  $\Delta t$  is the time synchronization error. A mean speed of 0.4 m/s (lateral) and 7 °/s (angular) can be assumed (section 6). The resulting error on the object world coordinates is mostly caused by the angular movement of the UWV during  $\Delta t$  and is listed in Table 1.

#### 6.1.3. Calibration accuracy

The relative orientations between image and lidar coordinates can only be determined to a certain accuracy, as shown in section 4. Their standard deviations and influences on the object coordinates are included in Table 1.

#### 6.1.4. Lidar 3D-Point accuracy

The Velodyne Puck user manual (Velodyne, 2019) lists a typical 3D-point accuracy of 3 cm, independent of measurement distance. Kidd (2017) shows that the accuracy in fact decreases with distance and is furthermore dependent on the material of the measured object. Since there is no accuracy analysis available for larger distances, this analysis will assume the manufacturer's declaration. In order to get a standard deviation for all three coordinate components, the 3D error is split into three equal parts:

$${}^{scs} s_{x/y/z} = \sqrt{\frac{({}^{scs} s_{3D})^2}{3}} = 17.3 \text{ mm} \quad (7)$$

#### 6.1.5. Propagation of errors

All individual error sources can be used to calculate an expected measurement 3D-point-error for the mobile lidar point cloud. Each 3D-point is calculated using eq. (6). The expected error on the point cloud coordinates  ${}^{wcs} (X, Y, Z)$  can be estimated using the law of error propagation. Assuming uncorrelated errors, the partial derivatives of eq. (6) with respect to each input variable are calculated and multiplied (squared) with their variance:

$${}^{wcs} s_{X/Y/Z} = \sqrt{\sum \left( \left( \frac{\delta(X/Y/Z)}{\delta v_i} \right)^2 \cdot s_{v_i}^2 \right)} \quad (8)$$

Where  $v_i$  are the 16 input variables:  ${}^{wcs}(\omega, \phi, \kappa, x, y, z)_{ccs}$ ,  $\Delta t$ ,  ${}^{ccs}(\omega, \phi, \kappa, x, y, z)_{scs}$  and  ${}^{scs}(x, y, z)$ . Table 1 lists their standard deviations and estimated influences on the 3D accuracy of the world coordinates for four exemplary measurement distances:

$${}^{wcs}s_{3D} = \sqrt{{}^{wcs}s_x^2 + {}^{wcs}s_y^2 + {}^{wcs}s_z^2} \quad (9)$$

It is assumed, that the three components of  ${}^{scs}(X, Y, Z)$  are equal, which does not reflect the real measurement behaviour of a Velodyne Puck, but simplifies the consideration of the 3D point errors.

The angular errors show, as expected, a higher influence on the overall measurement accuracy, especially in larger distances. The most dominant error source are the time synchronization errors (line 7 in Table 1), also originating from an angular movement of the UWV.

Table 1: Standard deviations ( $s_{v_i}$ ) of input parameters and their effect on the 3D point standard deviation in mm for world coordinates  ${}^{wcs}s_{3D}$  in 5, 10, 25 and 50 m distance.

name	$s_{v_i}$	${}^{wcs}s_{3D}$ (mm)			
		5 m	10 m	25 m	50 m
${}^{wcs}\omega_{ccs}$ (°)	0.078	5.7	11.3	28.0	55.8
${}^{wcs}\phi_{ccs}$ (°)	0.004	0.3	0.6	1.5	2.9
${}^{wcs}\kappa_{ccs}$ (°)	0.078	5.6	11.0	27.4	54.7
${}^{wcs}X_{ccs}$ (mm)	5.1	5.1	5.1	5.1	5.1
${}^{wcs}Y_{ccs}$ (mm)	5.4	5.4	5.4	5.4	5.4
${}^{wcs}Z_{ccs}$ (mm)	5.1	5.1	5.1	5.1	5.1
$\Delta t$ (s)	0.023	21.1	42.5	112	229
${}^{ccs}\omega_{scs}$ (°)	0.067	4.7	9.4	23.4	46.8
${}^{ccs}\phi_{scs}$ (°)	0.035	2.6	5.2	13.0	25.9
${}^{ccs}\kappa_{scs}$ (°)	0.015	1.0	2.1	5.2	10.5
${}^{ccs}X_{scs}$ (mm)	1.0	1.0	1.0	1.0	1.0
${}^{ccs}Y_{scs}$ (mm)	0.4	0.4	0.4	0.4	0.4
${}^{ccs}Z_{scs}$ (mm)	0.2	0.2	0.2	0.2	0.2
${}^{scs}X$ (mm)	17.3	17.3	17.3	17.3	17.3
${}^{scs}Y$ (mm)	17.3	17.3	17.3	17.3	17.3
${}^{scs}Z$ (mm)	17.3	17.3	17.3	17.3	17.3
<b><math>3D_{wcs}</math></b>		<b>39</b>	<b>56</b>	<b>126</b>	<b>250</b>

## 6.2. Experimental Results

The area of interest, the railway embankment, has been used for an accuracy analysis. Therefore, this area was clipped from the oriented mobile lidar point cloud, resulting in a cloud of 218,000 points. This point cloud has been compared to the TLS reference that has 2.5 million points in that area. First, a mesh has been calculated from the reference point cloud, which was then used for a point to mesh distance calculation using CloudCompare. Figure 14 shows the result of that comparison, while Figure 16a shows the histogram of the cloud to mesh distances. Besides a mean difference of 6 cm, an RMSE of 14 cm was achieved. It can be observed, that there is no local accuracy dependency in the point cloud.

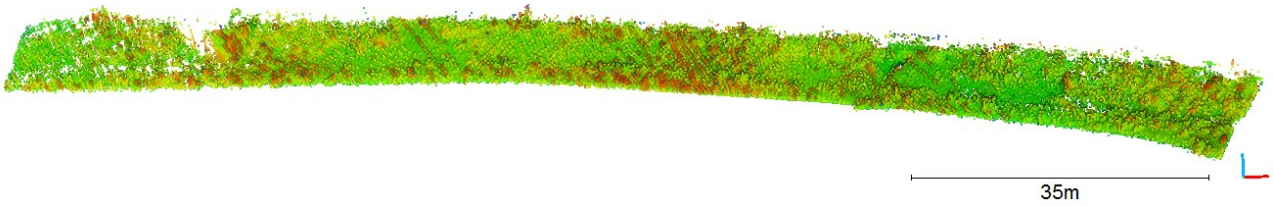


Figure 14: Mobile lidar point cloud to TLS mesh distance

Analyzing cross sections of the Velodyne point cloud reveals that there is a large overall noise resulting from the measurements from different UWV positions and orientations (Figure 15). It highlights furthermore, that the points tend to lie behind the reference. This is also reflected by the decentering of the histogram (Figure 16a).

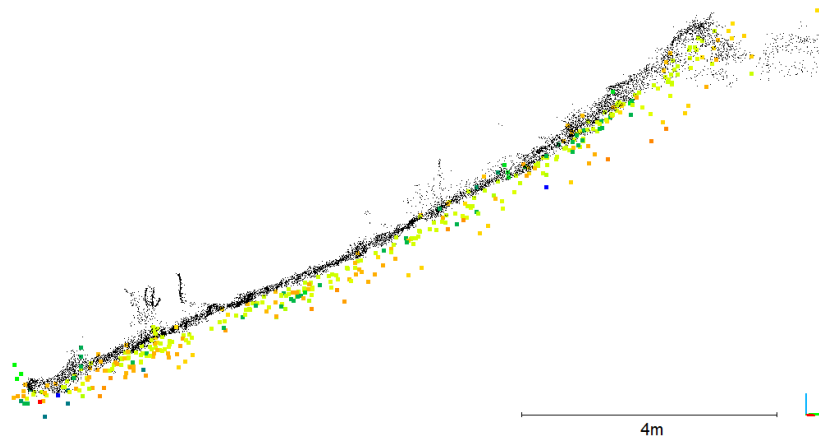
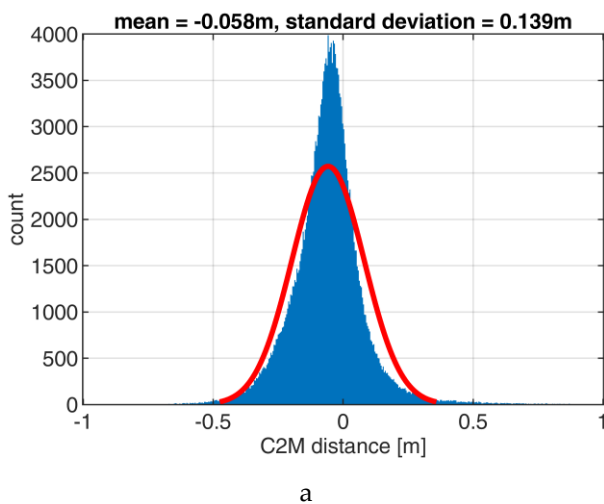


Figure 15: Cross section of mobile lidar point cloud (colored according to UWV position) and TLS point cloud (black).

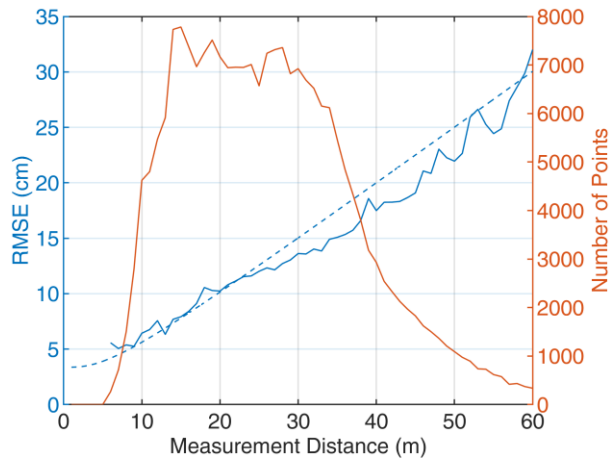
The estimations from section 6.1 suggest that the accuracy depends on the measurement distance. Therefore, distance dependent RMSEs are calculated. The observed point to reference differences are split in 1 m pieces:

$$\{D - 0.5 \text{ m} < d \leq D + 0.5 \text{ m}\} \quad (10)$$

for  $D \in \mathbb{Z}$  along the measurement range. The theoretical standard deviations have been calculated for the same distances following the equations (8) and (9), using the values from Table 1. Figure 16b shows the observed and expected RMSEs.



a



b

Figure 16: Mobile lidar point cloud to TLS mesh distance. a: histogram of cloud to mesh (C2M) distances for area of interest with a normal distribution fitted to the data (red line, parameters in figure title), b: distance dependent theoretical (dashed) vs observed (solid) RMSE and numbers of points in each distance (red).

## 7. Conclusions

This study shows the potential of camera based lidar orientation determination for an uncrewed multisensor water vehicle. GNSS and IMU depict the standard solution for the determination of position and orientation parameters of mobile mapping lidar systems. Differential GNSS offers the advantage of good overall global accuracy. The local accuracy may be improved by an IMU, which also offers a significantly higher temporal resolution. The major drawback of GNSS is signal loss in case of data acquisition in obstructed areas, as well as multi-path effects, which are for instance caused by GNSS signal double reflections on facades or water surfaces. The major drawback of IMU are temporal drifts. The camera-based approach is primarily based on the automatic measurement of tie points in image sequences, thus not requiring a free line-of-sight to satellites – it will also work indoors, provided that there is sufficient texture in the image data for image matching. Sequential relative image orientation will also suffer from drift effects, but here the camera-based approach offers the possibility of controlling drift effects by measuring control points (also called landmarks) in some of the images, thus geo-referencing the orientation data efficiently. Obviously, both methods, GNSS/IMU-based and camera based determination of the position and orientation of a lidar sensor, may also be combined, but the goal of this paper was the analysis of the potential of the camera-based approach. A crucial requirement for the utilization of exterior camera orientations for the lidar points is the calibration of the relative orientation between camera and scanner coordinate systems. The presented strategy enables a fast single-shot calibration, once the calibration field is established. This is more convenient when multiple systems have to be calibrated, compared to existing methods from the literature that use multiple shots of a planar test field. The resulting relative orientation can be determined very accurately with accuracies of  $<1$  mm for the translations and  $<0.1^\circ$  for the rotation angles. The calibration method could be applied for other multisensor systems as well.

The presented lidar transformation method was tested and analyzed based on a specific UWV configuration consisting of a Panasonic consumer camera and a Velodyne lidar. A theoretical accuracy analysis for this system showed that the largest errors occur from uncertainties in temporal synchronization between camera and scanner clocks. Using a camera with external triggering would largely eliminate this error. A practical experiment confirmed the theoretical analyses in terms of RMSE. It even performed superior to the expected RMSE. This could be caused by a bias of the cloud-to-cloud comparison. An inaccurate mobile lidar point is likely to be close to another TLS point, which it will be compared to. Additionally to the RMSE, a systematic offset of 5 cm was observed. This offset could be corrected by a registration of mobile and reference point cloud. Reasons for this behavior might be caused by the different measurement behavior of vegetation by TLS and mobile lidar. Another influence is the inclination of the river bank in combination with the laser footprint. The Velodyne lidar has a laser beam divergence of 3 mrad, resulting in a footprint with a diameter of 9 cm in 30 m distance, which is 10 times the size of the TLS spot. Figure 17 suggests that this results in mixed signals.

While there are some drawbacks in the accuracy of the tested system, it has been shown that the method can be used as a valid positioning option. In a multisensor set-up, it can serve as a fallback option if other positioning systems fail. It can furthermore be used as an approximation, which is needed for other methods like lidar based SLAM methods.

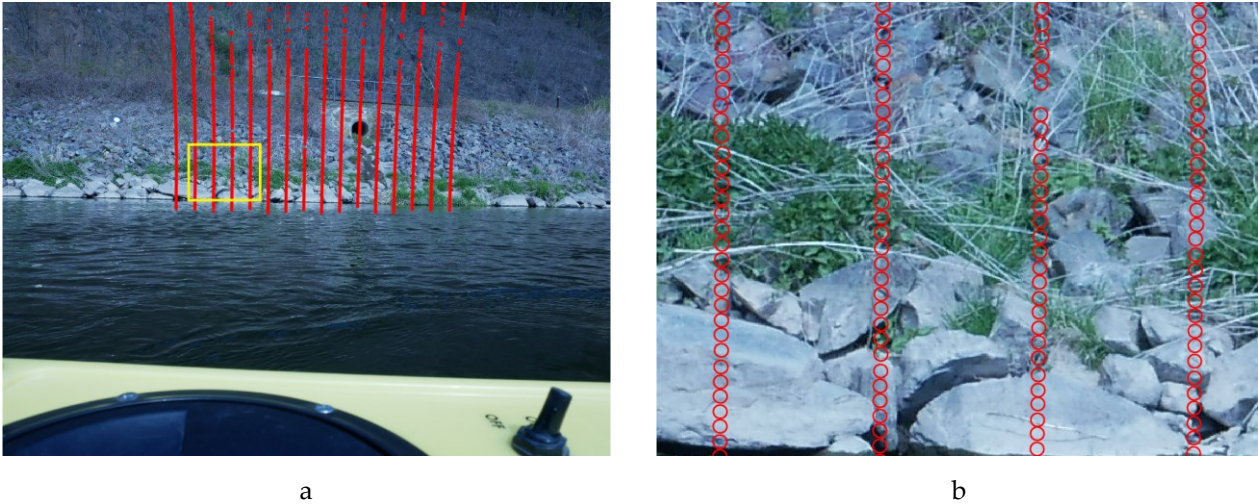


Figure 17: Footprints of mobile lidar. a: scan pattern of one Velodyne frame. b: detail view (yellow box area in a) with measurement distances of approx. 30 m including footprint sizes depicted as circles.

**Author Contributions:** Conceptualization, H.S., R.B. and H.G.M.; methodology, H.S.; software, H.S.; validation, H.S., R.B. and H.G.M.; formal analysis, H.S.; investigation, H.S. and R.B.; resources, H.G.M.; data curation, H.S.; writing—original draft preparation, H.S.; writing—review and editing, R.B. and H.G.M.; visualization, H.S.; supervision, H.G.M.; project administration, H.G.M.; funding acquisition, H.G.M.. All authors have read and agreed to the published version of the manuscript.

**Funding:** This research received no external funding.

**Conflicts of Interest:** The authors declare no conflict of interest

## References

1. Bai, X.; Li, B.; Xu, X.; Xiao, Y. (2022): A review of current research and advances in unmanned surface vehicles. *Journal of Marine Science and Application*, 21(2), pp. 47-58.
2. De Jong, C.D.; Lachapelle, G.; Skone, S.; Elemea, I.A. (2003): *Hydrography*. ISBN 90-407-2359-1.
3. Lewicka, O. et al. (2022): Integration Data Model of the Bathymetric Monitoring System for Shallow Waterbodies Using UAV and USV Platforms. *Remote Sensing* 14, p. 4075.
4. Mandlbürger, G. (2022): A review of active and passive optical methods in hydrography. *The International Hydrographic Review* 28, pp. 8-52.
5. Schneider, D.; Blaskow, R., (2021): Boat-based mobile laser scanning for shoreline monitoring of large lakes, *The International Archives of the Photogrammetry, Remote Sensing and Spatial Information Sciences (ISPRS Archives)*.
6. Zhang, W.; Jiang, F.; Yang, C. F.; Wang, Z. P.; Zhao, T. J. (2021): Research on unmanned surface vehicles environment perception based on the fusion of vision and lidar. *IEEE Access*, 9, 63107-63121.
7. Tauro, F. et al. (2018): Measurements and Observations in the XXI century (MOXXI): innovation and multi-disciplinarity to sense the hydrological cycle. *HYDROLOGICAL SCIENCES JOURNAL*. VOL. 63, NO. 2, pp. 169–196.
8. Cheng, Y.; Jiang, M.; Zhu, J.; Liu, Y. (2021): Are we ready for unmanned surface vehicles in inland waterways? The usv inland multisensor dataset and benchmark. *IEEE Robotics and Automation Letters*, 6(2), pp. 3964-3970.
9. Elhashash, M.; Albanwan, H.; Qin, R. (2022): A Review of Mobile Mapping Systems: From Sensors to Applications. *Sensors* 2022, 22, p. 4262.
10. Nistér, D.; Naroditsky, O.; Bergen, J. (2004): Visual odometry. In *Proceedings of the 2004 IEEE Computer Society Conference on Computer Vision and Pattern Recognition, 2004. CVPR 2004*. Vol. 1, pp. I-I.
11. Macario Barros, A.; Michel, M.; Moline, Y.; Corre, G.; Carrel, F. A Comprehensive Survey of Visual SLAM Algorithms. *Robotics* 2022, 11, 24.
12. Liebold, F.; Maas, H.-G. (2014): Integrated Georeferencing of LiDAR and Camera Data Acquired from a Moving Platform. *ISPRS - International Archives of the Photogrammetry, Remote Sensing and Spatial Information Sciences*. XL-3. Pp. 191-196. 10.5194/isprsarchives-XL-3-191-2014.
13. Ying, X.; Wang, G.; Mei, X.; Yang, S.; Jong, J.; Zha, H. (2014): A direct method for the extrinsic calibration of a camera and a line scan LIDAR, *2014 IEEE International Conference on Mechatronics and Automation*, Tianjin, China, pp. 571-576
14. Kim, E.-s.; Park, S.-Y. Extrinsic Calibration between Camera and LiDAR Sensors by Matching Multiple 3D Planes. *Sensors* 2020, 20, 52.

15. Puszta, Z.; Hajder, L. (2017): Accurate Calibration of LiDAR-Camera Systems Using Ordinary Boxes, *2017 IEEE International Conference on Computer Vision Workshops (ICCVW)*, Venice, Italy, pp. 394-402
16. Sardemann, H.; Eltner, A.; Maas, H.-G. (2018): Acquisition of Geometrical Data of Small Rivers with an Unmanned Water Vehicle. *Int. Arch. Photogramm. Remote Sens. Spatial Inf. Sci. XLII-2*, p. 1023.
17. Sardemann, H.; Mulsow, C.; Maas, H.-G. (2022): Accuracy Analysis of an Oblique Underwater Laser Lightsheet Triangulation System. *PFG - Journal of Photogrammetry, Remote Sensing and Geoinformation Science*. 90, pp. 1-16
18. Mader, D.; Westfeld, P.; Maas, H.-G. (2014): An integrated flexible self-calibration approach for 2D laser scanning range finders applied to the Hokuyo UTM-30LX-EW. *Int. Arch. Photogramm. Remote Sens. Spatial Inf. Sci. XL-5*, p. 385.
19. Velodyne Lidar (2019): VLP-16 User Manual 63-9243 Rev. E.
20. Kidd, J.R. (2017): Performance Evaluation of the Velodyne VLP-16 System for Surface Feature Surveying. Master's Theses and Capstones. 1116. <https://scholars.unh.edu/thesis/1116> (02-12-2022).

**Disclaimer/Publisher's Note:** The statements, opinions and data contained in all publications are solely those of the individual author(s) and contributor(s) and not of MDPI and/or the editor(s). MDPI and/or the editor(s) disclaim responsibility for any injury to people or property resulting from any ideas, methods, instructions or products referred to in the content.



Scientific Paper 3:

## Sardemann et al., 2021: Strict geometric calibration of an underwater laser triangulation system

Hannes Sardemann, Christian Mulsow, Hans-Gerd Maas

### Published in:

The International Archives of the Photogrammetry, Remote Sensing and Spatial Information Sciences, Volume XLIII-B2-2021

<https://doi.org/10.5194/isprs-archives-XLIII-B2-2021-689-2021>

Published on 28 June 2021

### Additional information:

The page numbers have been changed from 689 – 692 to 37 – 40 for this thesis.

This work has been presented in an oral online presentation at the XXIV ISPRS Congress (2021 edition) in Nice.

### Authors' Contributions following CRediT (Contributor Roles Taxonomy):

Conceptualization	Sardemann, Mulsow, Maas
Data Curation	Sardemann
Formal Analysis	Sardemann
Funding Acquisition	Maas
Investigation	Sardemann
Methodology	Sardemann, Mulsow
Project Administration	Maas
Resources	Maas
Software	Sardemann
Supervision	Maas
Validation	Sardemann
Visualization	Sardemann
Writing – original draft	Sardemann
Writing – review & editing	Mulsow, Maas



# STRICT GEOMETRIC CALIBRATION OF AN UNDERWATER LASER TRIANGULATION SYSTEM

H. Sardemann\*, C. Mulsow, H.-G. Maas

Institute of Photogrammetry and Remote Sensing, Technische Universität Dresden, Germany  
(hannes.sardemann, christian.mulsow, hans-gerd.maas)@tu-dresden.de

Commission II, WG II/9

**KEY WORDS:** Triangulation, Laser line, Underwater Photogrammetry, Calibration

## ABSTRACT:

This paper will describe a novel approach for the calibration of an underwater laser triangulation system. Underwater triangulation systems, consisting of a line laser and a camera can be used to determine the geometry of submerged objects or the topography of a water body bottom. Placing camera and laser line projector inside a waterproof housing leads to refraction effects at the air-glass-water interfaces, both of the laser light-sheet and image rays. This implies a deformed laser plane in the water and a curved line on the object surface. The proposed approach strictly models the geometry between camera, laser and housing. First experiments show, that the calibration method can be applied for water depth measurements with accuracies of 0.2 – 0.3 mm at depths in the order of 100 mm.

## 1. STATE OF THE ART

Triangulation based measurement systems, consisting of a line laser and a camera, are commonly used for instance in industrial measurement tasks. By determining the location of the laser line in the image, a height profile along the laser line can be measured, resulting in a 2D measurement system. By adding movement of either the object or the triangulation sensor, 3D measurements can be performed. When used in the air, the laser light-sheet can be calibrated and modelled as a plane. Image measurements along the laser line are intersected with that plane in order to receive an object coordinate.

When laser triangulation is used in underwater environments, there are two main adaptations necessary: First, because of the increasing opaqueness of water for higher wavelengths (Hale and Querry, 1973), a green or blue laser is usually chosen. Furthermore, both the laser plane and the image rays are refracted at the air-housing and housing-water interfaces. Refraction influences have been considered with different approaches in the past. By using two separate housings for the camera and the laser, they can be arranged in a way, that the glass interfaces are planar and parallel to the image plane and perpendicular to the laser plane (e.g. Bleier et al., 2019). In that case, refraction has a radial symmetric distortion effect for the camera image and only results in a decrease of the opening angle for the laser plane. This setup enables the same measurement procedure as it is used in air, where the laser is parameterised as a plane and is intersected with image rays. However, placing camera and laser in different housings limits the compactness of the setup. Placing both the camera and the laser in the same housing, requires them to be oblique to obtain optimal intersection conditions. Palomer et al. (2018) presented a calibration method for a system, where the laser is arranged oblique to the interface. This leads to a curved laser in the water (Figure 1a, c). The authors parameterise the laser sheet as an elliptical cone, which can be intersected with image rays. However, Palomer et al. do not consider that the laser could also be rotated around a second axis, leading to an S-shaped laser sheet (Figure 1b,d). The approach proposed in this paper considers rotation of the laser around all axes.

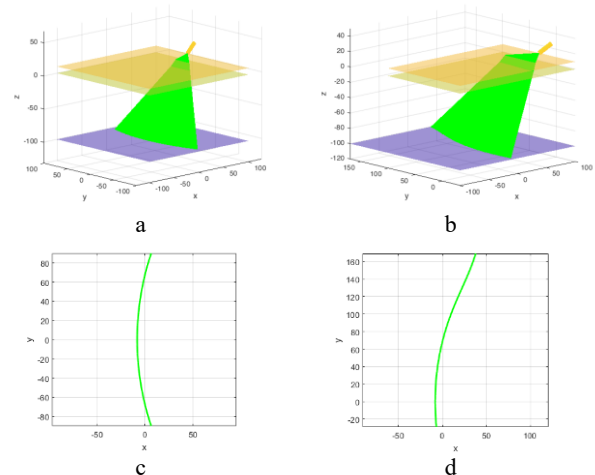


**Figure 1:** Deformation of a laser light-sheet penetrating from air through glass into water (a,b) and their appearance on a planar surface (c, d). Rotated around the y-axis with 45° (a-d) and additionally around the x-axis with 30° (only b, d).

## 2. METHOD

A triangulation system consisting of a line laser and a camera is used for underwater depth measurement. Both components are placed in the same housing with a transparent interface that is immersed into water. The laser light goes through the air, into the glass, from the glass into the water and hits the surface, where it is diffusely reflected. On its way back to the camera, it passes from water to glass to air into the camera. After measuring the laser line in the image (section 2.2), its image ray can be intersected with the deformed laser sheet in object space and a 3D coordinate can be determined (section 2.3).

### 2.1 Set-Up

Laser and image rays should optimally intersect orthogonally on the object in order to minimize the effect of inaccuracies in image

\* Corresponding author

measurements on object coordinates. This is accomplished by tilting laser and camera towards each other. An orthogonal setup of laser and camera in the air results in an angle smaller  $90^\circ$  inside the water, since all rays are refracted towards the normal of the interface. Section 2.5 shows, how minimum and maximum measurable depth can be determined for every set-up. This can be utilized to determine the best set-up, i.e. adjusting the base between the sensors, the orientation of both sensors and the distance to the media interface, for a given depth range. Figure 3 shows an exemplary set-up of camera and laser and the resulting image.

## 2.2 Line Detection

First, the laser has to be detected in the image space. A typical set-up of laser and camera results in a curved line in the image either from top to bottom or from the left to the right side. Therefore, it can be measured row- or column-wise. The intensity of the laser decreases perpendicular to the line and can be described by a Gaussian curve. In reality, the laser shows a strong Speckle overlaying its Gaussian profile, complicating the determination of its peak.

A possible solution for a row- or column-wise detection of the line is to use least-squares-matching (LSM; Ackermann, 1984), with a parameterisation allowing only for scaling and translation in x or y direction. Using LSM enables subpixel accuracy precision. The matching-template consists of one or multiple Gaussian profiles. Its width has to be chosen considering the planarity of the measured surface. A wider patch, consisting of multiple profiles enables a stable measurement when the object surface is planar and the line is rather consistent. A rough surface leads to an uneven line, requiring a smaller patch with down to only one profile, resulting in a less precise determination of the line centre, being highly influenced by Speckle.

Figure 2 shows an example for the detection of a laser line that was projected on a planar surface. Speckle influence can be seen in Figure 2b. LSM was performed with a single-column-patch and a wider patch. The single column is one Gaussian curve (red line in Figure 2c or one column of Figure 2d), while the wide patch consists of 21 of these columns (Figure 2d). The result for a single-column patch is less consistent and precise.

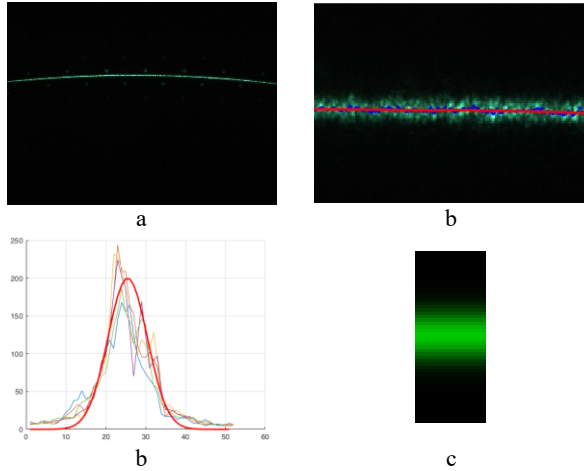


**Figure 2:** Laser line detection with LSM

- (a): Laser Line observed through glass and water
- (b): Detail of (a). Dots show LSM results with single-column patch (blue) and 21-column-wide patch (red)
- (c): green-values of six columns in the centre of (b) (thin lines) and Gaussian profile used as single-column patch (bold red line)
- (d): patch with 21 Gaussian profiles

## 2.3 Depth determination

In order to measure the depth of a point along the laser line observed in the image, its image ray has to be calculated. When interior and exterior orientation of the camera are known, a 3D light ray can be modelled for every image observation. When the position, orientation and thickness of the media interface, i.e. housing, is also known, we can determine the ray path through the interface and determine its vector inside the water, using a 3D representation of Snell's law (a derivation can be found in Glassner, 1989):

$$\vec{v}_2 = \frac{n_1}{n_2} \vec{v}_1 + \left( \frac{n_1}{n_2} (-\vec{N} \cdot \vec{v}_1) - \sqrt{1 + \left( \frac{n_1}{n_2} \right)^2 \left( (-\vec{N} \cdot \vec{v}_1) - 1 \right)^2} \right) \vec{N} \quad (1)$$

where

- $\vec{v}_{\{1,2\}}$  = ray vectors in media 1 and 2
- $n_{\{1,2\}}$  = refraction indices of media 1 and 2
- $\vec{N}$  = normal of interface between the two media

The vector inside the water (red line in Figure 3) needs to be intersected with the laser light-sheet to receive a 3D position. The deformed laser sheet cannot be parameterized as a plane, but it can be described as a bundle of coplanar rays (sub-beams) with a perspective centre at the position of the laser diode. When exterior orientation and opening angle of the laser is known, its sub-beams can be determined and refracted through the glass into the water considering Eq. 1. There is only one sub-beam that intersects with the image ray (magenta line in Figure 3). This sub-beam can be found iteratively by splitting the fan in two halves and choosing the one with the smaller distance between the central sub-beam and the image ray until it is underneath a threshold. The intersection determines the 3D position of the object surface. Figure 3 shows the image ray and its intersection with a specific sub beam of the laser sheet.

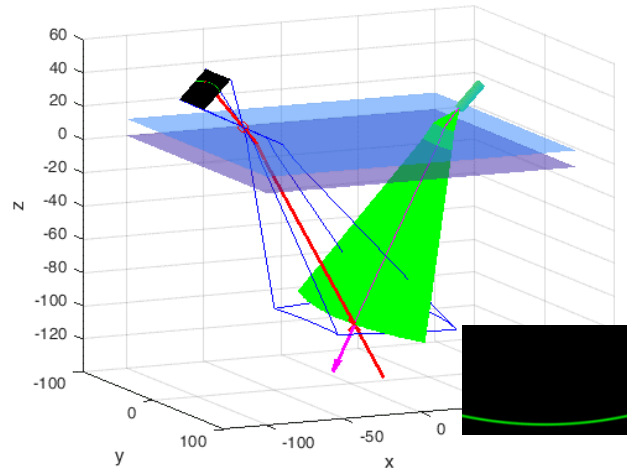


**Figure 3:** Intersection of image ray (red) and sub beam (magenta) of an image measurement on the line (small image). The two planes represent top and bottom of the glass interface between air and water.

## 2.4 Calibration

In order to enable 3D point measurements by intersecting image ray and laser sheet, exterior orientation of both the camera and the laser have to be calibrated relative to each other and relative to the housing interface. By measuring a bundle of sub beams, the laser sheet can be reconstructed. Further, a single sub beam can be determined by measuring at least two beam points.

Practically this can be realised by capturing the projection of the laser sheet in two levels. The definition of a single laser beam can be reached, when constructing the surface nearest to the laser as a grid. Therefore, parts of the laser pass through the first level and hit the second level below. This creates a line pattern on both levels, where the corresponding endpoints span a vector representing a sub beam. A similar approach was used by Mulsow et al. (2006) for the indirect laser triangulation on reflective water surfaces.

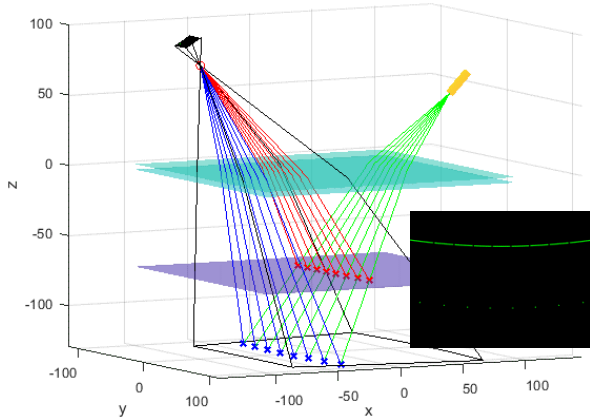


**Figure 4:** Calibration set-up. 3D-scheme and camera image. Sub-beams (green) are measured in two levels (red and blue crosses). The top level (purple plane) is designed as a grid. The image captured by the camera is shown in the small image.

Depending on the number of observed sub beams, camera position and orientation in relation to the glass surface, thickness and orientation of the glass, position and orientation of the two levels and refraction indices of air, glass and water can also be determined in a bundle adjustment using observations of the laser on two levels.

## 2.5 Measurement Volume

From a known or calibrated camera-laser set-up, the maximum achievable measurement volume can be determined. Therefore, the border pixels of the image are intersected with the laser sheet in order to get the outermost object coordinates that can be measured within the image (Figure 5).

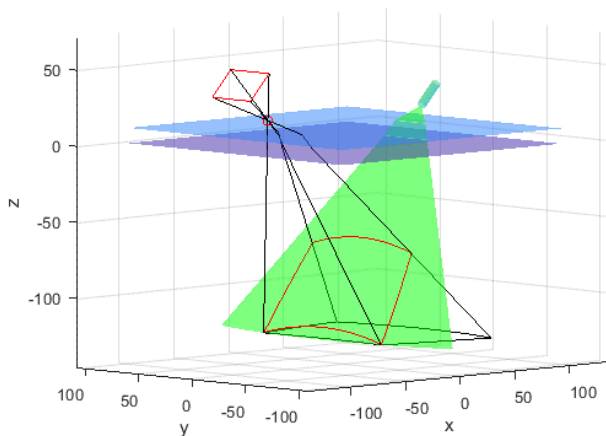


**Figure 5:** Measurement volume of a given camera-laser-set-up.

## 3. EXPERIMENTS AND RESULTS

For validation of the calibration procedure, a triangulation system, consisting of a green laser and an industrial camera has been placed in a glass housing. The laser has an opening angle of  $90^\circ$ , 40mW power and 520nm wavelength. The camera has a 4/3 sensor and a 20 mm lens. The glass housing was immersed into water. Figure 6 shows the experimental set-up

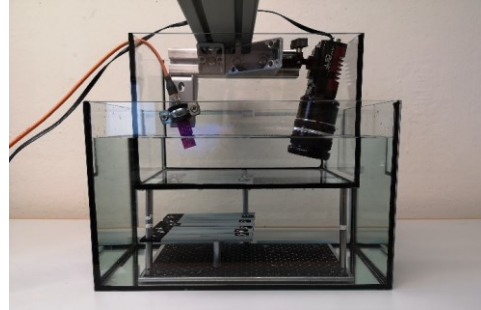


**Figure 6:** Set-up of the experiment, before camera and laser orientation were adjusted.

### 3.1.1 Calibration

For the calibration, two planes were placed in the field of view of camera and laser at 129 and 75 mm depth (Figure 7a). The upper plane is a grid, allowing for parts of the laser line to pass through. The distance of both planes relative to the glass interface and the thickness of the glass were measured with a calliper with 0.05 mm accuracy. Both planes and the interface are assumed planar and parallel. The camera's interior orientation was calibrated in advance by self-calibrating bundle adjustment, using a calibration panel consisting of coded markers and scale-bars. For this experiment, the calibration described in section 2.4 was used to determine the position and orientation of both the camera and the laser relative to the glass interface, keeping all other parameters fixed. The laser line runs from the left to right image side and can be measured column-wise. Eight corresponding points were measured manually in the image on both levels (Figure 7b). Furthermore, 152 points along the line were measured using LSM (section 2.2) and included in the adjustment. The line points are constrained to lay on the according level.

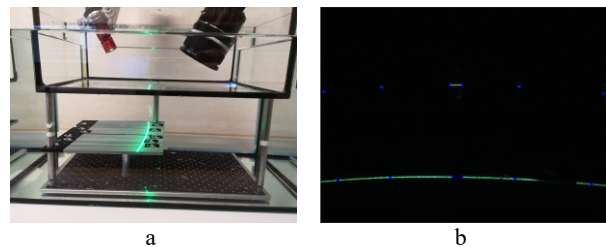


**Figure 7:** Calibration set-up (a) and image (b) with corresponding points on both levels (blue crosses) and additional points across the line (red dots).

Table 1 shows the results of this calibration. The origin of the coordinate system lies on top of the glass interface. The x- and y-position of the laser have been fixed to zero, since only its height relative to the glass plane is relevant. One orientation angle of the laser (around the x-axis) has also been set to zero, since it has the same effect that a wider opening angle would have.

Position of camera and laser were determined with standard deviations of 0.2 - 2 mm, while the orientation angles were determined with standard deviations of  $0.1^\circ$  -  $0.9^\circ$ . This set-up with a 225 mm base and the orientations mentioned in Table 1

enables a depth range of 54 to 185 mm, following the concept of section 2.5.

Laser	value	Std.dev.	Camera	value	Std.dev.
x	0	-	$\Delta x$	220,554	2,334
y	0	-	$\Delta y$	2,730	0,287
z	106,26	0,856	$\Delta z$	-47,378	2,463
$\omega$	0	-	$\Delta\omega$	143,388	0,710
$\varphi$	31,324	0,871	$\Delta\varphi$	33,409	0,911
$\kappa$	0,355	0,069	$\Delta\kappa$	-67,311	0,212

**Table 1:** Calibration Results. Positions are given in mm and orientations as angles in degrees around the x ( $\omega$ ), y ( $\varphi$ ) and z ( $\kappa$ ) axes. Camera position and orientation is given relative to the laser.

### 3.1.2 Measurements

In order to test the achievable accuracy within the depth range, a planar panel was placed in three different water depths from 72 – 122 mm. The panel has circular markers on top of it, enabling a photogrammetric reference measurement. The reference measurement was performed in air, using a DSLR camera and additional coded markers and scale bars, resulting in reference depth values with 0.01 – 0.03 mm standard deviation (Figure 8). Camera and laser were mounted fix to each other and in reference to the glass interface for the calibration and the test depth measurements. The ground plate was 128.9 mm underneath the glass interface. The panel is 6.2 mm thick, resulting in a reference depth of 122.7 mm, when it is placed directly on top of the ground plate. It was placed on two more height levels for this test.



**Figure 8:** Measurement object consisting of ground plate and measurement panel.

Figure 9 shows the camera image for 128.9 mm and 122.7 mm depth, with the laser points that were determined column-wise by LSM. Those image points were intersected with the laser sheet, resulting in 3D object points. It also shows the epipolar lines for both reference depths. The mean distance between the measured points and the reference depths is 0.03 mm with 0.21 mm standard deviation. Figure 10 shows the distance between measurement and reference in object space.

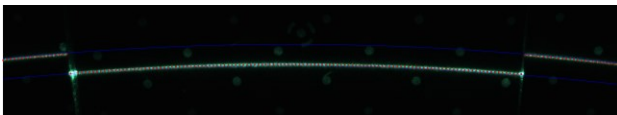


**Figure 9:** Laser line measurement in the image (detail) with LSM-based image measurements (red dots) and epipolar lines of the reference depths (blue lines).

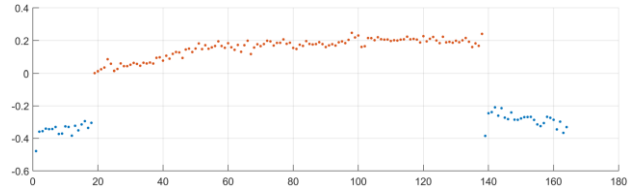


**Figure 10:** Distance between measurement and reference in mm for 128.9 mm (blue) and 122.7 mm depth (red).

The panel was also placed at 72.7 mm and 83.1 mm depths resulting in mean errors of 0.07 and 0.46 mm with standard deviations of 0.15 and 0.34 mm.

## 4. SUMMARY AND OUTLOOK

This paper presents a novel geometric modelling and calibration method for an underwater laser triangulation system. The calibration of the exterior orientations of camera and laser can be achieved with only one image of a calibration object, that consist of two planes, where the top plane is a grid that allows parts of the laser to pass through. First experiments show, that the concept can be applied. Nevertheless, it can be observed, that there are systematic errors left in the results. This can be caused by different influences that will be examined in future work. One possible explanation is the choice of the refraction indices. The exact value for the used glass was unknown. It should be possible to include the refraction index of the glass interface into the adjustment, enough input measurements are available. Another influence was the gridded panel that was used as the top level for calibration. It was not very solid and might have bended, resulting in inaccurate calibration results. A new calibration grid has already been designed and 3D-printed and will be used for upcoming experiments. Another option is to stabilize the calibration by adding a third level to the process.

## ACKNOWLEDGEMENTS

Funded by the Deutsche Forschungsgemeinschaft (DFG, German Research Foundation) – 433522300.

## REFERENCES

- Ackermann, F., 1984: Digital Image Correlation: Performance and Potential Application in Photogrammetry. *Photogrammetric Record*, 11(64), 429-439
- Bleier, M., van der Lucht, J., Nüchter, A., 2019: Towards an Underwater 3D Laser Scanning System for Mobile Mapping. *Proceedings of the IEEE ICRA Workshop on Underwater Robotic Perception (ICRAURP '19)*. Montreal, Canada
- Glassner, A. S., 1989: Surface Physics for Ray Tracing. In *Glassner, Andrew S. (Ed.): An introduction to ray tracing*. Academic Press. 121-160.
- Hale, G. M., Querry, M. R. (1973): Optical Constants of Water in the 200-nm to 200- $\mu$ m Wavelength Region. *Applied Optics*, 12(3), 555.
- Mulsow, C., Schulze, M., Westfeld, P., 2006: An optical triangulation method for height measurements on non-stationary water surfaces. *Int. Arch. Photogramm. Remote Sens. Spatial Inf. Sci.*, Vol. XXXVI, Part 5, 213-217.
- Palomer, A., Ridao, P., Youakim, D., Ribas, D., Forest, J., & Petillot, Y., 2018: 3D laser scanner for underwater manipulation. *Sensors*, 18(4), 1086.

Scientific Paper 4:

# Sardemann et al., 2022: Accuracy Analysis of an Oblique Underwater Laser Lightsheet Triangulation System

Hannes Sardemann, Christian Mulsow, Hans-Gerd Maas

## Published in:

PFG – Journal of Photogrammetry, Remote Sensing and Geoinformation Science 90 – 1

<https://doi.org/10.1007/s41064-022-00196-x>

Published on 22 February 2022

## Additional Information:

The page numbers have been changed from 3 – 18 to 43 – 59 for this thesis.

This work has been awarded with the annual “Hansa Luftbild Prize” for the best and for practical application valuable article in the PFG.

## Authors’ Contributions following CRediT (Contributor Roles Taxonomy):

Conceptualization	Sardemann, Mulsow, Maas
Data Curation	Sardemann
Formal Analysis	Sardemann
Funding Acquisition	Maas
Investigation	Sardemann
Methodology	Sardemann, Mulsow
Project Administration	Maas
Resources	Maas
Software	Sardemann
Supervision	Maas
Validation	Sardemann
Visualization	Sardemann
Writing – original draft	Sardemann
Writing – review & editing	Mulsow, Maas



# Accuracy Analysis of an Oblique Underwater Laser Lightsheet Triangulation System

Hannes Sardemann · Christian Mulsow · Hans-Gerd Maas

Received: 24 October 2021 / Accepted: 9 February 2022 / Published online: 22 February 2022

© The Author(s) 2022

## Abstract

Laser lightsheet triangulation is a well-established optical measurement method, which is frequently used in industrial applications. With some adaptations, the technique can also be used underwater. Placing a green laser line projector and a camera at a fixed base inside a watertight housing enables flexible and accurate underwater measurements at low cost. In order to achieve near-orthogonal intersections on the object surface, camera and laser need to be placed oblique to the housing interface. Refraction influences have to be considered strictly in geometric modelling, with the light propagating through the air-glass and glass-water interfaces. The measurement and calibration methods presented in the paper utilize a concept of splitting the lightsheet into multiple sub-beams, which are traced, refracted, and intersected with image observations in order to receive 3D measurements. In a calibration step, the relative orientation between camera, laser and interfaces is determined. In a theoretical accuracy analysis, the error influences caused by the calibrated parameters is estimated with a standard deviation of 0.2 to 0.4 mm in a depth range of up to 15 cm. A prototype triangulation sensor is applied for practical measurements of two test objects with known geometry. The predicted accuracy is validated in stationary single scan measurements. The sensor is furthermore moved along the test objects, using a six-degrees-of-freedom method to determine its exterior orientation. The combination of multiple single scans results in dense point clouds with 0.3 mm standard deviation compared to a reference.

**Keywords** Triangulation · Laser lightsheet · Underwater Photogrammetry

## Zusammenfassung

Lasertriangulation ist ein etabliertes optisches Messverfahren, welches häufig in industriellen Anwendungen eingesetzt wird. Mit einigen Anpassungen kann die Technologie auch Unterwasser verwendet werden. Mit einem grünen Linienlaser und einer Kamera, die auf einer festen Basis in einem gemeinsamen wasserdichten Gehäuse angebracht werden, werden flexible, genaue und kostengünstige Unterwassermessungen ermöglicht. Um möglichst orthogonale Schnittwinkel auf der Objektoberfläche zu erzielen, müssen die Kamera und der Laser schräg zum Gehäuse angebracht werden. Dies erfordert die geometrische Modellierung der Refraktionen, wenn das Licht an den Trennflächen von Luft zu Glas und von Glas zu Wasser gebrochen wird. Die Mess- und Kalibriermethoden, die in diesem Artikel vorgestellt werden, verwenden ein Konzept, bei dem der gesamte Lichtkegel in einzelne Strahlen unterteilt wird. Diese werden modelliert, gebrochen und mit Bildstrahlen geschnitten um 3D Objektkoordinaten zu erhalten. In der Kalibrierung werden die relativen Orientierungen zwischen Kamera, Laser und Trennflächen bestimmt. In einer theoretischen Genauigkeitsuntersuchung werden die Einflüsse der kalibrierten Parameter auf die Tiefenmessung untersucht und ergeben Standardabweichungen von 0,2 bis 0,4 mm in einem Tiefenmessbereich von bis zu 15 cm. Ein Prototyp wird für praktische Untersuchungen zweier Testobjekte mit bekannter Geometrie verwendet. Dabei werden die theoretisch abgeschätzten Genauigkeiten für Einzelmessungen bestätigt. Der Sensor wird außerdem entlang der Objekte bewegt, während die äußere Orientierung mit dem six-degrees-of-freedom Verfahren bestimmt wird. Die Kombination mehrerer Einzelscans ergibt eine dichte Punktwolke mit einer Standardabweichung von 0,3 mm.

## 1 Introduction

This article presents an oblique underwater laser triangulation sensor system, including its measurement principle and system layout as well as a detailed accuracy analysis. The presented sensor model consists of a laser line projector and a camera, both placed in the same housing, enabling a compact and flexible system design with a fixed base. The target application of this sensor are sub-mm accurate measurements in a close range of up to 25 cm. When mounted on an unmanned water vehicle (UWV), this triangulation sensor enables mapping of the surface of lake and river bottoms in shallow water zones. It is also suitable for measurements in hydromechanical laboratory channels. The system is composed of affordable components, enabling highly accurate underwater measurements at a low cost. It furthermore enables multiple simultaneous measurements along the laser line with a high lateral resolution. It also closes the gap underneath the minimum depth of echo sounders that is typically at least 20 cm. Besides the mapping of rivers and lakes, another application could be the inspection of immersed industrial or archaeological objects, e.g. from an unmanned underwater vehicle, where high accuracies are needed.

In the following sections, the measurement principle of the presented underwater triangulation system will be described. The calibration concept will be outlined and tested for a prototype of the sensor. A theoretical assessment of the error influences of various calibration parameters on the 3D measurement will be presented, and achievable accuracies of the prototype will be practically evaluated by measuring test objects inside a water tank.

## 2 Background and state of the art

Laser lightsheet triangulation is a well-established optical measurement method, frequently used for instance for part inspection in industrial applications. When used in air, usually a red line laser and a camera are mounted convergent on a rigid base. The line laser emits a planar lightsheet that can be modelled as a plane. The object to be measured is placed underneath the triangulation sensor, and the laser line is reflected on the object and projected into the camera image, where it can be detected. When the relative orientation between camera and laser diode is known, object coordinates along the line can be determined by spatial intersection of image rays with the laser plane. In order to optimize depth accuracy and to exploit the camera field of view, camera and laser are tilted towards each other, resulting in preferably near-orthogonal intersection angles. Adding movement to either the triangulation sensor or the object upgrades the triangulation sensor to an optical 3D measurement device.

Applying laser triangulation techniques underwater requires some adaptations. A first major difference is the obvious choice of a suitable laser source, necessitated by the increasing opaqueness of water for higher wavelengths (Hale and Querry, 1973) and the low water penetration depth for the red or near-infrared wavelengths of typical laser triangulation systems. This will usually result in the choice of a green or blue laser source. Furthermore, both the laser diode and the camera need to be placed in watertight housings. This results in refraction influences on the laser plane and the image rays at the air-glass and the glass-water interfaces. When laser and camera are placed in two separate housings, their interfaces can be arranged in a way that refraction influence is minimized. For the laser, that would be a planar interface placed orthogonally to the laser direction. This only leads to a decrease of the lightsheet opening angle. The camera can either be equipped with a spherical dome lens minimizing all refraction effects, or placed behind a planar surface parallel to the image sensor. The planar surface results in radial symmetric distortion effects that can largely be compensated with conventional photogrammetric camera calibration methods (Shortis, 2015).

For the design of a flexible modular underwater laser triangulation system, it may be desirable to have camera and laser source placed in one housing. In this case, camera and laser will necessarily have to be arranged oblique to the interface in order to obtain near-orthogonal intersection angles on the object surface. When the laser lightsheet hits the interface in an oblique angle, it will be deformed, resulting in a curved projection profile. Therefore, strict geometric modelling for precise underwater 3D measurement requires the consideration of aspects of multimedia photogrammetry (with the media air, glass and water), both for the projected laser lightsheet and for the camera. Moreover, several deteriorating effects of measurements through water have to be regarded in system design and in accuracy potential assessment.

While a wide range of industrial in-air laser triangulation systems are commercially available, only a few experimental studies for underwater laser triangulation systems have been presented in the literature. Several authors have presented applications of underwater laser triangulation, but mostly either neglected or simplified aspects of multimedia photogrammetry. Tetlow and Spours (1999) described a laser triangulation system with a rotating mirror, that can be used from a remotely operated vehicle (ROV) to scan underwater work sites and acquire data for CAD models. They focus on aspects of image processing to segment underwater laser stripe images in turbid water, but do not address aspects of multimedia photogrammetry in geometric modelling and only achieve accuracies of a few centimetres. A similar approach, based on a linear array

CCD sensor and a scanning mirror deflecting a laser beam, is shown in (Moore and Jaffe, 2002). Herein, the refractive index is considered in depth calculation, but the curvature of the projected line is avoided by an orthogonal system adjustment, and the basis between linear array sensor and scanned line is arranged across-track rather than in-track (as in conventional laser triangulation system design). Ekkel et al. (2015) present a system for the analysis of the quality of underwater welding. They avoid the geometric modelling of the projected lightsheet by imaging it with a stereo camera, whose measurements are processed using a simplified multimedia approach given by Ross (2014). Roman et al. (2010) used a ROV-mounted 532 nm sheet laser and a camera to create high resolution bathymetric maps of underwater archaeological sites (without considering multimedia photogrammetry aspects) and also reported accuracies at centimetre level. Van der Lucht et al. (2019) developed a triangulation based underwater laser scanning system consisting of a machine vision camera and a green line laser for the 3D acquisition of semi-submerged structures. They show a model to correct for refraction of the laser line and camera rays at the water-air boundary. They proceed from a pointwise model, but then treat the laser lightsheet as a plane for calculation stability reasons. This restricts the laser plane to be orthogonal to the water interface. A similar model has been used by Klopfer et al. (2017) in their study on the potential of the Microsoft Kinect range imager for underwater measurements (with the expected result of a penetration depth limited to 30-40 cm due to the wavelength of the light source). Bleier et al. (2019) present a custom-built system consisting of two rotating line lasers and LED flashes installed on each side of a sensor bar of an underwater mining vehicle, also avoiding the necessity of strict multimedia geometry modelling. Matos et al. (2018) present a method for underwater laser triangulation and conduct an accuracy analysis in a depth range of 150 to 290 mm. They consider refraction for the image rays, but assume a planar laser lightsheet. Palomer et al. (2017) replace the planar lightsheet model by an elliptical cone to approximate the multimedia geometry induced lightsheet deformation in a system for underwater robot arm manipulation (Palomer et al., 2018). The approach requires a rather complex calibration strategy and still delivers remaining errors in the order of about 2 mm.

Several authors also used underwater laser triangulation for environmental monitoring purposes. Gonzales et al. (2007) used a two camera system, where the modelling of the lightsheet is dispensable, in combination with a simplified geometric model assuming the horizontal sensor axis parallel with the water surface, to observe sedimentation processes in a laboratory channel. Røy et al. (2002) developed a lightsheet technology to analyse the relation between surface roughness and three-dimensional

diffusive fluxes of marine sediments at 100  $\mu\text{m}$  resolution. In their case, geometric modelling is less relevant, as only the relative measure of local roughness is determined rather than absolute depth coordinates. Noss et al. (2018) developed a hand-held laser triangulation system with a green laser to measure riverbed topography for micro- and meso-habitat surveys in streams, but don't mention handling of refraction effects. Several other approximate solutions presented in the literature are reviewed in (Inglis et al., 2012).

Meanwhile, there are also commercial underwater laser triangulation systems, for instance the Voyis scanners from seatronics (2020). They provide scanners with different baselines for different depth ranges with accuracies reaching the sub-millimetre range. The scanners are using special underwater laser and camera optical heads to avoid the multimedia photogrammetric modelling mentioned above, which results in rather high system costs. The same holds for the Seavision system from Kraken Robotics (2021), which uses a tricolour laser system in combination with three underwater cameras to produce 3D point clouds with RGB colour attributes. Newton Labs (2020) also offers a range of underwater triangulation scanners with different varying base lengths. A review of active optical underwater 3D scanners present in the literature and commercially available products is presented in (Castillón et al., 2019).

The majority of previous studies assume the laser lightsheet to be planar even underwater. This requires a specific setup of the system where the laser plane is arranged orthogonal to the water interface. When the laser lightsheet hits the interface in an oblique angle, it will be deformed. A rotation of the laser plane around one of the axis of the interface results in a curved lightsheet underwater and therefore in a curved projection line on a planar object surface (**Fig. 1** top, **Fig. 2** left). The curved lightsheet can be parameterised with an elliptical cone, which can then be intersected with the image observations, as shown by Palomer et al. (2018). When the laser plane is furthermore rotated around a second axis, the lightsheet deformation becomes more complex, e.g. S-shaped (**Fig. 1** bottom, **Fig. 2** right).

This paper uses an approach that considers all rotations of the laser and the camera relative to the interfaces. The measurement method is therefore suitable for a variety of underwater triangulation sensor systems where the laser and the camera are placed in the same housing. A strict geometric multimedia modelling enables high precision measurements regardless of the orientation the components. The calibration procedure was already outlined in a more theoretical manner in (Sardemann et al., 2021). For this present article, a system of a green laser line projector and an industrial camera was set up to analyse the applicability of the method both in theory and in practical experiments.

The sensor system was tested in static as well as in scanning mode, where it was moved linearly along a static object.

The remainder of this paper is structured as follows. First, the design of the evaluated sensor system will be presented. This is followed by a description of the utilized methods for measurement and calibration. After a short analysis of the covered measurement volume a theoretical accuracy analysis is presented. It shows the influence of the calibrated input parameters on the error of the measured depth and presents the achievable depth accuracy in three depths along the measurement volume. The estimated accuracy is then validated in four experiments using two test objects. The test objects are first measured with a stationary sensor using only one scanline. Then, they are scanned with a moved sensor system, using an additional camera and the 6-DOF method to determine the position and orientation of each scanline. The multiple scanlines are merged to a dense point cloud of the object. The article closes with a summary and an outlook.

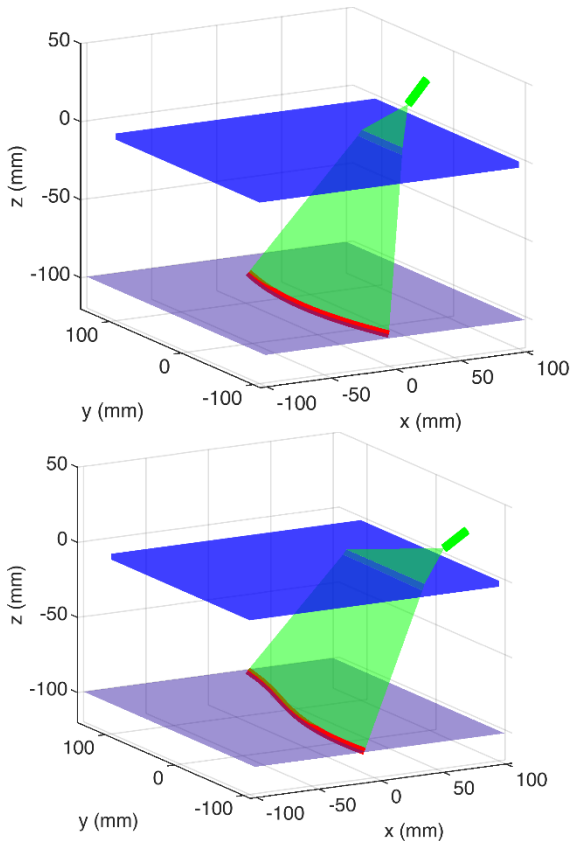


**Fig. 1** Deformation of laser lightsheet at air-glass and glass-water interfaces. Rotated around the y-axis with  $45^\circ$  (top and bottom) and additionally around the x-axis with  $30^\circ$  (bottom).

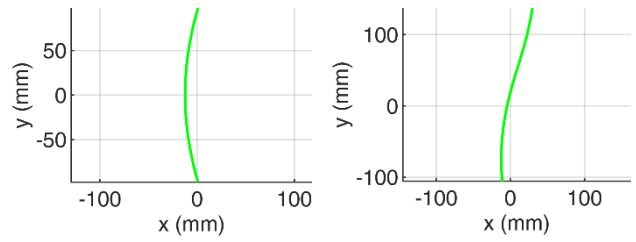


**Fig. 2** Deformed laser line on a planar underwater surface, rotated around the y-axis with  $45^\circ$  (left and right) and additionally around the x-axis with  $30^\circ$  (right).

### 3 System Design

Our underwater triangulation system consists of an industrial camera and a green line laser, both mounted in the same watertight glass housing. The applied camera and laser are a Mako-G419 (Allied Vision, 2021) and a Flexpoint MVmicro (Laser Components, 2020). Having both sensors in the same housing offers the advantage of a compact and flexible modular system design with a fixed base that can be used on unmanned surface or underwater vehicles, where at least the bottom interface of the housing is immersed into water. However, this constrains camera and laser to be oblique to the interface, leading to a challenging task in modelling the spatial intersection of image-ray and laser lightsheet when determining 3D coordinates (section 4).

The goal of the presented system is to enable highly accurate measurements for close range applications in the range of up to 25 cm. Thus, the base between camera and laser was chosen to be approx. 15 cm, tilting both sensors towards the centre, enabling near-orthogonal intersection angles over the depth range. An exact calculation of the covered measurement volume can be found in section 5. Fig. 3 shows the setup, while

Table 1 lists its components and parameters. The ground sampling distance (GSD) for the oblique camera setup depends on measured depth and image position and is given for 100 mm depth at the centre of the image.

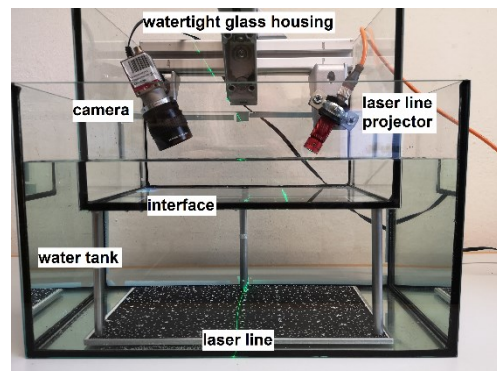


**Fig. 3** System Setup

Table 1 System parameters

component	parameter	value
setup	base	17.4 cm
camera	sensor size	2048 x 2048 Pixels
	pixel size	5.5 x 5.5 $\mu\text{m}$
	focal length	12 mm
	GSD at 100 mm	0.02 x 0.03 mm/Pixel
laser	wavelength	520 nm
	power	40 mW
	line thickness at 100mm	0.03 mm ( $1/e^2$ )
	opening angle	90°

## 4 Measurement method

In order to receive 3D point coordinates of water bottom points, the laser line has to be detected in the image. In theory, the laser brightness decreases perpendicular to line direction in a Gaussian manner. Its peak could therefore be found by fitting a Gaussian curve. In real environments, this is overlaid by a random speckle pattern. Therefore, Least Squares Matching (LSM) with a template consisting of several line profiles is more reliable to determine the centre of the line (section 4.1). The Gaussian intensity profile in line direction may be compensated by using a Powell lens. When the interior and exterior orientations (IOR and EOR) of the camera are known, a corresponding 3D image ray can be calculated for each image point along the line. The image ray can be intersected with sub-beams of the laser lightsheet when the EOR of the laser diode is also known. Herein, refraction at the air-glass and glass-water interfaces must be considered (section 4.2).

The system and its components have to be calibrated. The parameters of interest are the orientation parameters of both the camera and the laser relative to each other and relative to the air-glass and glass-water interfaces (section 4.3). The following paragraphs follow the concepts of Sardemann et al. (2021).

### 4.1 Line measurement

As outlined before, the laser appears as a curved line in the image. Depending on the camera-to-laser setup, it will usually have a preeminent direction either from top to bottom or from left to right in the image. Adapted to that setup, it makes sense to detect the centre of the line either row- or column-wise. From a precision point of view, it would be favourable to use a monochromatic camera with a bandpass filter in the wavelength of the laser. In order to keep this setup suitable for low-cost, a RGB-camera was used, considering only the green channel for line measurement. Using an RGB-camera also delivers the advantage of simultaneous generation of an orthophoto of the water bottom as a by-product. Fig. 4 shows the line in a measurement image, where the line runs from top to bottom and is therefore measured row-wise.

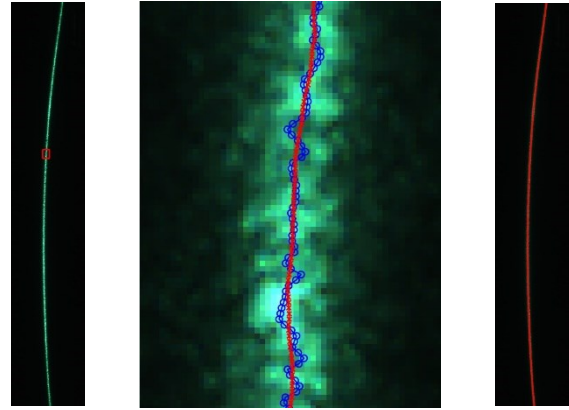


**Fig. 4** Laser line in measurement image (left) with row- (blue) and patch-based (red) detection for detail (centre) and complete line (right). Measurement image has been cut on both sides.

In theory, the intensity of the line decreases in a Gaussian manner perpendicular to the line on the object plane. This suggests conducting a Gaussian fit perpendicular to the line. In a setup where the predominant line direction is vertical, a row-wise fit can be applied to find a first approximation for the centre of the line for every image row. In an iterative process, this may also be used to determine the local direction of the line and conduct a Gaussian fit perpendicular to the line. The result of the row wise fits is depicted as blue circles in Fig. 4 (centre). It can be observed, that the line appearance is overlaid by a strong speckle pattern that influences the fitted peak of the Gaussian curve. Fig. 5 shows three adjacent profiles from that line and the resulting Gaussian fits. The fitted peak varies by three pixels. The standard deviation of the fit-based peak was approx. 0.5 pixels in practical experiments.

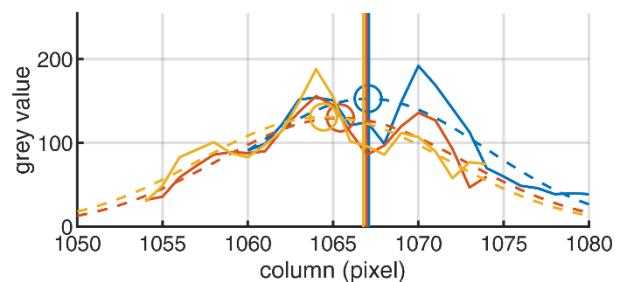


**Fig. 5** Grey-value profiles of three adjacent rows in the green channel in the centre of Fig. 4 (centre) with fitted Gaussian curves (dashed). The circles depict their peaks (1064.44, 1065.42 and 1067.05 pixel). The vertical lines depict the LSM-based results (1066.77, 1066.95 and 1067.10 pixel). Adjacent profiles are indicated with different colours.

Row-wise approaches like the Gaussian fit are strongly influenced by speckle noise, reducing the achievable accuracy. Therefore, a least-squares-matching (LSM) approach is utilized to stabilize the detection of the line centre. Herein, a synthetic patch of multiple Gaussian rows is searched for in every row of the measurement image, enabling only translation in  $y'$  and a horizontal scale factor

out of the standard six affine parameters (**Fig. 6**). The red line in **Fig. 4** and the vertical lines in **Fig. 5** show the LSM-based result, using a 15 x 15 pixel patch. A standard deviation of 0.1 to 0.2 pixels was achieved in practical experiments, depending on depth and surface texture.

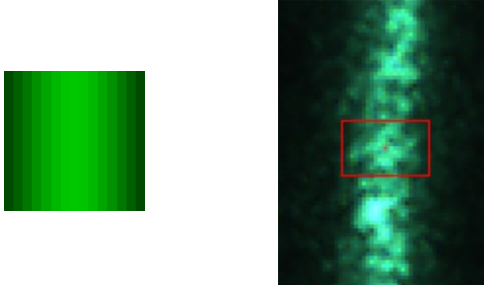


**Fig. 6** LSM: patch (left) and matching result (right).

## 4.2 Determination of 3D coordinates

Each image point along the line can be used to determine a 3D object coordinate. Therefore, its image ray needs to be traced through the air-glass and glass-water interfaces. The refracted vector has to be calculated with a 3D representation of Snell's law (a derivation can be found in Glassner, 1989):

$$\vec{v}_2 = \text{snell}(\vec{v}_1, n_1, n_2, \vec{N}) = \frac{n_1}{n_2} \vec{v}_1 + \left( \frac{n_1}{n_2} (-\vec{N} \cdot \vec{v}_1) - \sqrt{1 + \left( \frac{n_1}{n_2} \right)^2 \left( (-\vec{N} \cdot \vec{v}_1) - 1 \right)^2} \right) \vec{N} \quad (\text{eq. 1})$$

where  $\vec{v}_{\{1,2\}}$  = ray vectors in media 1 and 2  
 $n_{\{1,2\}}$  = refraction indices of media 1 and 2  
 $\vec{N}$  = normal of interface between the two media

First, an image ray  $\vec{v}_{air}^{image}$  in air is calculated from the camera EOR and IOR and the observed image point. Then, eq. 1 is applied at the air-glass interface, giving the direction of the vector. Its position can be determined by intersection of the original ray with the interface. The resulting ray is then refracted a second time at the glass-water interface, resulting in a 3D image vector  $\vec{v}_{water}^{image}$  inside the water (red line in **Fig. 7**):

$$\vec{v}_{glass}^{image} = \text{snell}(\vec{v}_{air}^{image}, n_{air}, n_{glass}, \vec{N}_{glass}) \quad (\text{eq. 2})$$

$$\vec{v}_{water}^{image} = \text{snell}(\vec{v}_{glass}^{image}, n_{glass}, n_{water}, \vec{N}_{water}) \quad (\text{eq. 3})$$

The image ray needs to be intersected with the laser lightsheet to receive a 3D coordinate. Since the deformed lightsheet cannot be parameterized overall, it is split into sub-beams that are considered as separate rays  $\vec{v}_{air}^{subbeam}$  and can be calculated using the exterior orientation of the laser diode. The sub-beams are refracted individually using eq. 2 and eq. 3. Each refracted image ray intersects only with one specific sub-beam of the laser lightsheet. This sub-beam can be found recursively by splitting the lightsheet in two halves

until the nearest points of the skew image- and laser rays is underneath a given threshold. The resulting sub-beam  $\vec{v}_{water}^{subbeam}$  is depicted in magenta in **Fig. 7**. The measured object point is the intersection of sub-beam and image ray in water:

$$P_{object} = \vec{v}_{water}^{subbeam} \cap \vec{v}_{water}^{image} \quad (\text{eq. 4})$$

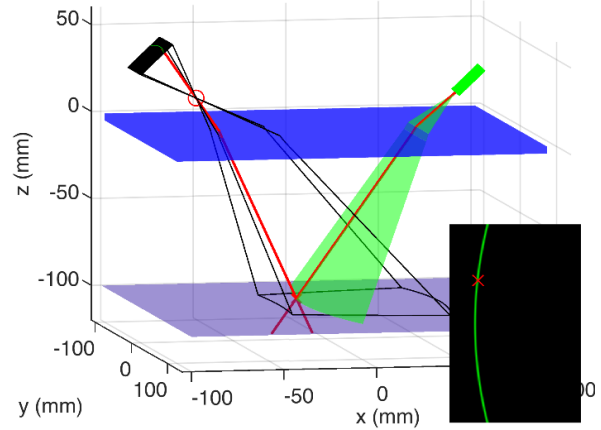


**Fig. 7** Determination of 3D coordinate by intersection of image point (red x in small image) with laser lightsheet.

### 4.2.1 Exterior orientation determination for scanning

As shown in the previous section, a scan of a curved line can be measured from a single image. In order to receive a 3D point cloud, either the object or the triangulation sensor has to be moved. The presented triangulation sensor is developed with the objective of its application on UWV for scanning water body surfaces. Therefore, the sensor is designed to be moved, and multiple line scans can be merged to a point cloud based on the known or measured movement of the sensor relative to the object. This may be achieved by different approaches:

- For outdoor applications on an UWV, an on board GNSS and/or inertial measurement system would be a typical choice (Sardemann et al., 2018). However, with accuracies of approx.  $0.1^\circ$  (low cost IMU orientation) and up to 2 cm (RTK-position), this may deteriorate the achieved sub-mm accuracies of each line scan.
- On an underwater vehicle, GNSS is not available. A common method here is to use acoustic signals for positioning. Maurelli et al. (2021) present a review of various active and passive underwater localisation techniques.
- The images captured by the RGB camera of the triangulation sensor can be used to detect features on the water body bottom in consecutive images and use those for a strip triangulation. The image data may furthermore be used to generate a colour orthophoto of the water bottom (Bodenmann et al., 2016). The laser line area in

the image could either be excluded from that process, or a second image with different exposure settings and inactive laser could be captured at every position.

- The geometry of the ground can also be utilized for a SLAM based method. Massot-Campos et al. (2016) generate local 3D models from laser line triangulation and use those for the orientation determination of following measurements in an iterative process.
- In laboratory applications, the triangulation sensor can be operated on a fixed rail construction, with the position measured by linear encoders.
- A more flexible, yet accurate solution for close range applications is a six-degrees-of-freedom (6-DOF) procedure as described below.

6-DOF has been chosen for the accuracy analysis experiments shown in section 7. A calibrated, non-planar panel with markers is solidly attached to the sensor system, and its object coordinates are determined relative to the triangulation sensor. An additional camera is placed statically on a tripod to record the moving panel. For each image of the static camera, a spatial resection is calculated, providing the EOR of the static camera in the coordinate system of the moving panel. Transforming the apparent camera motion parameters into panel motion enables the calculation of the position and orientation of the panel for each shot. The known relative orientation between panel and triangulation sensor system gives the position of the triangulation sensor in a coordinate system centred in the static camera. A detailed description of the mathematical model and the accuracy potential of 6DOF can be found in Luhmann (2009). **Fig. 8** shows the result for three example images.

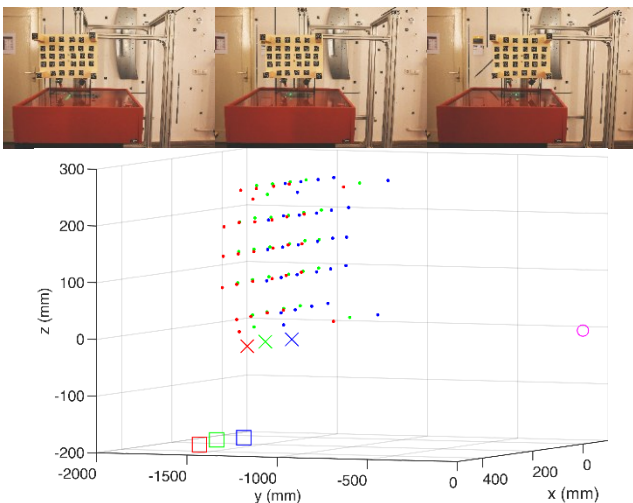


**Fig. 8** 6-DOF determination. The stationary camera is marked with a magenta circle. Panel (dots), triangulation camera (x) and laser (square) coordinates are given in 6-DOF camera coordinates for three images in red, green and blue (from left to right)

### 4.3 Calibration

For the determination of 3D coordinates using eq. 4, it is necessary to know the IOR and EOR of the camera and the EOR of the laser relative to the interfaces. These parameters have to be determined in a suitable calibration procedure. The calibration procedure used here utilises a concept presented by Sardemann et al. (2021), which was inspired by a concept presented by Mulsow et al. (2006) for a laser lightsheet based water surface measurement technique. The basic concept is to make a number of sub-beams of the laser lightsheet distinguishable and to trace these rays. From the intersection of multiple sub-beams, the position and orientation of the laser diode can be determined. Sub-beams are distinguished using a calibration pattern that consists of two planar levels and is placed inside the water underneath the triangulation sensor (**Fig. 9** left). The top level is gridded, leading to a line with small gaps where the light passes to the bottom level. On the bottom level, only small parts of the line appear. Two lines can be observed on the measurement image. One is almost continuous but interrupted and the other one is only fractional (**Fig. 9** bottom right). The gaps of the top level line (red) represent corresponding sub-beams to the pieces on the bottom level (blue). The two lines can be measured with LSM (section 4.1) and serve as observations for a bundle adjustment.

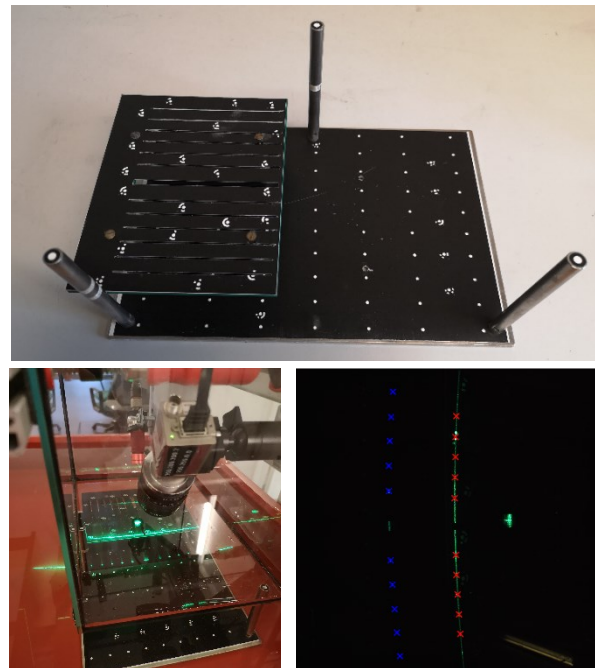


**Fig. 9** Calibration pattern (top), setup (bottom left) and image (bottom right) with observations on top (red) and bottom (blue) level.

From the image observations, 3D coordinates can be calculated using approximate values for camera, laser and interface orientations (chapter 4.2). The parameters are then adjusted iteratively until all sub-beams intersect at the laser diode centre with a minimum distance. A condition to the

adjustment is that the object coordinates of the two lines fall on the two calibration levels. Depending on the number of observations, it is theoretically possible to calibrate camera, laser and interface EORs, as well as refraction indices of the three media. However, due to correlations between parameters, only the laser EOR was calibrated in the adjustment, while the camera IOR and EOR parameters were determined separately before water and housing were added, using the markers on the calibration pattern and additional scale bars. The resulting calibrated set up is shown in Fig. 10.

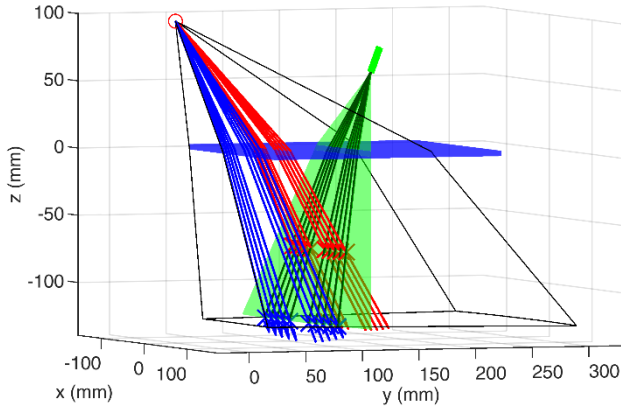


**Fig. 10** Calibration result: Refracted image rays intersect with refracted sub-beams (dark green) on top level (red) and bottom level (blue).

## 5 Measurement volume

Knowing the parameters of the calibrated system, the measurement volume can be calculated. For every pixel position of the measurement image, an unambiguous object coordinate can be calculated using the formulae of section 4.2. Thus, a look-up-table (LUT) can be calculated, giving the X-, Y- and Z-coordinates for every pixel. Fig. 11 shows the three components of that LUT. The image area on the right side of the 0 mm line in Z is only of theoretical interest, since this corresponds to an intersection of image ray and laser lightsheet above the glass surface. There are also image areas where the laser plane is never seen (dark blue in Fig. 11). For these image areas, no 3D coordinate can be determined. It can be observed that lines of same depth appear as curved lines in the image (black isolines in Fig. 11 (Z) and coloured lines in Fig. 12).

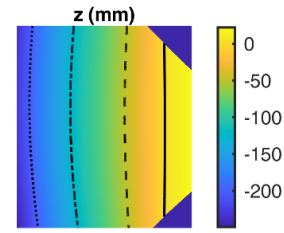
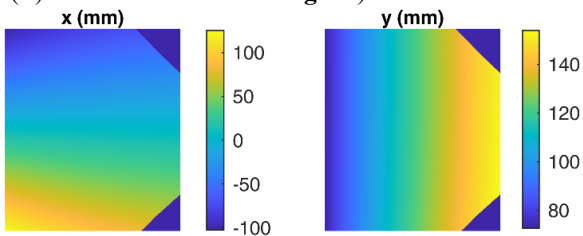


**Fig. 11** Look-Up-Tables giving the corresponding x-, y- and z-coordinates for every pixel. In Z, isolines for the reference depths of 0, 50, 125 and 250 mm (from right to left) are shown.

By calculating the 3D object coordinates for the image borders, the maximum possible measurement volume (3D bounding box) can be calculated. In the setup shown here, the maximum depth is 248 mm. The width of the measurement volume is 227 mm in X and 81 mm in Y. Fig. 12 shows the measurement volume and the position of the three reference depths, corresponding to the dashed and dotted lines in Fig. 11.

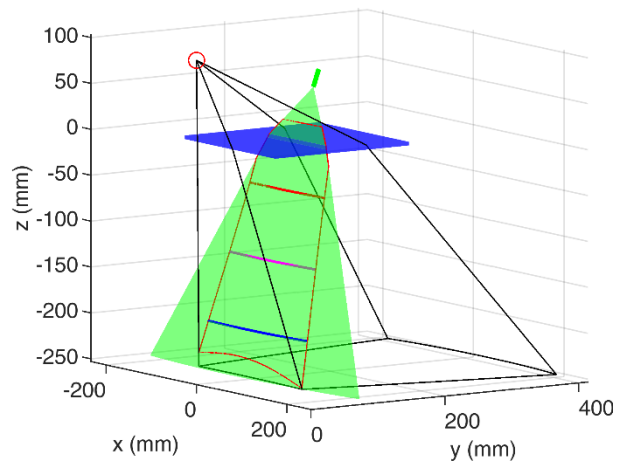


**Fig. 12** Measurement volume: The thin red line depicts the maximum measurement volume. The bold lines represent object coordinates for the depths of 50 mm (red), 125 mm (magenta) and 250 mm (blue).

## 6 Statistical Accuracy Analysis

The accuracy of 3D coordinates with a calibrated underwater triangulation system is effected by various parameters section 4.2). These include the image measurement of the laser line, IOR and EOR of the camera and EOR of the laser diode. These parameters can only be determined with a certain accuracy and thus contribute to the error budget of 3D measurement. The influence of each parameter on the X-, Y- and Z-coordinate depends on its precision, the system setup and the location of the measured laser in the image. The overall error can be assessed by the law of error propagation. Herein, the influence of each parameter of eq. 1 to the resulting 3D position can be estimated by calculating the derivative of the equation with respect to that parameter and scale it with its standard deviation. The following paragraphs address the resulting standard deviation of 3D coordinates measured across the whole image using the previously calibrated triangulation system. Since the sensor

will mostly be used for depth determination, the evaluations will focus on the Z-coordinate. The errors are exemplarily shown for the three reference depths of 50 mm, 125 mm and 200 mm.

The following analyses only consider the accuracy in a profile scan obtained from a single image, neglecting the additional errors caused by system movement determination when merging multiple profiles.

### 6.1 Influence of image measurement

In the presented setup, the preeminent direction of the laser line is horizontal in the image. The line centre is therefore measured row-wise in the image. LSM and Gauss-fitting methods lead to sub-pixel accuracies in  $x'$  in the order of 0.1 – 0.2 pixel. Therefore, the influence of an assumed standard deviation of 0.15 pixel is tested. **Fig. 13a** shows that the resulting error in Z increases with depth with a maximum standard deviation of 0.027 mm in Z at 200 mm depth.

### 6.2 Influence of camera IOR

The camera used for triangulation was calibrated beforehand, and its IOR was considered stable for all measurements. The most prominent influence of the camera IOR on the triangulation measurement is the focal length. It has been calibrated with a standard deviation of 0.004 mm. This results in a depth error of up to 0.06 mm over the whole measurement volume, depending on the depth (**Fig. 13b**).

### 6.3 Influence of camera EOR

The camera position and orientation relative to the interface were determined in a bundle adjustment using a calibration pattern (section 4.3). A standard deviation of about 0.05 mm in position and  $0.02^\circ$  for orientation was achieved herein. The glass interface is considered as the XY-plane of the coordinate system. Therefore, only the Z-coordinate of the camera relative to this plane is considered. X and Y have no influence and are set to zero. A standard deviation of 0.05 mm for the cameras Z-coordinate results in standard deviations of up to 0.08 mm for depth determination (**Fig. 13c**). The orientation errors result in up to 0.04 mm ( $\omega$  and  $\varphi$ ) and up to 0.015 mm ( $\kappa$ ).

### 6.4 Influence of laser EOR

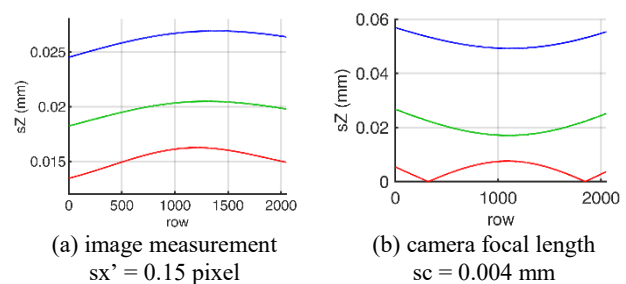
The laser position and orientation were calibrated as shown in section 4.3. The position was determined with standard deviations of 0.07 mm (X), 0.08 mm (Y) and 0.12 m (Z). This results in depth standard deviations of up to 0.035 mm, 0.15 mm and 0.12 mm, respectively (**Fig. 13d**). The orientation was determined with standard deviations of  $0.02^\circ$  ( $\omega$ ),  $0.06^\circ$  ( $\varphi$ ) and  $0.04^\circ$  ( $\kappa$ ) resulting in up to 0.12 mm (**Fig. 13e**).

### 6.5 Influence of refractive index

The refractive index of water  $n_w$  has been taken from the literature. Its value depends among other factors on the temperature of the water, which was not stable amongst all experiments. When a variation of  $10^\circ$  is assumed,  $n_w$  has an inaccuracy of approx. 0.001 (Schiebener et al., 1980). This results in a depth standard deviation of up to 0.17 mm (**Fig. 13f**).

### 6.6 Summarized estimation of accuracies

The previous paragraphs show, that the measurement accuracy is dependent on various inputs and their standard deviations. All influences contribute to the total error budget with individual errors of up to 0.18 mm. A decrease of accuracy with increasing depth can be observed for all parameters. Unfortunately, image measurement accuracy also decreases with depth (and thus decreasing line width). Rotations of camera and laser around the Y- and Z-axis ( $\varphi$  and  $\kappa$ ) have minimum effects close to the centre of the image, where the rotation axis is. All error sources can be summarized (squared) to a total estimation of the error budget using the law of error propagation. Herein, correlations between all parameters are neglected, as the parameters have been determined in independent processes that do not provide the required information. Assuming the previously mentioned standard deviations leads to the depth accuracies shown in **Fig. 13g**. Standard deviations of 0.15 mm to 0.35 mm can be expected in the whole measurement volume under perfect conditions. They increase with depth and decrease towards the image centre. The accuracy of the line measurement affects the depth measurement linearly. It is therefore an important factor especially considering relative depth deviations. The determination of absolute 3D measurements is furthermore effected by the quality of the system calibration. Thus, a proper balance between the two components should be achieved. The refractive index of water also has a significant influence on the measurement. In laboratory experiments, it could be determined with high precision in a multimedia bundle adjustment (Mulsow, 2010). Instabilities in the mount of camera, laser and housing may lead to higher standard deviations.



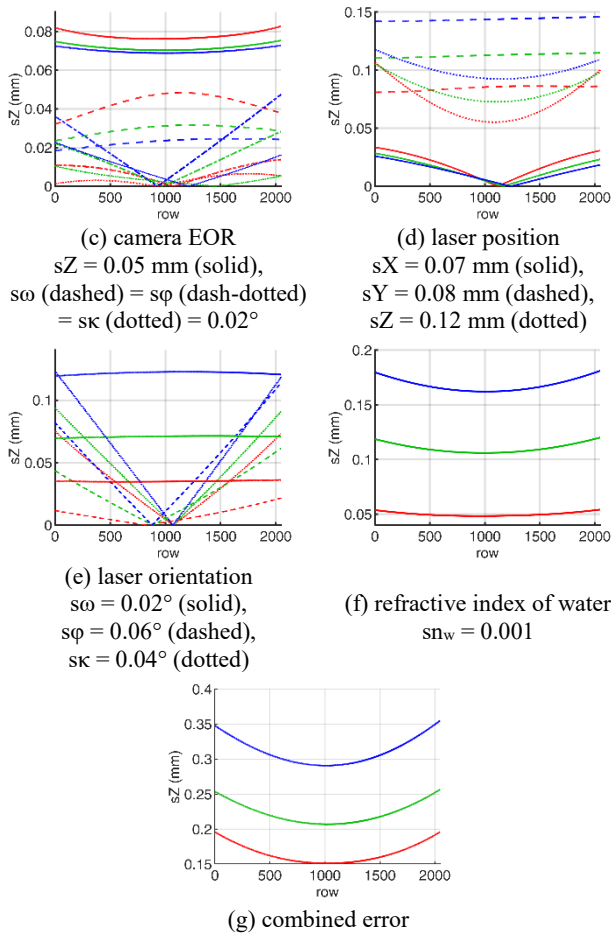


**Fig. 13** Variance propagation. Influence of various parameters on depth standard deviation in three reference depths of 50 mm (red), 125 mm (green) and 200 mm (blue)

## 7 Experiments and de facto achieved accuracies

In addition to the theoretical accuracy potential analysis in the previous section, the previously calibrated underwater laser triangulation sensor prototype was used for practical testing in a water tank. Experiments were conducted in two setups. First, it was used with a single shot, measuring along the laser line profile. This measurement can be compared to the theoretically assessed accuracies of section 6. Secondly, the sensor system was moved along two test objects to investigate the accuracy in scanning mode. In those experiments, 6-DOF was used for EOR determination (section 4.2.1). This second setup is lastly more relevant for the applicability on an unmanned water or underwater vehicle.

### 7.1 Reference objects

Two objects were used for testing. The first is a very stable metal test object (**Fig. 14** top) with dimensions of approx. 300 mm (length) x 65 mm (width) x 45 mm (height), containing three height levels. For reference measurement,

markers have been attached to the object. The markers have been measured in a close range bundle adjustment, using calibrated scale bars and a DSLR camera and the Aicon 3D Studio software. Plane fits of the three levels give the heights of 0.006 mm, 20.195 mm and 40.135 mm with RMSs of 0.070 mm, 0.028 mm and 0.004 mm (**Fig. 14** bottom).

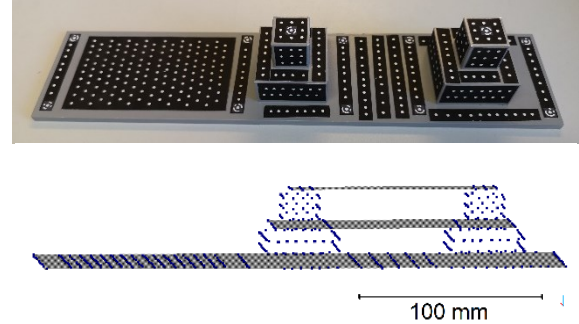


**Fig. 14** Test object. Image (top) and 3D point cloud with plane fits (bottom).

The second object is an aquarium decoration shipwreck model. It is made out of plastic and has dimensions of approx. 260 mm (length) x 75 mm (width) x 80 mm (height). It was placed lying on one side (**Fig. 15** left). The geometry of this object is more complicated, including holes and rough surfaces. The reference measurement was conducted with a GOM ATOS triple scan triangulation scanner (GOM, 2021). The resulting mesh has a resolution of approx. 0.1 mm and accuracies in the order of 0.02 mm (**Fig. 15** right).

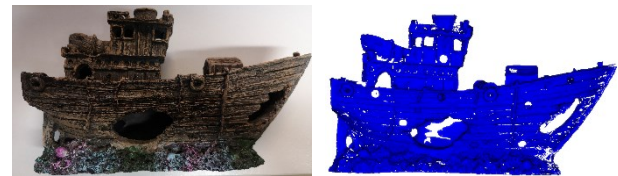


**Fig. 15** Wreck model. Image (left) and 3D mesh (right).

### 7.2 Single profile scan

The two test objects were placed in water underneath the sensor system and measured with a single image resulting a single profile scan. **Fig. 18** shows the measurement image and the detected laser line. For a better comprehension of the situation, a brighter version of the measurement image was also included (**Fig. 18** a).

**Fig. 19** shows the calculated 3D coordinates and the differences to the reference heights. Especially the test object with markers produces outliers in the image measurement, which affect the object coordinates. After a simple threshold-based outlier exclusion, the majority of points (99%) are within  $\pm 3\sigma$  (2.24 mm). A bi-modal behaviour can be observed in the histogram (**Fig. 19** d left). This is mainly caused by the different surface colours of the test object. The white markers are overexposed, while the

black areas appear very dark in the image. The overexposure is furthermore mainly in the direction of the laser, leading to an intensity dependent image measurement. **Fig. 16** highlights that the measured line centre tends to the left in the white areas. This effect may be eliminated by using a more evenly coloured object (as it is usually the case for water bottoms), by a correction method based on intensity or line width or by using multiple images with different exposure settings.

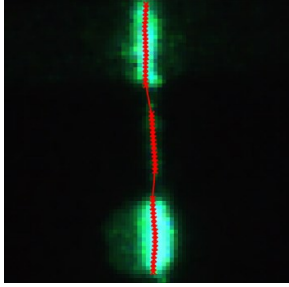


**Fig. 16** Detail of image measurement of test object with white markers on black background.

The wreck model has a surface texture with less contrast leading to normal-distributed of image measurement errors and thus also of object coordinate distances to the reference mesh (**Fig. 19 d right**). It is also not infected by outliers and shows a standard deviation of 0.38 mm. However, the distances to the test object are strongly influenced by the registration of scanline and reference mesh, leading to a decentred histogram.

**Fig. 19 (c)** includes the estimated standard deviations following the calculations of section 6, showing that the experimentally observed reference-measurement distances are well comparable to the theoretically calculated standard deviation.

**Table 2** summarises the results of the single scan mode.

**Table 2** Results of single image scan.

	Test object with markers	Wreck model
Points on object	1461	1105
Standard deviation	0.75 mm	0.38 mm
Outlier threshold	$3\sigma = 2.24$ mm	$3\sigma = 1.15$ mm
Points remaining	1448 = 99%	1105 = 100%
Standard deviation after outlier removal	0.22 mm	0.38 mm

### 7.3 Scanning mode

The two objects were also measured in a scanning procedure. For that purpose, the triangulation sensor was moved linearly in steps of approx. 2-5 mm. For each step, a measurement image of the laser line was recorded and the

corresponding 3D scan profile was calculated. Furthermore, an orientation image was captured with an additional camera on a tripod for every step in order to calculate the EOR of each shot using the 6-DOF approach as outlined in section 4.2.1. The 6-DOF camera was placed approx. 1.5 m away from the panel and provided EOR values for the triangulation sensor with approx.  $0.01^\circ$  and 0.05 mm standard deviations over all experiments. The measurement setup is depicted in **Fig. 17**.

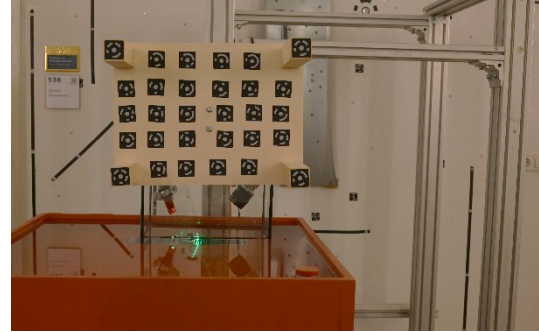


**Fig. 17** Setup for scanning mode.

The first test object was scanned with seven lines (**Fig. 20 a left**). Planes were fitted in the three height levels with an RMS of approx. 0.2 mm per plane. **Fig. 20 (c left)** and **(d left)** show the distances of the object points to the fitted planes. Large distances can be observed, where the laser has hit a white marker. The histogram shows the same bi-modal as in section 7.2, resulting from the different influences of white and black surface colours of the test object. The standard deviation of all points is 0.3 mm. After an exclusion of outliers with distances greater than  $+3\sigma$  (0.9 mm), a standard deviation of 0.20 mm can be observed.

The wreck model was scanned with 70 scan positions. The point cloud resulting from the single scans referenced by 6-DOF is shown in **Fig. 20 (a right)**. An iterative-closest-points algorithm was used to align the underwater triangulation point cloud with the reference mesh (**Fig. 20 b right**). The distances between triangulated point cloud and reference mesh have a standard deviation of 0.4 mm. **Fig. 20 (c – d right)** show the point to mesh distances after an exclusion of outliers greater than  $3\sigma$  (1.2 mm). The outlier-free distances show a normal distribution with a standard deviation of 0.29 mm. This includes both the errors of single scan triangulation and EOR determination of the moving sensor. Systematic errors occur at positions, where the reference mesh shows holes, that originate from markers, which were needed for the reference scan. Furthermore, it can be observed, that some complete lines show higher distances. This might be caused by an inaccurate 6DOF determination. The 6-DOF determination has a larger influence on the accuracy using the complex wreck model than with the plane based test object, where only the measured depth is compared to the three planes ignoring the

lateral location. **Table 3** summarises the results for the measurement of both test objects in scanning mode.

**Table 3** Results for test object with markers in scanning mode

	Test object with markers	Wreck model
Number of scanlines	7	70
Total points on object	4,656	66,666
Standard deviation	0.3 mm	0.4 mm
Outlier threshold	$3\sigma = 0.9$ mm	$3\sigma = 1.2$ mm
Points remaining	4587 = 98%	65,987 = 99%
Standard deviation after outlier removal	0.20 mm	0.29 mm

## 8 Summary and Outlook

In this article, an oblique underwater laser lightsheet triangulation sensor concept was presented and evaluated. The system concept with camera and laser placed in one housing allows for a compact and flexible design, but requires the development of a dedicated geometric model for 3D coordinate determination and system calibration. The presented prototype triangulation sensor consisting of an industrial camera and a green line laser with 17.5 cm base is designed to measure depths of up to 25 cm. Theoretical error analyses showed that accuracies of 0.2 to 0.4 mm can be achieved with such a sensor system. Practical experiments confirmed these theoretical estimations. When used in scanning mode, additional errors may occur from the positioning of each line scan. The achieved accuracy is suitable for various applications.

The sensor will be integrated into a multisensory UWV (unattended water vehicle, Sardemann et al. (2018)) to conduct in situ measurements of riverbeds in shallow areas. Future work will also consider an adaptation of the LSM-based line measurement to varying water bottom brightness as well as an extension of the concept from a single laser line to multiple lines obtained with a diffractive element in the laser optics. Future work should also include investigations on the most suitable method for the determination of position and orientation of the sensor in outdoor experiments, since the 6DOF method that was used in this article is limited at larger distances or underwater.

## 9 Declaration

**Funding:** Funded by the Deutsche Forschungsgemeinschaft (DFG, German Research Foundation) – 433522300.

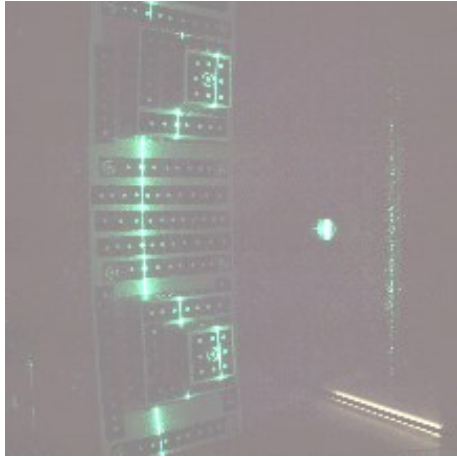
## References

Ackermann, F., 1984: Digital Image Correlation: Performance and Potential Application in Photogrammetry. *Photogrammetric Record*, 11(64), 429-439

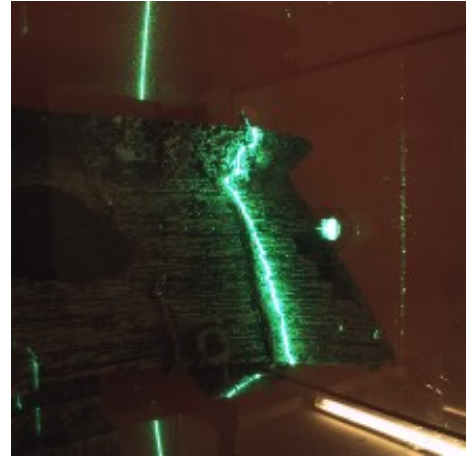
- Allied Vision, 2021: GigE Vision Cameras. Mako. Technical Manual. [https://cdn.alliedvision.com/fileadmin/content/documents/products/cameras/Mako/techman/Mako\\_TechMan\\_en.pdf](https://cdn.alliedvision.com/fileadmin/content/documents/products/cameras/Mako/techman/Mako_TechMan_en.pdf)
- Bleier, M., van der Lucht, J., Nüchter, A., 2019: Towards an Underwater 3D Laser Scanning System for Mobile Mapping. *Proceedings of the IEEE ICRA Workshop on Underwater Robotic Perception (ICRAURP '19)*. Montreal, Canada
- Bodenmann, A.; Thornton, B.; Ura, T. Generation of High-resolution Three-dimensional Reconstructions of the Seafloor in Color using a Single Camera and Structured Light. *J. Field Robot.* 2017, 34, 833–851.
- Castillón, M.; Palomer, A.; Forest, J.; Ridao, P. (2019): State of the Art of Underwater Active Optical 3D Scanners. In: *Sensors* 19 (23). 5161
- Ekkel, T.; Schmik, J.; Luhmann, Th.; Hastedt, H., 2015: Precise laser-based optical 3D measurement of welding seams under water. *Int. Arch. Photogramm. Remote Sens. Spat. Inf. Sci.*, Vol. XL-5/W5. 117–122
- Glassner, A. S., 1989: Surface Physics for Ray Tracing. In Glassner, Andrew S. (Ed.): *An introduction to ray tracing*. Academic Press. 121-160.
- GOM, 2021: Industrial 3D Scanning Technology. <https://www.gom.com/en/products/3d-scanning>
- Gonzalez, E.; Sanchez-Tembleque Diaz-Pache, F.; Mosquera, L.; Agudo, J., 2007: Bidimensional measurement of an underwater sediment surface using a 3D-Scanner. *Optics & Laser Technology*, Vol. 39. 481–489
- Hale, G. M., Querry, M. R. (1973): Optical Constants of Water in the 200-nm to 200- $\mu$ m Wavelength Region. *Applied Optics*, 12(3), 555. <https://doi.org/10.1364/ao.12.000555>
- Inglis, G.; Smart, C.; Vaughn, I., 2012: A pipeline for structured light bathymetric mapping. *IEEE/RSJ International Conference on Intelligent Robots and Systems, Vilamoura, Portugal*
- Klopper, F.; Hämmerle, M.; Höfle, B., 2017: Assessing the potential of a low-cost 3-D sensor in shallow-water bathymetry. *IEEE Geoscience and Remote Sensing Letters* 14. 1388-1392
- Kraken, 2021: SeaVision Precision Underwater Imaging. [https://krakenrobotics.com/themencode-pdf-viewer/?file=https://krakenrobotics.com/wp-content/uploads/2020/11/SeaVision-2020\\_rev-1.1.pdf](https://krakenrobotics.com/themencode-pdf-viewer/?file=https://krakenrobotics.com/wp-content/uploads/2020/11/SeaVision-2020_rev-1.1.pdf)
- Massot-Campos, M.; Oliver, G.; Bodenmann, A.; Thornton, B., 2016: Submap bathymetric SLAM using structured light in underwater environments. In *Proceedings of the 2016 IEEE/OES Autonomous Underwater Vehicles 2016 (AUV 2016)*, Tokyo, Japan, 6–9 November 2016. 181–188.
- Matos, G.; Buschinelli, P.; Pinto, T., 2020: Underwater Laser Triangulation Sensor Model With Flat Refractive Interfaces. *IEEE Journal of Oceanic Engineering*, Vol. 45, No. 3, 937-945
- Maurelli, F.; Krupiński, S.; Xiang, X.; Petillot, Y., 2021: AUV localisation: a review of passive and active techniques. *International Journal of Intelligent Robotics and Applications*.
- Moore, K.; Jaffe, J., 2002: Time-evolution of high-resolution topographic measurements of the sea floor using a 3-d laser line scan mapping system. *Journal of Oceanic Engineering* 27. 525–545
- Mulsow, C., Schulze, M., Westfeld, P., 2006: An optical triangulation method for height measurements on non-stationary water surfaces. *Int. Arch. Photogramm. Remote Sens. Spatial Inf. Sci.*, XXXVI, Part 5, 213
- Mulsow, C., 2010: A Flexible Multi-media Bundle Approach. *International Archives of Photogrammetry, Remote Sensing and Spatial Information Sciences*, XXXVIII, Part 5.

- Newton Labs, 2020: Underwater Laser Scanners. [https://www.newtonlabs.com/subsea\\_scanners-1.htm](https://www.newtonlabs.com/subsea_scanners-1.htm)
- Noss, C.; Wilkinson, J.; Lorke, A., 2018: Triangulation hand-held laser-scanning (TriHaLaS) for micro- and meso-habitat surveys in streams. *Earth Surf. Process. Landforms*, Vol. 43/6. 1241-1251
- Laser Components, 2020: Flexpoint Machine Vision Lasers MVmicro series. [https://www.lasercomponents.com/fileadmin/user\\_upload/home/Datasheets/laser-modules/mv\\_micro.pdf](https://www.lasercomponents.com/fileadmin/user_upload/home/Datasheets/laser-modules/mv_micro.pdf)
- Luhmann, T., 2009: Precision potential of photogrammetric 6DOF pose estimation with a single camera. *ISPRS Journal of Photogrammetry and Remote Sensing* 64, 275-284.
- Palomer, A.; Ridao, P.; Ribas, D.; Forest, J., 2017: Underwater 3D laser scanners: The deformation of the plane. *Sensing and Control for Autonomous Vehicles* (Eds. T. Fossen, K. Petter-sen, H. Nijmeijer), Springer. 73-88
- Palomer, A., Ridao, P., Youakim, D., Ribas, D., Forest, J., & Petillot, Y., 2018: 3D laser scanner for underwater manipulation. *Sensors*, 18(4), 1086.
- Roman, C.; Inglis, G.; Rutter, J., 2010: Application of structured light imaging for high resolution mapping of underwater archaeological sites. *IEEE OCEANS, Sydney*. 1–9
- Ross, B., 2014: COSC 3P98 – Ray Tracing Basics. Brock University, St. Catharines, Canada ([www.cosc.brocku.ca/Offerings/3P98/course/assignments/RayTracing.pdf](http://www.cosc.brocku.ca/Offerings/3P98/course/assignments/RayTracing.pdf)). 17-19
- Røy, H.; Hüttel, M.; Jørgensen, B., 2002: The role of small-scale sediment topography for oxy-gen flux across the diffusive boundary layer. *Limnol. Oceanogr.*, Vol. 47(3). 837–847
- Sardemann, H.; Eltner, A.; Maas, H.-G., 2018: Acquisition of Geometrical Data of Small Rivers with an Unmanned Water Vehicle. *Int. Arch. Photogramm. Remote Sens. Spatial Inf. Sci.* XLII-2, 1023
- Sardemann, H.; Mulsow, C. & Maas, H.-G., 2021: Strict geometric Calibration of an Underwater Laser Triangulation System. *Int. Arch. Photogramm. Remote Sens. Spatial Inf. Sci.*, XLIII-B2-2021, 689
- Schiebener, P.; Straub, J.; Levelt Sengers, J. M. H.; Gallagher, J. S. 1990: Refractive index of water and steam as function of wavelength, temperature and density. *Journal of physical and chemical reference data*, 19(3), 677-717.
- Seatronics, 2020: Voyis. Insight Underwater Laser Scanners. [https://seatronics-group.com/wp-content/uploads/2020/04/Voyis\\_LaserScanners\\_DataSheet.pdf](https://seatronics-group.com/wp-content/uploads/2020/04/Voyis_LaserScanners_DataSheet.pdf)
- Shortis, M., 2015: Calibration Techniques for Accurate Measurements by Underwater Camera Systems. *Sensors* 2015, 15, 30810-30827.
- Tetlow, S.; Spours, J., 1999: Three-dimensional measurement of underwater work sites using structured laser light. *Measurement Science and Technology*, Volume 10, Number 12. 1162-1167
- van der Lucht, J.; Bleier, M.; Leutert, F.; Schilling, K., and Nüchter, A., 2018: Structured-Light Based 3d Laser Scanning of Semi-Submerged Structures. *ISPRS Ann. Photogramm. Remote Sens. Spatial Inf. Sci.*, Vol. IV-2. 287-294

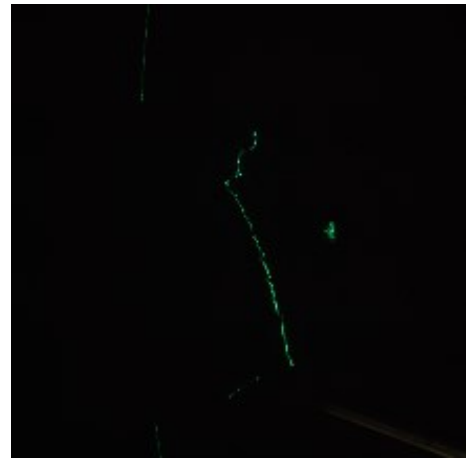
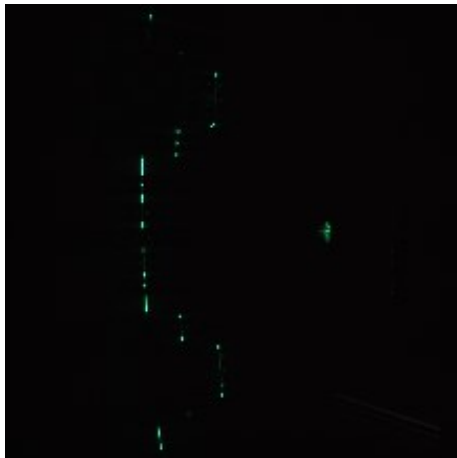
Test object with markers



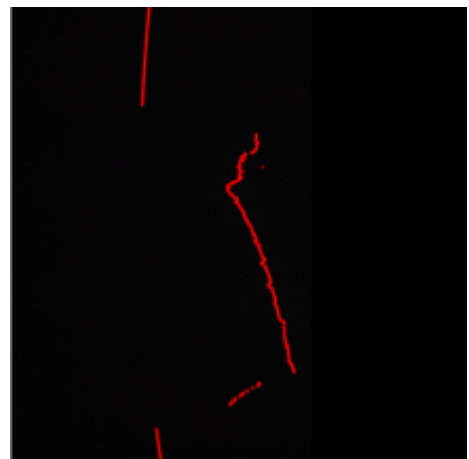
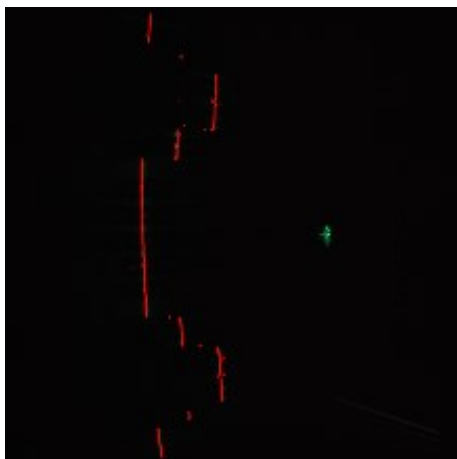
Wreck model



a  
measurement image  
with enhanced  
brightness (left) and  
long exposure (right)

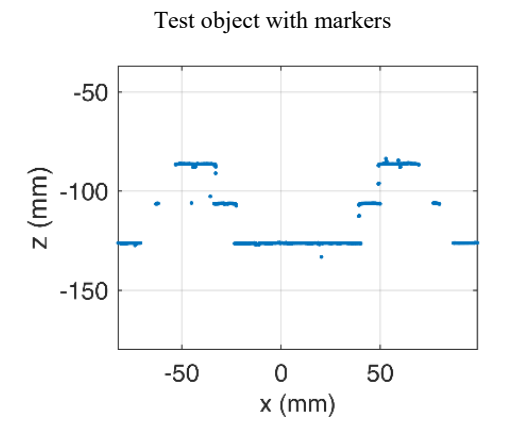


b  
measurement image

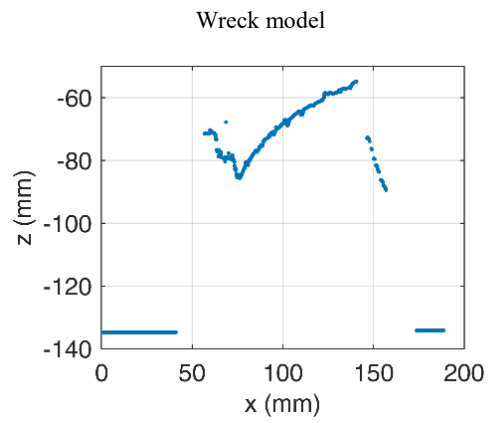


c  
detected laser line

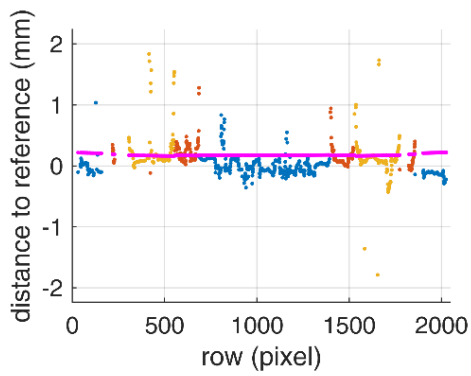
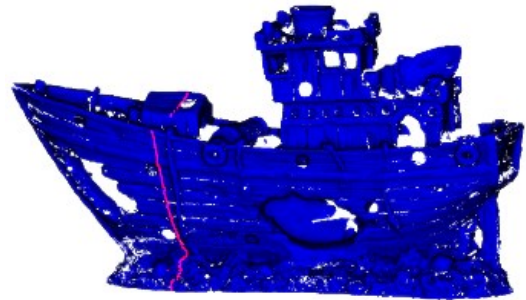
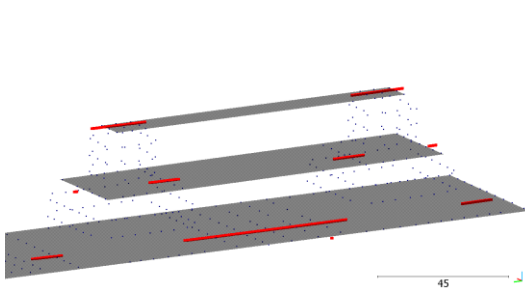
Fig. 18 Measurement images of a single profile scan of test object with markers and wreck model.



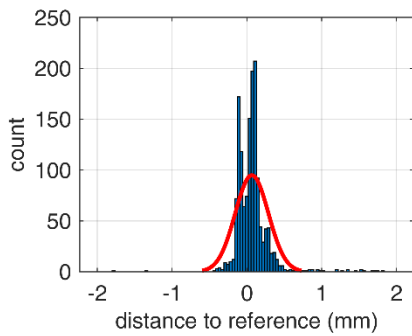
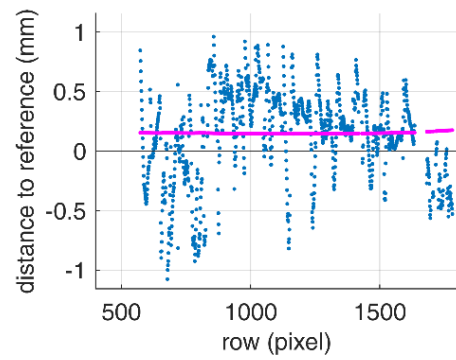
a  
reconstructed  
object points  
(scanline)



b  
scanline on  
reference point  
cloud (left) and  
mesh (right)



c  
row-wise  
distances to  
reference planes  
(left) and mesh  
(right) with  
theoretical  
standard  
deviation  
(magenta)



d  
histogram of  
distances to  
reference

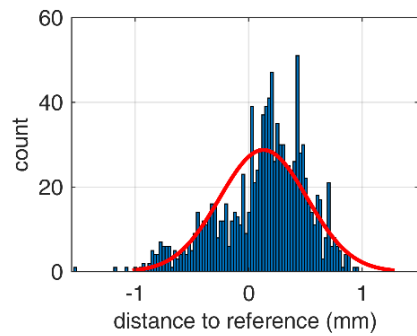
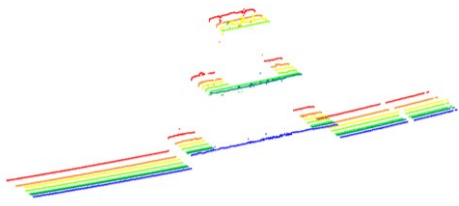


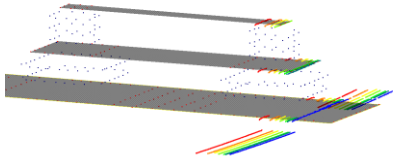
**Fig. 19** Results of a single profile scan of test object with markers and wreck model. Object points are outlier adjusted with  $\pm 3\sigma$ .

Test object with markers

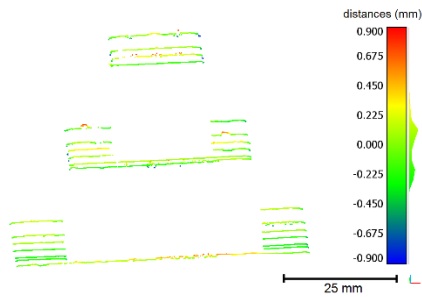
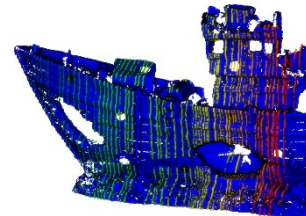
Wreck model



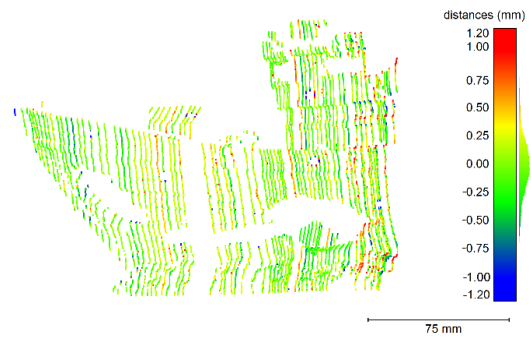
a  
point cloud.  
Colour depicts  
scanline number



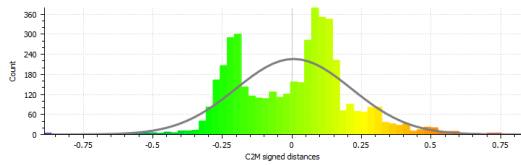
b  
point cloud  
aligned on  
reference cloud  
(left) and mesh  
(right)



c  
distances to  
reference planes /  
mesh



Gauss: mean = 0.005542 / std.dev. = 0.204266 [68 classes]



d  
histogram of  
distances to  
reference

Gauss: mean = 0.004230 / std.dev. = 0.294063 [255 classes]

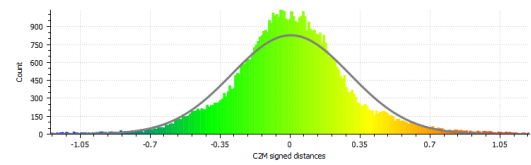


**Fig. 20** Scanning mode results of wreck model (70 scanlines) and test object with markers (seven scanlines). Outliers  $>3\sigma$  were excluded beforehand.

## 3 Syntheses

The following sections describe comparisons and syntheses of the concepts presented in the previous chapters. In section 3.1, a comparison of the platform orientation methods used for the registration of mobile point clouds is made. Therefore, the INS-based method (Sardemann et al., 2018) is compared to the image-based method (Sardemann et al., 2023). Then, in section 3.2, the techniques of measuring above the water level (Sardemann et al., 2018 and 2023) and under water (Sardemann et al, 2022 and 2023) are merged in a combined UWV concept.

### 3.1 Comparison of INS- and Camera-based Orientation

In Sardemann et al. (2018), IMU orientations and GNSS positions were used for the generation of a 3D point cloud from mobile lidar points, while in Sardemann et al. (2023), exterior camera orientations were utilised. The first version did not use RTK GNSS and simplified the boresight alignment between scanner and IMU to integer multiples of  $90^\circ$ . The following section will analyse a mobile lidar point cloud, generated from IMU orientations and RTK positions, using a strict lever arm and boresight alignment calibration. A theoretical error estimation will be examined with de facto achieved accuracies from a comparison with a TLS-based reference. This is done with data acquired during the measurement presented in Sardemann et al. (2023), enabling a direct comparison of INS- and image-based approaches.

#### 3.1.1 Boresight alignment and lever-arm calibration

The calibration of the relative orientation and the base between the IMU coordinate system ( $ics$ ) and the scanner coordinate system ( $scs$ ) is achieved using the calibration field presented in Sardemann et al. (2023). Since the Velodyne points, the RTK positions and the IMU orientations are all synchronised with GPS time, stationary UWV positions are not needed for the calibration. In fact, they would even be counter-productive, since the IMU tends to drift when standing still. Therefore, only calibration measurements recorded with a moving platform are used. The dynamic calibration procedure described in section 4.2 and 5.2 in Sardemann et al. (2023) was used for that purpose. Every lidar point recorded during the dynamic process has an exact GPS time stamp. The IMU and RTK trajectories are interpolated in order to get a platform position and orientation for all of those time stamps and therefore for every lidar point. A first mobile lidar point cloud of the calibration field is generated, using an approximated relative transformation between  $scs$  and  $ics$ :

$${}^{wcs} \begin{bmatrix} x \\ y \\ z \\ 1 \end{bmatrix}_i = {}^{wcs} M_{ics} \cdot {}^{ics} M_{scs} \cdot {}^{scs} \begin{bmatrix} x \\ y \\ z \\ 1 \end{bmatrix}_i$$

where  ${}^{wcs} M_{ics}$  represents the RTK-position and IMU-orientation of the platform in the world coordinate system ( $wcs$ ) and  ${}^{ics} M_{scs}$  is the relative transformation between scanner and IMU coordinate system. The latter is first approximated with  $\phi = -90^\circ$ ,  $\omega = \kappa = 0^\circ$  and  $x = y = z = 0 \text{ mm}$ . The cones are manually extracted from the initially registered 3D point cloud (Fig. 3.1a). Then, the six parameters of  ${}^{wcs} M_{ics}$  are refined in a Gauss-Markov-Optimization, minimizing the distances of the lidar points to the according cone model (eq. 1 and 2 in Sardemann et al., 2023). Fig. 3.1b shows the resulting point cloud of one cone using the optimized relative orientation matrix. The resulting Euler angles have been determined with standard deviations of  $0.004^\circ - 0.018^\circ$ , while the lever arm elements have been determined with standard deviations of  $0.1 \text{ mm} - 0.5 \text{ mm}$ .

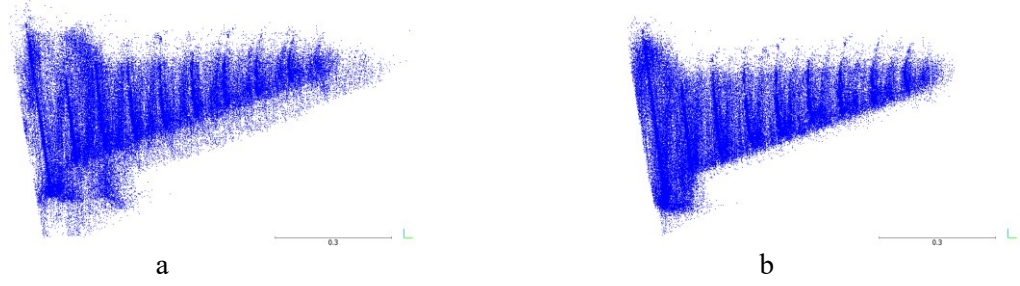


Fig. 3.1: Cone points with approximated (a) and calibrated (b) relative orientation parameters.

### 3.1.2 Theoretical error estimation

The accuracy of an INS-based mobile lidar point cloud can be estimated using the laws of error propagation following the deliberations of section 6.1 in Sardemann et al. (2023). Table 3.1 lists the input standard deviations and their influences on the world coordinates in four different distances. Standard deviations for IMU, GNSS and lidar were taken from manufacturers specifications. Considering the poor conditions for IMU and GNSS, it can be assumed that the accuracies are in fact worse than stated by the manufacturer. The greatest influence on the overall accuracy is caused by the heading error  ${}^{wcs}\kappa_{ics}$ , assuming a moving platform that rotates with a mean angular speed of  $7^\circ/s$ . Temporal synchronisation, which had the greatest influence on accuracy in the camera-based alternative, does not play a role in the INS-based method. It has to be noted, that the simple standard deviation represents only approx. 68% of the measurements values. It was chosen in order to be able to compare the different methods and to reveal the dominant error sources. For a more realistic statement on the system's accuracy, twice (95%) or triple standard deviations (99.7%) should be considered.

Table 3.1: Standard deviations ( $s_{v_i}$ ) of input parameters and their effect on the 3D point standard deviation in mm for world coordinates  ${}^{wcs}\mathbf{s}_{3D}$  in 5, 10, 25 and 50 m distance using INS-based platform orientation.

Input parameter	$s_{v_i}$	${}^{wcs}\mathbf{s}_{3D}$ (mm)			
		5 m	10 m	25 m	50 m
${}^{wcs}\omega_{ics}$ ( $^\circ$ )	0.1	7	14	35	70
${}^{wcs}\phi_{ics}$ ( $^\circ$ )	0.1	7	14	35	71
${}^{wcs}\kappa_{ics}$ ( $^\circ$ )	0.2	14	28	71	143
${}^{wcs}X_{ics}$ (mm)	20	20	20	20	20
${}^{wcs}Y_{ics}$ (mm)	20	20	20	20	20
${}^{wcs}Z_{ics}$ (mm)	30	30	30	30	30
${}^{ics}\omega_{scs}$ ( $^\circ$ )	0.018	1.3	2.6	6.6	13.2
${}^{ics}\phi_{scs}$ ( $^\circ$ )	0.009	0.6	1.2	3.1	6.2
${}^{ics}\kappa_{scs}$ ( $^\circ$ )	0.004	0.3	0.6	1.5	3.0
${}^{ics}X_{scs}$ (mm)	0.5	0.5	0.5	0.5	0.5
${}^{ics}Y_{scs}$ (mm)	0.2	0.2	0.2	0.2	0.2
${}^{ics}Z_{scs}$ (mm)	0.1	0.1	0.1	0.1	0.1
${}^{scs}X$ (mm)	17	17	17	17	17
${}^{scs}Y$ (mm)	17	17	17	17	17
${}^{scs}Z$ (mm)	17	17	17	17	17
<b><math>{}^{3D}{}_{wcs}</math></b>		54	62	101	183

### 3.1.3 De facto achieved accuracies

The resulting INS-based point cloud was compared to a TLS-reference as shown in section 6.2 of Sardemann et al. (2023). Fig. 3.2 shows the cloud to mesh distances considering only the railroad embankment using the same colour scale as in Figure 15 of Sardemann et al. (2023). An overall RMSE of 23 cm was achieved.

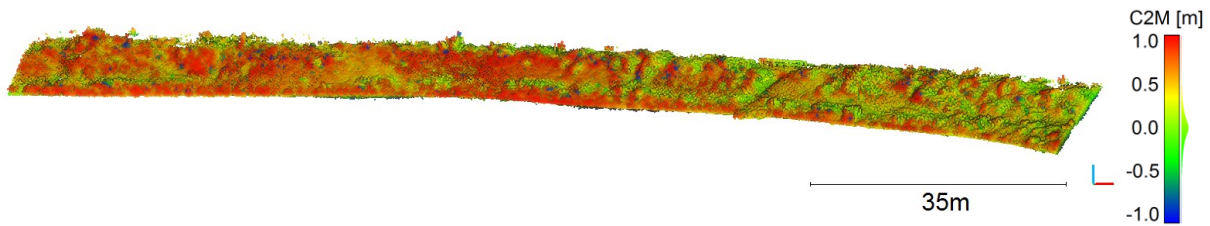


Fig. 3.2: Distances of INS-based mobile lidar point cloud to triangulated TLS-reference.

### 3.1.4 Comparison of both approaches

The previous section showed that the IMU-based method does perform inferior to the camera-based method concerning the accuracy when both methods are compared to a superior reference. This is highlighted in Fig. 3.3, where the point to mesh distances of both approaches are analysed according to their measurement distances.

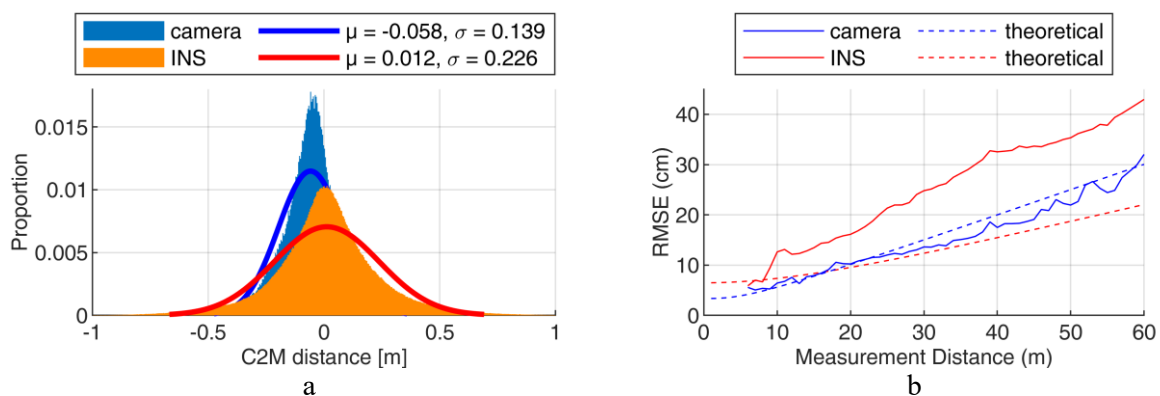


Fig. 3.3: Point distances to reference mesh. a: normalized histograms of INS- and camera-based approach with fitted normal distributions. b: distance dependent theoretical (dashed) and achieved (solid) RMSEs for both approaches.

Table 3.1 and Fig. 3.3b (dashed lines) show, that the INS-based orientation method should theoretically outperform the camera-based method. The standard deviations of IMU and GNSS that were used for error propagation were taken from the manufacturers specifications. However, UWVs navigating on rivers represent an environment where GNSS and IMU can only operate in a limited way and with reduced accuracy as mentioned in Sardemann et al. (2023). The de facto achieved and observed accuracies are therefore inferior to the expected and compared to the camera-based method. However, there are other arguments for both methods that are not represented by the accuracy results alone:

- The INS-based approach enables georeferencing of all recorded Velodyne points. This results in 6 million points for the Freiburger Mulde dataset, compared to 560,000 points that were georeferenced using the camera-based method. The point density is therefore more than 10 times higher.
- The camera-based approach enables georeferencing of mobile lidar points when GNSS is not available. This happens in deep valleys, under bridges or when big structures or dense vegetation is present on the riverbanks.

The before mentioned differences of both positioning and orientation approaches prompts the combination of both methods. Using RTK positions for (part of) the UWV trajectory eliminates the need for control points on the riverbank. Combining both methods in an optimization or Kalman Filter, improves the accuracy and reliability of the platform orientation. The positioning and point cloud accuracy could furthermore be improved using lidar based SLAM (simultaneous localisation and mapping) methods. The INS and camera based poses could be used as approximations for the SLAM algorithm.

## 3.2 Integrating the underwater laser triangulation sensor

In Sardemann et al. (2018) and Sardemann et al. (2023), methods for measuring riverbanks with mobile lidar and cameras have been presented. The UWV is supposed to fulfil measurement tasks underwater as well in order to map the morphology of the whole river. It is therefore equipped with a single beam echo sounder (Sardemann et al., 2018). Echo sounders are limited in shallow depths. Therefore, an underwater laser triangulation sensor has been developed. Sardemann et al., 2021 and Sardemann et al., 2023 evaluated the potential of the sensor in laboratory tests. The following section analyses the feasibility of attaching the underwater laser triangulation system to the UWV and the value of it by using simulated data.

When integrating it into the multisensor system architecture, time synchronisation and relative orientation need to be calibrated. The first could be achieved by triggering the (industrial) camera with a pulse-per-second signal, which is generated by the GNSS receiver and therefore synchronised with GPS time. The relative orientation can be calibrated by a combination of the calibration fields introduced in Sardemann et al. (2021) and Sardemann et al. (2023). Fig. 3.4 shows the UWV with the integrated triangulation sensor.



Fig. 3.4: Underwater laser triangulation sensor system integration in the UWV: set-up (a) and detail view (b).

The laser triangulation sensor can be used as an extension of the underwater measurement system by scanning the bottom of the water in conjunction with the echo sounder. The two measurement methods complement each other through their different measurement ranges. A combination of echo sounder and underwater laser triangulation is particularly useful for recording waters that contain very shallow as well as deeper regions. For an analysis of the benefit of such a combination, a river profile was simulated. The simulated river is an adjusted version of the third river subset used in Krüger et al. (2018) containing bathymetry data of the Ohio River (US Army Corps of Engineers). The dataset was scaled to obtain a small river with a width of approx. 10 m. The depth was adjusted to span a range of 0 to 2.5 m. A zigzag survey was simulated (Fig. 3.5a). It was assumed that the echo sounder provides reliable measurements in depths deeper than 20 cm. For the 5 to 20 cm depth range, laser triangulation can be used. To evaluate the value of the triangulation data, a synthetic data set was generated with triangulation measurements and echo soundings, revealing additional value especially in the shallow areas close to the riverbanks (Fig. 3.5b).

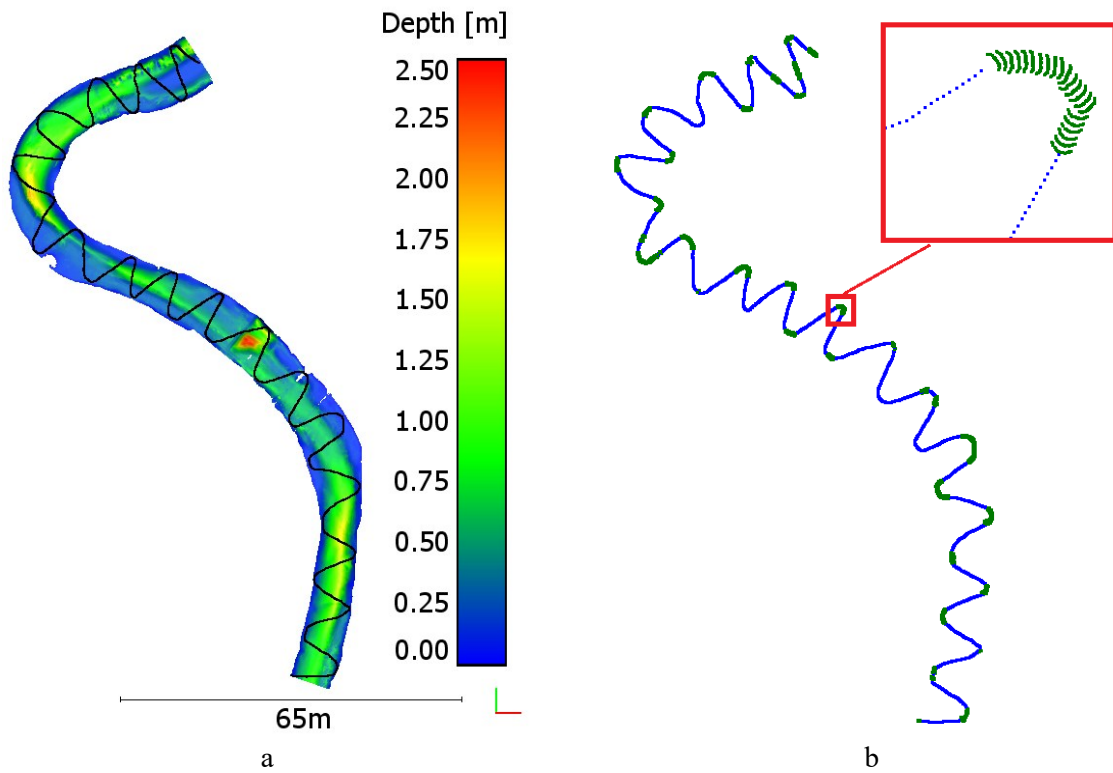


Fig. 3.5: Simulation of combined echo sounder and triangulation measurement. a: River profile with UUV track. b: Echo soundings (blue) and triangulation data (green).

## 4 Ongoing and Future Work

The following paragraphs present experiments and concepts that extend the work that was depicted in the preceding sections. Section 4.1 shows a practical application for UWV-based mobile lidar measurements. Section 4.2 shows an extension of the underwater laser triangulation system.

### 4.1 Deformation Analysis

One application of the UWV is the deformation analysis of riverbanks, i.e. caused by flood events. Such an experiment was conducted at the river Sajó in Hungary. The Sajó is a 230 km long river in Slovakia and Hungary that flows into the Tisza and from there into the Danube, finally issuing into the black sea. The area of interest is a segment of the Sajó close to Miskolc in Northeastern Hungary. It is characterized with sandy riverbanks that are almost vertical and are affected by regular erosion due to flood events. The consequences of the large deformations of the riverbanks for farmers and the environment necessitate a monitoring of it. It was therefore studied in multiple field campaigns with various sensor systems, including the UWV, an UAV with RGB and thermal cameras and an ADCP (Acoustic Doppler Current Profiler) boat. These field campaigns were part of an exchange project between the TU Dresden and the University of Debrecen (Bertalan et al., 2019). Fig. 4.1 shows UAV-based orthophotos of the river segment in October 2019, October 2020 and September 2021. In 2019 and 2021, joint field campaigns were carried out including scientists and material from both universities. Between those two campaigns, there was a flood event in 2020, which was recorded with an UAV by the Debrecen team. The flood event resulted in erosion of the undercut bank. This erosion could be observed as a deformation in the UWV based point clouds of both years.

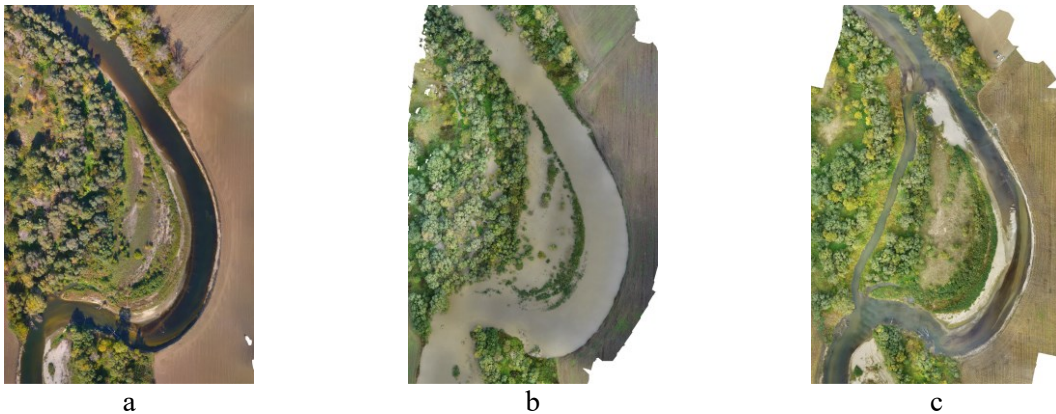


Fig. 4.1: Orthophotos of Sajó River segment in 2019 (a), 2020 (b) and 2021 (c).

Mobile lidar point clouds were recorded using the method described in Sardemann et al. (2023). The platform position and orientation was determined using images of a time-lapse camera. The 2019 version of the UWV had the Ricoh Theta V 360° camera attached. Thus, panorama images have been used for SfM in Metashape. The 2021 version had the Panasonic camera attached, which was pointed to the left riverbank and used for SfM as described in Sardemann et al. (2023). For an estimation of the accuracy of the two point clouds, error propagation was applied as described in section 6.1 of Sardemann et al. (2023). The input standard deviations of the calibrations and SfM-based platform orientations were applied as well as the speeds of the UWV and the measured distances. These calculations result in RMSEs of 15 cm (2019) and 19 cm (2021).

Fig. 4.2c shows both recorded epochs, revealing an erosion that was quantitatively confirmed with a cloud-to-cloud distance calculation (Fig. 4.2d). A maximum deformation of approx. 7 m could be observed on the undercut bank. Thus, the deformation is significant based on the accuracy. Areas, that were only exposed in 2021, due to dryer conditions, were neglected in the comparison. These areas and the remaining riverbed could also be compared using the recorded echo sounder data (Sardemann et al.,

2018) and UAV based bathymetry recorded with multimedia photogrammetry (Eltner et al., 2021). A paper containing more detailed analyses of the erosion process is in preparation.

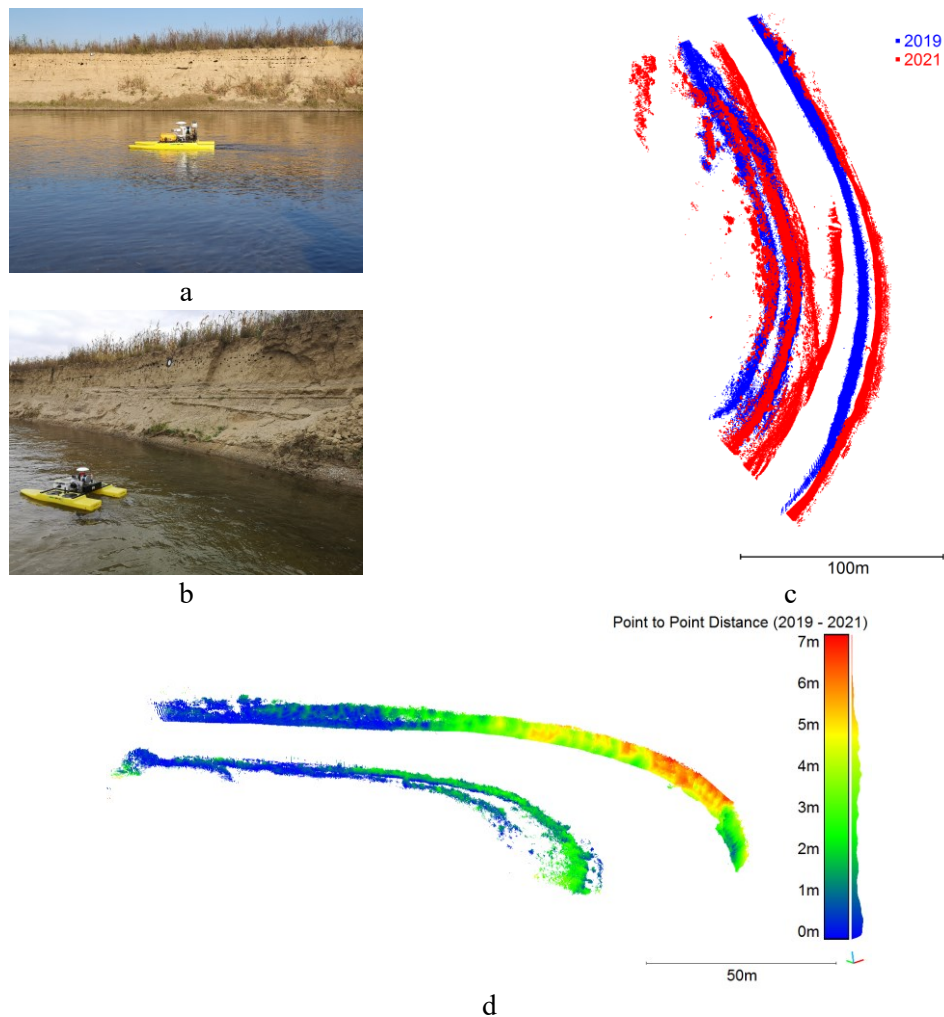


Fig. 4.2: Multitemporal deformation analysis using the UWV at the Sajo River. Data acquisition in 2019 (a) and 2021 (b), mobile lidar point clouds of 2019 (blue) and 2021 (red) (c) and point to point distances of 2021 in comparison to 2019 (d).

## 4.2 Multiline Underwater Laser Triangulation

A useful extension to the system presented in section 5 is a laser diode, which projects multiple parallel lines. By that, a simultaneous 3D measurement could be achieved within one camera shot, utilising more space of the image sensor. Fig. 4.3 shows a simulation of the sensor system using a laser diode with 15 lines.

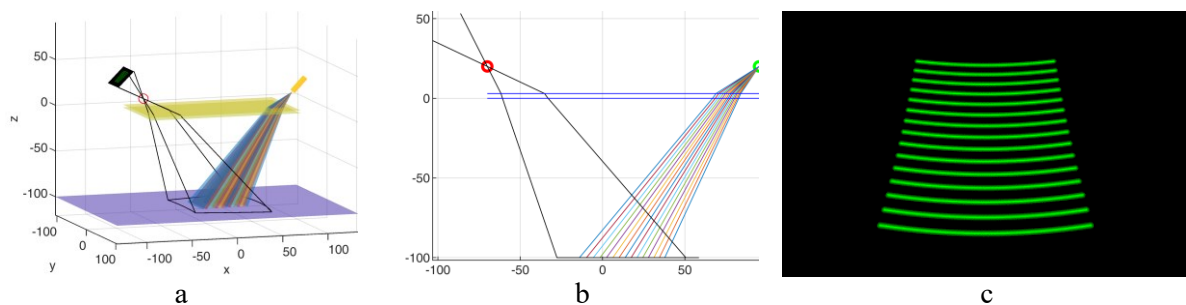


Fig. 4.3: Simulation of a multiline underwater laser triangulation sensor system. a: 3D view, b: 2D section, c: measurement image.

For a first analysis of the feasibility of such a system, a green laser diode with 15 lines was tested using the setup of section 5. Therefore, the single laser line projector was replaced by a laser module that uses diffractive optical elements to project 15 parallel lines. The angular distances between the lines is given by the manufacturer Laser Components with  $1.7^\circ$ , resulting in a (vertical) opening angle of  $23.8^\circ$  for all 15 lines. Each line has a (horizontal) opening angle of  $28.2^\circ$ .

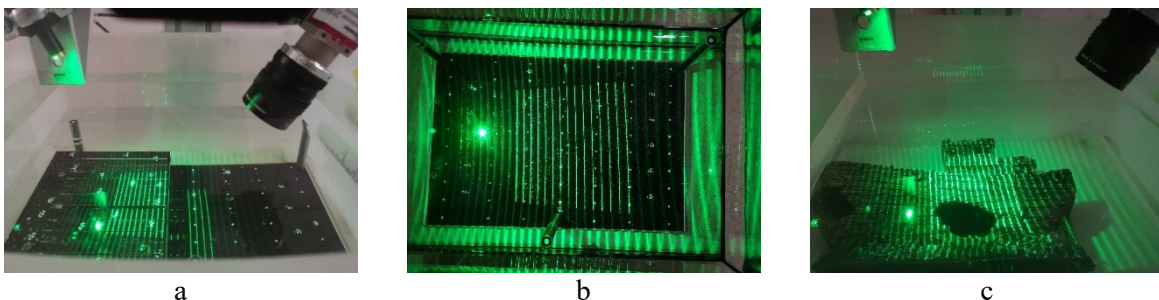
#### 4.2.1 Calibration

The system can be calibrated with the setup presented in Sardemann et al. (2023). Two physical models can be applied for the calibration:

- Calibration of each line separately. Every line is considered as a separate laser diode, resulting in 15 exterior orientation sets (90 parameters).
- Calibration of a multiline laser diode. Assuming one optical centre and regular distances between the laser lines reduces the number of parameters and therefore stabilizes the optimization. This results in one exterior orientation set and one angular step (7 parameters).

Both calibration approaches were tested with the prototype sensor system (Fig. 4.4a). First, the laser lines and line segments were detected using least squares matching (LSM), as described in Sardemann et al. (2021). The existing calibration pattern only enabled the visibility of six lines on both the top and the bottom calibration plane. The gaps in the line on the upper plate and the corresponding line segments on the bottom plate were used for a calibration of the exterior orientation of the laser (red x in Fig. 4.4d). Therefore, six laser orientations were calibrated using the first approach (36 parameters). The calibration of each line separately revealed that the spacing between the lines is in fact not regular and that there is no exact joint optical centre for all lines. Each line was calibrated with an a posteriori standard deviation of 1 pixel. The system was furthermore calibrated with the second approach. Therefore, the remaining lines that are only visible on one of the planes are also included in the optimization process. The laser diode was considered as one element with a joint exterior orientation and a regular angular spacing between the lines. This resulted, as expected from the first calibration, in inferior accuracies for the calibrated parameters and for the overall a posteriori standard deviation (4 pixels) in the optimization process. However, this approach enables the utilisation of all 15 lines for subsequent measurements.

The calibrated multiline underwater laser triangulation system was used to acquire a 3D point cloud of a planar object (Fig. 4.4b, e). Using both calibrated parameter sets for the measurement of the plane, which was placed under water at a known distance, confirmed the assumption that the second model does correspond inferior to reality and is not able to exactly model the optical behaviour of the multiline laser. Using the first model (individual line parameters) resulted in a RMSE of 0.13 mm, while the second model resulted in a RMSE of 0.17 mm for the same 6 lines and 0.32 mm for all 15 lines. A calibration model, modelling the complete multiline diode with additional parameters is aimed to be found in future research. Using the sensor system for the measurement of a 3D object that is not flat (Fig. 4.4c), reveals the predominant problem of assigning an image observation to the corresponding laser line. The wreck model that was introduced in Sardemann et al. (2022) was placed under water underneath the sensor system. Fig. 4.4f shows the measurement image acquired by the camera. It is still possible to detect the laser lines in the image, but they are not clearly assignable to the corresponding line, especially at jumps in heights. This problem will be addressed in future research.



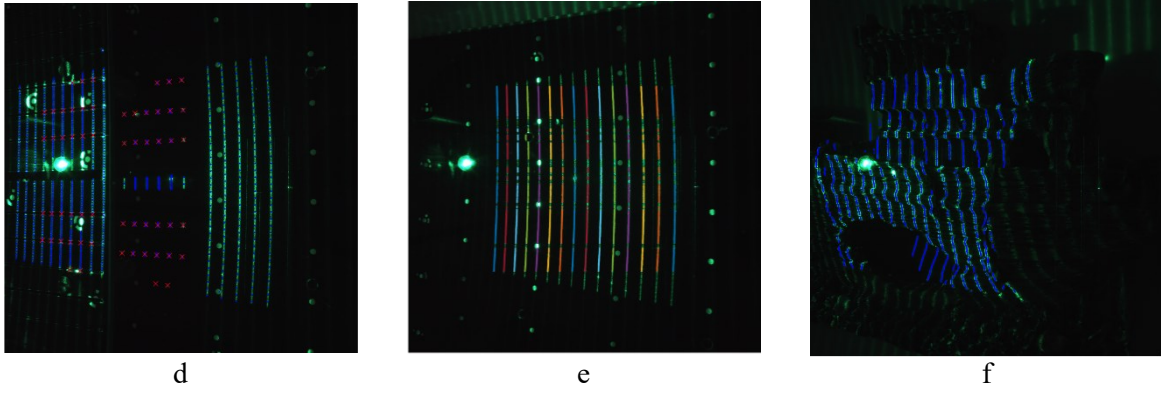


Fig. 4.4: Multilane underwater triangulation system: Calibration (a, d) and measurement of plane (b, e) and wreck model (c, f). a – c: measurement setup, d – f: camera images with detected lines.



## 5 Conclusion

This thesis introduced an uncrewed water vehicle used as a photogrammetric multisensor platform. The UWV was developed with the scope of photogrammetric measurements of river morphologies. It was therefore equipped with multiple sensors to simultaneously scan the riverbanks and the river bottom. First, the general feasibility of the UWV for river mapping was analysed and how the acquired data can be fused with other data, for example from UAV. This revealed one major issue that occurs when an UWV is applied on a river that is surrounded by larger vegetation or geological formations: Satellite based positioning is not reliable in this environment. Additionally, IMU based orientation determination on a small platform suffers from errors caused by electromagnetic fields emitted from the boat rotors and the rotating sensors. Therefore, an alternative positioning and orientation approach was analysed. Using camera images acquired in time-lapse mode enables a SfM based trajectory of the camera on board. In order to use this trajectory for the orientation of mobile lidar points, an accurate relative orientation has to be known. A calibration process was presented that enables an accurate calibration of relative orientations. At the same time, it only needs the image and scan from one viewpoint for the calibration, while existing calibration methods rely on multiple recordings of a moving object. Extending the calibration procedure to a kinematic method enabled the calibration of time synchronisation between camera and lidar sensor. The kinematic calibration process was furthermore applied for a determination of the relative orientation between IMU and camera or lidar.

Subsequently, the topic of underwater measurements was addressed. An underwater laser triangulation sensor was developed that enables sub-mm accurate depth measurements in close range applications. First, the physical and mathematical models that need to be applied for a strict geometric modelling of the measurement process were presented. When a planar laser light sheet hits a media interface, it is refracted. For the presented sensor, this happens twice when the line laser travels from air through glass into water and twice on its way back from water, through glass onto the camera sensor that is also in air. The exact ray path needed to be determined for every observation with the underwater laser triangulation sensor. Based on the simulations, a sensor was developed and presented. A theoretical and practical accuracy analysis of the underwater laser triangulation sensor was conducted. Practical experiments were performed in a laboratory setting. Standard deviations of 0.3 mm have been achieved in measurement distances of up to 14 cm. An integration of the underwater triangulation sensor to the UWV multisensor set-up was also tested briefly.

It has been demonstrated, that the developed UWV-based multisensor system is a useful tool for the geometric measurement of rivers. High-resolution measurements of rivers form a basis for (flash) flood analysis. It has been demonstrated that a deformation analysis of a river reach can be determined in order to detect the effects on the landscape.



## 6 Literature

3D scanning with ATOS. GOM Metrology. URL <https://www.gom.com/en/products/3d-scanning> (accessed 6.15.23).

Ackermann, F., 1984. Digital image correlation: performance and potential application in photogrammetry. *The Photogrammetric Record* 11, 429–439.

Bai, X., Li, B., Xu, X., Xiao, Y., 2022. A Review of Current Research and Advances in Unmanned Surface Vehicles. *J. Marine. Sci. Appl.* 21, 47–58. <https://doi.org/10.1007/s11804-022-00276-9>

Bertalan, L., Nagy, B., Szopos, N., Eltner, A., Sardemann, H., Mader, D., 2019. Medertopográfiai és hidrometriai vizsgálatok a Sajó mentén pilóta nélküli vízi- és légi járművekkel, in: *Theory Meets Practice in GIS*. Debrecen University Press, pp. 55–60.

Bleier, M., van der Lucht, J., Nüchter, A., 2019. Towards an underwater 3D laser scanning system for mobile mapping, in: *Proceedings of the IEEE ICRA Workshop on Underwater Robotic Perception (ICRAURP'19)*. Montreal, Canada.

Bodenmann, A., Thornton, B., Ura, T., 2017. Generation of High-resolution Three-dimensional Reconstructions of the Seafloor in Color using a Single Camera and Structured Light: Generation of High-Resolution. *J. Field Robotics* 34, 833–851. <https://doi.org/10.1002/rob.21682>

Borga, M., Gaume, E., Creutin, J.D., Marchi, L., 2008. Surveying flash floods: gauging the ungauged extremes. *Hydrol. Process.* 22, 3883–3885. <https://doi.org/10.1002/hyp.7111>

Castillón, M., Palomer, A., Forest, J., Ridao, P., 2019. State of the Art of Underwater Active Optical 3D Scanners. *Sensors* 19, 5161. <https://doi.org/10.3390/s19235161>

Cheng, Y., Jiang, M., Zhu, J., Liu, Y., 2021. Are We Ready for Unmanned Surface Vehicles in Inland Waterways? The USV Inland Multisensor Dataset and Benchmark. *IEEE Robot. Autom. Lett.* 6, 3964–3970. <https://doi.org/10.1109/LRA.2021.3067271>

Ekkel, T., Schmik, J., Luhmann, T., Hastedt, H., 2015. PRECISE LASER-BASED OPTICAL 3D MEASUREMENT OF WELDING SEAMS UNDER WATER. *Int. Arch. Photogramm. Remote Sens. Spatial Inf. Sci.* XL-5/W5, 117–122. <https://doi.org/10.5194/isprsarchives-XL-5-W5-117-2015>

Elhashash, M., Albanwan, H., Qin, R., 2022. A Review of Mobile Mapping Systems: From Sensors to Applications. *Sensors* 22, 4262. <https://doi.org/10.3390/s22114262>

Eltner, A., Bertalan, L., Grundmann, J., Perks, M.T., Lotsari, E., 2021. Hydro-morphological mapping of river reaches using videos captured with UAS. *Earth Surf Processes Landf* 46, 2773–2787. <https://doi.org/10.1002/esp.5205>

Eltner, A., Elias, M., Sardemann, H., Spieler, D., 2018. Automatic Image-Based Water Stage Measurement for Long-Term Observations in Ungauged Catchments. *Water Resour. Res.* 54. <https://doi.org/10.1029/2018WR023913>

Eltner, A., Hoffmeister, D., Kaiser, A., Karrasch, P., Stöcker, C., Rovere, A., 2022. UAVs for the Environmental Sciences. *wbg Academic*.

Flexpoint Machine Vision Lasers MVmicro series. Laser Components. URL [https://www.lasercomponents.com/fileadmin/user\\_upload/home/Datasheets/laser-modules/mv\\_micro.pdf](https://www.lasercomponents.com/fileadmin/user_upload/home/Datasheets/laser-modules/mv_micro.pdf) (accessed 6.15.23).

GigE Vision Cameras. Mako. Technical Manual. Allied Vision. URL [https://cdn.alliedvision.com/fileadmin/content/documents/products/cameras/Mako/techman/Mako\\_TechMan\\_en.pdf](https://cdn.alliedvision.com/fileadmin/content/documents/products/cameras/Mako/techman/Mako_TechMan_en.pdf) (accessed 6.15.23).

Glassner, A.S., 1989. Surface physics for ray tracing, in: *An Introduction to Ray Tracing*. Academic San Diego, Calif., pp. 121–160.

González, E.P., Díaz-Pache, F.S.-T., Mosquera, L.P., Agudo, J.P., 2007. Bidimensional measurement of an underwater sediment surface using a 3D-Scanner. *Optics & Laser Technology* 39, 481–489. <https://doi.org/10.1016/j.optlastec.2005.11.007>

Hale, G.M., Querry, M.R., 1973. Optical Constants of Water in the 200-nm to 200- $\mu$ m Wavelength Region. *Appl. Opt.* 12, 555. <https://doi.org/10.1364/AO.12.000555>

Hydrographic survey data. US Army Corps of Engineers: URL <http://www.lrp.usace.army.mil/Missions/Navigation/Navigation-Charts/HydrographicSurveyData/> (accessed 6.15.23).

Inglis, G., Smart, C., Vaughn, I., Roman, C., 2012. A pipeline for structured light bathymetric mapping, in: 2012 IEEE/RSJ International Conference on Intelligent Robots and Systems. Presented at the 2012 IEEE/RSJ International Conference on Intelligent Robots and Systems (IROS 2012), IEEE, Vilamoura-Algarve, Portugal, pp. 4425–4432. <https://doi.org/10.1109/IROS.2012.6386038>

Jong, C.D. de (Ed.), 2010. *Hydrography*, 1. ed., corr. 2010. ed, Series on mathematical geodesy and positioning. VSSD, Delft.

Kidd, J.R., n.d. Performance Evaluation of the Velodyne VLP-16 System for Surface Feature Surveying. University of New Hampshire.

Kim, E., Park, S.-Y., 2019. Extrinsic Calibration between Camera and LiDAR Sensors by Matching Multiple 3D Planes. *Sensors* 20, 52. <https://doi.org/10.3390/s20010052>

Klopper, F., Hammerle, M., Hofle, B., 2017. Assessing the Potential of a Low-Cost 3-D Sensor in Shallow-Water Bathymetry. *IEEE Geosci. Remote Sensing Lett.* 14, 1388–1392. <https://doi.org/10.1109/LGRS.2017.2713991>

Krüger, R., Karrasch, P., Bernard, L., 2018. Evaluating Spatial Data Acquisition and Interpolation Strategies for River Bathymetries, in: Mansourian, A., Pilesjö, P., Harrie, L., Van Lammeren, R. (Eds.), *Geospatial Technologies for All, Lecture Notes in Geoinformation and Cartography*. Springer International Publishing, Cham, pp. 3–25. [https://doi.org/10.1007/978-3-319-78208-9\\_1](https://doi.org/10.1007/978-3-319-78208-9_1)

Lewicka, O., Specht, M., Stateczny, A., Specht, C., Dardanelli, G., Brčić, D., Szostak, B., Halicki, A., Stateczny, M., Widźgowski, S., 2022. Integration Data Model of the Bathymetric Monitoring System for Shallow Waterbodies Using UAV and USV Platforms. *Remote Sensing* 14, 4075. <https://doi.org/10.3390/rs14164075>

Liebold, F., Maas, H.-G., 2014. Integrated Georeferencing of LiDAR and Camera Data Acquired from a Moving Platform. *Int. Arch. Photogramm. Remote Sens. Spatial Inf. Sci.* XL–3, 191–196. <https://doi.org/10.5194/isprsarchives-XL-3-191-2014>

Luhmann, T., 2009. Precision potential of photogrammetric 6DOF pose estimation with a single camera. *ISPRS Journal of Photogrammetry and Remote Sensing* 64, 275–284. <https://doi.org/10.1016/j.isprsjprs.2009.01.002>

Macario Barros, A., Michel, M., Moline, Y., Corre, G., Carrel, F., 2022. A Comprehensive Survey of Visual SLAM Algorithms. *Robotics* 11, 24. <https://doi.org/10.3390/robotics11010024>

Mader, D., Westfeld, P., Maas, H.-G., 2014. An Integrated Flexible Self-calibration Approach for 2D Laser Scanning Range Finders Applied to the Hokuyo UTM-30LX-EW. *Int. Arch. Photogramm. Remote Sens. Spatial Inf. Sci.* XL–5, 385–393. <https://doi.org/10.5194/isprsarchives-XL-5-385-2014>

- Mandlbürger, G., 2022. A review of active and passive optical methods in hydrography. *IHR* 28, 8–52. <https://doi.org/10.58440/ihr-28-a15>
- Mandlbürger, G., Monetti, D., Greifeneder, C., 2022. Fließgewässervermessung mittels UAV-basierter Laserbathymetrie im Produktiveinsatz. Large-scale river survey using UAV-based laser bathymetry in production use 2022, 59–77.
- Mandlbürger, G., Pfennigbauer, M., Schwarz, R., Flöry, S., Nussbaumer, L., 2020. Concept and Performance Evaluation of a Novel UAV-Borne Topo-Bathymetric LiDAR Sensor. *Remote Sensing* 12, 986. <https://doi.org/10.3390/rs12060986>
- Manfreda, S., Dor, E.B., 2023. Unmanned Aerial Systems for Monitoring Soil, Vegetation, and Riverine Environments. Elsevier. <https://doi.org/10.1016/C2020-0-02177-8>
- Massot-Campos, M., Oliver, G., Bodenmann, A., Thornton, B., 2016. Submap bathymetric SLAM using structured light in underwater environments, in: 2016 IEEE/OES Autonomous Underwater Vehicles (AUV). Presented at the 2016 IEEE/OES Autonomous Underwater Vehicles (AUV), IEEE, Tokyo, Japan, pp. 181–188. <https://doi.org/10.1109/AUV.2016.7778669>
- Matos, G., Buschinelli, P., Pinto, T., 2020. Underwater Laser Triangulation Sensor Model With Flat Refractive Interfaces. *IEEE J. Oceanic Eng.* 45, 937–945. <https://doi.org/10.1109/JOE.2019.2891863>
- Maurelli, F., Krupiński, S., Xiang, X., Petillot, Y., 2022. AUV localisation: a review of passive and active techniques. *Int J Intell Robot Appl* 6, 246–269. <https://doi.org/10.1007/s41315-021-00215-x>
- Merwade, V.M., Maidment, D.R., Goff, J.A., 2006. Anisotropic considerations while interpolating river channel bathymetry. *Journal of Hydrology* 331, 731–741. <https://doi.org/10.1016/j.jhydrol.2006.06.018>
- Moore, K.D., Jaffe, J.S., 2002. Time-evolution of high-resolution topographic measurements of the sea floor using a 3-D laser line scan mapping system. *IEEE J. Oceanic Eng.* 27, 525–545. <https://doi.org/10.1109/JOE.2002.1040936>
- Mueller, E.N., Pfister, A., 2011. Increasing occurrence of high-intensity rainstorm events relevant for the generation of soil erosion in a temperate lowland region in Central Europe. *Journal of Hydrology* 411, 266–278. <https://doi.org/10.1016/j.jhydrol.2011.10.005>
- Mulson, C., 2010. A flexible multi-media bundle approach. *The International Archives of the Photogrammetry, Remote Sensing and Spatial Information Sciences XXXVIII-5*, 472–477.
- Mulson, C., Mandlbürger, G., Maas, H.-G., 2020. COMPARISON OF SUBAQUATIC DIGITAL ELEVATION MODELS FROM AIRBORNE LASER SCANNING AND IMAGERY. *ISPRS Ann. Photogramm. Remote Sens. Spatial Inf. Sci.* V-2-2020, 671–677. <https://doi.org/10.5194/isprs-annals-V-2-2020-671-2020>
- Mulson, C., Schulze, M., Westfeld, P., 2006. AN OPTICAL TRIANGULATION METHOD FOR HEIGHT MEASUREMENTS ON INSTATIONARY WATER SURFACES. *The International Archives of the Photogrammetry, Remote Sensing and Spatial Information Sciences XXXVI-5*, 213–217.
- Nister, D., Naroditsky, O., Bergen, J., 2004. Visual odometry, in: Proceedings of the 2004 IEEE Computer Society Conference on Computer Vision and Pattern Recognition, 2004. CVPR 2004. Presented at the Proceedings of the 2004 IEEE Computer Society Conference on Computer Vision and Pattern Recognition, 2004. CVPR 2004., IEEE, Washington, DC, USA, pp. 652–659. <https://doi.org/10.1109/CVPR.2004.1315094>
- Noss, C., Wilkinson, J., Lorke, A., 2018. Triangulation hand-held laser-scanning (TriHaLaS) for micro- and meso-habitat surveys in streams: Laser triangulation surveys in streams. *Earth Surf. Process. Landforms* 43, 1241–1251. <https://doi.org/10.1002/esp.4310>

- Palomer, A., Ridao, P., Ribas, D., Forest, J., 2017. Underwater 3D laser scanners: The deformation of the plane, in: *Sensing and Control for Autonomous Vehicles: Applications to Land, Water and Air Vehicles*. Springer, pp. 73–88.
- Palomer, A., Ridao, P., Youakim, D., Ribas, D., Forest, J., Petillot, Y., 2018. 3D Laser Scanner for Underwater Manipulation. *Sensors* 18, 1086. <https://doi.org/10.3390/s18041086>
- Pusztai, Z., Hajder, L., 2017. Accurate Calibration of LiDAR-Camera Systems Using Ordinary Boxes, in: *2017 IEEE International Conference on Computer Vision Workshops (ICCVW)*. Presented at the 2017 IEEE International Conference on Computer Vision Workshop (ICCVW), IEEE, Venice, Italy, pp. 394–402. <https://doi.org/10.1109/ICCVW.2017.53>
- Roman, C., Inglis, G., Rutter, J., 2010. Application of structured light imaging for high resolution mapping of underwater archaeological sites, in: *OCEANS'10 IEEE SYDNEY*. IEEE, pp. 1–9.
- Ross, B.J., 2014. COSC 3P98: Ray Tracing Basics. Brock University, St. Catharines, Canada ([www.cosc.brocku.ca/Offerings/3P98/course/assignments/RayTracing.pdf](http://www.cosc.brocku.ca/Offerings/3P98/course/assignments/RayTracing.pdf)) 17–19.
- Røy, H., Hüttel, M., Jørgensen, B.B., 2002. The role of small-scale sediment topography for oxygen flux across the diffusive boundary layer. *Limnol. Oceanogr.* 47, 837–847. <https://doi.org/10.4319/lo.2002.47.3.0837>
- Santillan, J.R., Serviano, J.L., Makinano-Santillan, M., Marqueso, J.T., 2016. INFLUENCE OF RIVER BED ELEVATION SURVEY CONFIGURATIONS AND INTERPOLATION METHODS ON THE ACCURACY OF LIDAR DTM-BASED RIVER FLOW SIMULATIONS. *Int. Arch. Photogramm. Remote Sens. Spatial Inf. Sci.* XLII-4/W1, 225–235. <https://doi.org/10.5194/isprs-archives-XLII-4-W1-225-2016>
- Sardemann, H., Eltner, A., Maas, H.-G., 2018. ACQUISITION OF GEOMETRICAL DATA OF SMALL RIVERS WITH AN UNMANNED WATER VEHICLE. *Int. Arch. Photogramm. Remote Sens. Spatial Inf. Sci.* XLII-2, 1023–1027. <https://doi.org/10.5194/isprs-archives-XLII-2-1023-2018>
- Sardemann, H., Mulsow, C., Maas, H.-G., 2022. Accuracy Analysis of an Oblique Underwater Laser Lightsheet Triangulation System. *PFG* 90, 3–18. <https://doi.org/10.1007/s41064-022-00196-x>
- Sardemann, H., Mulsow, C., Maas, H.-G., 2021. STRICT GEOMETRIC CALIBRATION OF AN UNDERWATER LASER TRIANGULATION SYSTEM. *Int. Arch. Photogramm. Remote Sens. Spatial Inf. Sci.* XLIII-B2-2021, 689–692. <https://doi.org/10.5194/isprs-archives-XLIII-B2-2021-689-2021>
- Schiebener, P., Straub, J., Levelt Sengers, J.M.H., Gallagher, J.S., 1990. Refractive index of water and steam as function of wavelength, temperature and density. *Journal of Physical and Chemical Reference Data* 19, 677–717. <https://doi.org/10.1063/1.555859>
- Schneider, D., Blaskow, R., 2021. BOAT-BASED MOBILE LASER SCANNING FOR SHORELINE MONITORING OF LARGE LAKES. *Int. Arch. Photogramm. Remote Sens. Spatial Inf. Sci.* XLIII-B2-2021, 759–762. <https://doi.org/10.5194/isprs-archives-XLIII-B2-2021-759-2021>
- SeaVision Precision Underwater ImagingURL [https://krakenrobotics.com/themencode-pdf-viewer/?file=https://krakenrobotics.com/wp-content/uploads/2020/11/SeaVision-2020\\_rev-1.1.pdf](https://krakenrobotics.com/themencode-pdf-viewer/?file=https://krakenrobotics.com/wp-content/uploads/2020/11/SeaVision-2020_rev-1.1.pdf) (accessed 6.15.23).
- Shortis, M., 2015. Calibration Techniques for Accurate Measurements by Underwater Camera Systems. *Sensors* 15, 30810–30826. <https://doi.org/10.3390/s151229831>
- Tauro, F., Porfiri, M., Grimaldi, S., 2016. Surface flow measurements from drones. *Journal of Hydrology* 540, 240–245. <https://doi.org/10.1016/j.jhydrol.2016.06.012>

Tauro, F., Selker, J., Van De Giesen, N., Abrate, T., Uijlenhoet, R., Porfiri, M., Manfreda, S., Caylor, K., Moramarco, T., Benveniste, J., Ciralo, G., Estes, L., Domeneghetti, A., Perks, M.T., Corbari, C., Rabiei, E., Ravazzani, G., Bogena, H., Harfouche, A., Brocca, L., Maltese, A., Wickert, A., Tarpanelli, A., Good, S., Lopez Alcala, J.M., Petroselli, A., Cudenneq, C., Blume, T., Hut, R., Grimaldi, S., 2018. Measurements and Observations in the XXI century (MOXXI): innovation and multi-disciplinarity to sense the hydrological cycle. *Hydrological Sciences Journal* 63, 169–196. <https://doi.org/10.1080/02626667.2017.1420191>

Tetlow, S., Spours, J., 1999. Three-dimensional measurement of underwater work sites using structured laser light. *Meas. Sci. Technol.* 10, 1162–1167. <https://doi.org/10.1088/0957-0233/10/12/307>

Underwater Laser Scanners. Newton Labs. URL [https://www.newtonlabs.com/subsea\\_scanners-1.htm](https://www.newtonlabs.com/subsea_scanners-1.htm) (accessed 6.15.23).

van der Lucht, J., Bleier, M., Leutert, F., Schilling, K., Nüchter, A., 2018. STRUCTURED-LIGHT BASED 3D LASER SCANNING OF SEMI-SUBMERGED STRUCTURES. *ISPRS Annals of Photogrammetry, Remote Sensing & Spatial Information Sciences* 4.

VLP-16 User Manual 63-9243 Rev. E.. Velodyne Lidar.

Voyis. Insight Underwater Laser Scanners. Seatronics. URL [https://seatronics-group.com/wp-content/uploads/2020/04/Voyis\\_LaserScanners\\_DataSheet.pdf](https://seatronics-group.com/wp-content/uploads/2020/04/Voyis_LaserScanners_DataSheet.pdf)

Ying, X., Wang, G., Mei, X., Yang, S., Rong, J., Zha, H., 2014. A direct method for the extrinsic calibration of a camera and a line scan LIDAR, in: 2014 IEEE International Conference on Mechatronics and Automation. Presented at the 2014 IEEE International Conference on Mechatronics and Automation (ICMA), IEEE, Tianjin, China, pp. 571–576. <https://doi.org/10.1109/ICMA.2014.6885760>

Zhang, W., Jiang, F., Yang, C.-F., Wang, Z.-P., Zhao, T.-J., 2021. Research on Unmanned Surface Vehicles Environment Perception Based on the Fusion of Vision and Lidar. *IEEE Access* 9, 63107–63121. <https://doi.org/10.1109/ACCESS.2021.3057863>



## List of Figures

Fig. 2.1	Development stages of the UWV .....	3
Fig. 2.2	3D printed sensor mounts for antenna and panorama camera .....	3
Fig. 2.3	Sensor configuration and system architecture of the multisensory system .....	4
Fig. 2.4	Central control unit .....	6
Fig. 3.1	Cone points with approximated and calibrated relative orientation parameters .....	60
Fig. 3.2	Distances of INS-based mobile lidar point cloud to triangulated TLS-reference .....	61
Fig. 3.3	Point distances to reference mesh .....	61
Fig. 3.4	Underwater laser triangulation sensor system integration in the UWV .....	62
Fig. 3.5	Simulation of combined echo sounder and triangulation measurement .....	63
Fig. 4.1	Orthophotos of Sajo River segment in 2019, 2020 and 2021 .....	64
Fig. 4.2	Multitemporal deformation analysis using the UWV at the Sajo River .....	65
Fig. 4.3	Simulation of a multiline underwater laser triangulation sensor system .....	65
Fig. 4.4	Multiline underwater triangulation system .....	67

## Figures of Sardemann et al., 2018

Figure 1	Multi Sensor UWV with Lidar, 360° camera, echo sounder (hidden) and GNSS-supported IMU .....	9
Figure 2	Calibration of relative orientations .....	11
Figure 3	Survey configuration on the river Freiberger Mulde .....	11
Figure 4	Lidar point cloud of a 1.5 km segment of the river Freiberger Mulde .....	12
Figure 5	Details of the lidar point cloud .....	12
Figure 6	Results of a test surveys on the river Freiberger Mulde .....	12

## Figures of Sardemann et al., 2023

Figure 1	UWV trajectory .....	20
Figure 2	Calibration field set-up .....	20
Figure 3	Cone coordinate system .....	21
Figure 4	Synthetic camera image and synthetic lidar frame of the cone-based calibration field .....	21
Figure 5	The uncrewed water vehicle used in this study .....	23
Figure 6	Freiberger Mulde .....	24
Figure 7	Terrestrial laser scan of the Freiberger Mulde (reflectance colorized) .....	24
Figure 8	Geometric calibration .....	25
Figure 9	Time offset calibration .....	25
Figure 10	Image Orientation determination and georeferencing .....	26
Figure 11	Oriented mobile lidar point cloud .....	26

Figure 12	Measurement image used for SfM .....	27
Figure 13	Determination of camera clock offset .....	28
Figure 14	Mobile lidar point cloud to TLS mesh distance .....	30
Figure 15	Cross section of mobile lidar point cloud and TLS point cloud .....	30
Figure 16	Mobile lidar point cloud to TLS mesh distance .....	30
Figure 17	Footprints of mobile lidar .....	32

## Figures of Sardemann et al., 2021

Figure 1	Deformation of a laser light-sheet penetrating from air through glass into water and their appearance on a planar surface .....	37
Figure 2	Laser line detection with LSM .....	38
Figure 3	Intersection of image ray and sub beam of an image measurement on the line .....	38
Figure 4	Calibration set-up. 3D-scheme and camera image .....	39
Figure 5	Measurement volume of a given camera-laser-set-up .....	39
Figure 6	Set-up of the experiment, before camera and laser orientation were adjusted .....	39
Figure 7	Calibration set-up and image with corresponding points on both levels and additional points across the line .....	39
Figure 8	Measurement object consisting of ground plate and measurement panel .....	40
Figure 9	Laser line measurement in the image with LSM-based image measurements and epipolar lines of the reference depths .....	40
Figure 10	Distance between measurement and reference in mm for 128.9 mm and 122.7 mm depth .....	40

## Figures of Sardemann et al., 2022

Fig. 1	Deformation of laser lightsheet at air-glass and glass-water interfaces .....	46
Fig. 2	Deformed laser line on a planar underwater surface, rotated around the y-axis with $45^\circ$ and additionally around the x-axis with $30^\circ$ .....	46
Fig. 3	System setup .....	46
Fig. 4	Laser line in measurement image with row- and patch-based detection for detail and complete line .....	47
Fig. 5	Grey-value profiles of three adjacent rows in the green channel in the centre of Fig. 4 with fitted Gaussian curves .....	47
Fig. 6	LSM: patch and matching result .....	48
Fig. 7	Determination of 3D coordinate by intersection of image point with laser lightsheet ..	48
Fig. 8	6-DOF determination .....	49
Fig. 9	Calibration pattern, setup and image with observations on top and bottom level .....	49
Fig. 10	Calibration result .....	50
Fig. 11	Look-Up-Tables giving the corresponding x-, y- and z-coordinates for every pixel ....	50

Fig. 12	Measurement volume .....	50
Fig. 13	Variance propagation .....	52
Fig. 14	Test object .....	52
Fig. 15	Wreck model .....	52
Fig. 16	Detail of image measurement of test object with white markers on black background	53
Fig. 17	Setup for scanning mode .....	53
Fig. 18	Measurement images of a single profile scan of test object with markers and wreck model .....	56
Fig. 19	Results of a single profile scan of test object with markers and wreck model .....	57
Fig. 20	Scanning mode results of wreck model and test object with markers .....	58



# List of Tables

Table 3.1 Standard deviations of input parameters and their effect on the 3D point standard deviation in mm for world coordinates in 5, 10, 25 and 50 m distance using INS-based platform orientation..... 60

## Tables in Sardemann et al., 2023

Table 1 Standard deviations of input parameters and their effect on the 3D point standard deviation in mm for world coordinates in 5, 10, 25 and 50 m distance ..... 29

## Tables in Sardemann et al., 2021

Table 1 Calibration Results ..... 40

## Tables in Sardemann et al., 2022

Table 1 System parameters ..... 47  
Table 2 Results of single image scan ..... 53  
Table 3 Results for test object with markers in scanning mode ..... 54



# List of Abbreviations

<b>2D</b>	two-dimensional
<b>3D</b>	three-dimensional
<b>ADCP</b>	Acoustic Doppler Current Profiler
<b>CAD</b>	computer-aided design
<b>DTM</b>	digital terrain model
<b>EOR</b>	exterior orientation
<b>GNSS</b>	global navigation satellite system
<b>GPS</b>	global positioning system
<b>IMU</b>	inertial measurement unit
<b>INS</b>	inertial navigation system
<b>IOR</b>	interior orientation
<b>LSM</b>	least squares matching
<b>LUT</b>	look-up-table
<b>PPK</b>	post processing kinematic
<b>RGB</b>	red green blue
<b>RMSE</b>	root mean squared error
<b>RTK</b>	real time kinematic
<b>SDK</b>	software development kit
<b>SfM</b>	structure from motion
<b>SLAM</b>	simultaneous localization and mapping
<b>TLS</b>	terrestrial laser scanner
<b>UAV</b>	unattended (unmanned) aerial vehicle
<b>USV</b>	uncrewed (unmanned) surface vehicle
<b>UWV</b>	uncrewed (unmanned) water vehicle